

Dissertation

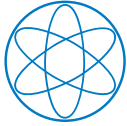
**Aspects of Ultra-Cold Neutron  
Production in Radiation Fields  
at the FRM II**

Stephan Albrecht Wlokka

June, 2016







Fakultät für Physik  
Lehrstuhl für Experimentalphysik (E18)  
Teilchenphysik mit Neutronen (Universe-Cluster)

## Aspects of Ultra-Cold Neutron Production in Radiation Fields at the FRM II

Stephan Albrecht Wlokka

Vollständiger Abdruck der von der Fakultät für Physik  
der Technischen Universität München zur Erlangung des akademischen Grades eines

**Doktors der Naturwissenschaften (Dr. rer. nat.)**

genehmigten Dissertation.

Vorsitzender: apl. Prof. Dr. Norbert Kaiser

Prüfer der Dissertation:

1. Prof. Dr. Peter Fierlinger

2. Prof. Dr. Peter Böni

Die Dissertation wurde am 28.06.2016 bei der Technischen Universität München  
eingereicht und durch die Fakultät für Physik am 17.08.2016 angenommen.



## Abstract

Since the mid-20<sup>th</sup> century scientists have built ever larger accelerators for high energy experiments, which discovered new particles and step by step put together the puzzle of the standard model of particle physics. However, if one wants to measure particle properties very precisely, one can go to very low energies. Ultra-cold neutrons are an excellent tool for high precision physics at energies on the neV scale. Neutrons are called ultra-cold when their energy is low enough, so that they undergo total reflection on material walls under all angles of incident. Thus neutrons can be stored and observed in material or magnetic bottles for long times. The fundamental properties of the free neutron such as the neutron lifetime or a possible neutron electric dipole moment can then be examined.

At the Forschungs-Neutronenquelle Heinz Maier-Leibnitz (FRM II) constructions have begun for a new strong source for such ultra-cold neutrons. This new source operates with deuterium at a temperature of  $\sim 5$  K. This Deuterium will be under constant irradiation from thermal neutrons, fast neutrons and gammas coming from the reactor as well as beta particles coming from activated aluminium structures of the source. In this work the irradiation effects on the deuterium source have been studied. Solid D<sub>2</sub> was irradiated with protons at the Maier-Leibnitz Laboratory (MLL) in Munich. It was studied, whether the ortho/para ratio in the deuterium changes due to the irradiation. Then, the results were extrapolated to the case of the deuterium, which is irradiated at the new ultra-cold neutron source of the FRM II.

Once the ultra-cold neutrons have been produced they have to be guided to the experimental areas. This will be done with so called “Replika” guides. This work covers studies of the surface properties of these guides. In a series of experiments at the Institut Laue-Langevin (ILL) in Grenoble, France the transmission of those guides when filled with helium gas was investigated. Together with simulations, the diffuse reflectivity of the Replika surface was determined.

Helium plays a big role in the operation of the ultra-cold neutron source. Not only is it used as a coolant for the deuterium, acting as a neutron converter, but it is also used to cool the surrounding aluminium beam tubes, which are heated through radiation. In both cases, purified helium with a low helium-3 content will be used, to minimize the amount of tritium produced through neutron capture during the operation of the UCN source. A detector system was tested to measure the tritium content in an irradiated helium sample to access the level of helium-3 in a purified sample.

## Zusammenfassung

Seit der Mitte des 20. Jahrhunderts haben Wissenschaftler weltweit immer größere Beschleuniger für Hochenergie-Experimente gebaut. Diese haben immer neue Teilchen entdeckt und somit Stück für Stück das Standardmodell der Teilchenphysik zusammengebaut. Will man jedoch die Eigenschaften solcher Elementarteilchen sehr genau studieren, so kann man zu sehr geringen Energien gehen. Ultrakalte Neutronen sind ein exzellentes Werkzeug für hochpräzise Messungen bei Energien im neV Bereich. Neutronen heißen “ultrakalt”, wenn ihre Energie klein genug ist, um von Materiewänden unter allen Einfallswinkeln totalreflektiert werden. Sie können dann in Materie- oder Magnetflaschen für etliche Minuten gespeichert werden. Fundamentale Eigenschaften des freien Neutrons, wie dessen Lebensdauer oder ein mögliches elektrisches Dipolmoment, können dann untersucht werden.

An der Forschungs-Neutronenquelle Heinz Maier-Leibnitz (FRM II) hat der Aufbau für eine neue, starke Quelle für solche ultrakalten Neutronen begonnen. Diese Quelle benutzt Deuterium bei einer Temperatur von  $\sim 5$  K. Das Deuterium wird dabei kontinuierlich von thermischen und schnellen Neutronen, sowie  $\gamma$ -Strahlung, die jeweils vom Reaktor kommen, bestrahlt. Auch Elektronen von aktivierten Aluminiumstrukturen der Quelle tragen zur nuklearen Aufheizung bei. In dieser Arbeit wurden zunächst die Bestrahlungs-Effekte auf die Deuterium-Quelle untersucht. Dazu wurde festes  $D_2$  mit Protonen am Maier-Leibnitz Laboratorium in München bestrahlt. Es wurde untersucht, ob sich das Ortho/Para Verhältnis in Deuterium durch die Bestrahlung ändert. Die Resultate wurden anschließend auf den Fall der neuen ultrakalten Neutronenquelle am FRM II extrapoliert.

Die einmal produzierten ultrakalten Neutronen müssen dann zu den Experimenten transportiert werden. Dafür werden sogenannte “Replika”-Leiter benutzt werden. In dieser Arbeit wurden die Oberflächeneigenschaften der Replika-Leiter untersucht. In einer Reihe von Experimenten am Institut Laue-Langevin (ILL) in Grenoble, Frankreich wurde die Transmission der Leiter untersucht, während sie mit Helium gefüllt waren. Zusammen mit Simulationen konnte so die diffuse Reflektivität der Oberfläche bestimmt werden.

Helium spielt eine große Rolle im Betrieb der ultrakalten Neutronenquelle. Es wird nicht nur zur Kühlung des Deuteriums verwendet, das zur Neutronenkonversion dient, sondern auch zur Kühlung der umliegenden Strahlrohre aus Aluminium, welche durch die Bestrahlung aufgeheizt werden. In beiden Fällen wird speziell gereinigtes Helium verwendet, das einen besonders geringen Helium-3 Anteil aufweist, um die Bildung von Tritium, das während des Betriebs durch Neutronen-Bestrahlung entstehen kann, zu minimieren. Es wurde ein Detektorsystem getestet, um den Tritiumanteil einer bestrahlten Heliumprobe zu bestimmen. Damit konnte auf den vorher enthaltenen Helium-3 Anteil einer gereinigten Probe zurückgeschlossen werden.

# Contents

---

<b>1. Introduction</b>	<b>1</b>
1.1. Ultra-cold neutrons . . . . .	1
1.2. UCN physics . . . . .	1
1.2.1. Strong interaction . . . . .	2
1.2.2. Magnetic interaction . . . . .	4
1.2.3. Gravitational interaction . . . . .	4
1.2.4. Weak interaction . . . . .	4
1.3. Ultra-cold neutron production . . . . .	5
1.3.1. Production by moderation . . . . .	5
1.3.2. Superthermal production . . . . .	6
1.3.3. Existing UCN sources . . . . .	9
1.4. Experiments with UCN . . . . .	11
1.4.1. Lifetime of the free neutron . . . . .	12
1.4.2. Electric dipole moment of the free neutron . . . . .	12
1.4.3. Quantized states in the earth's gravitational field . . . . .	13
<b>2. The ultra-cold neutron facility at the FRM II</b>	<b>15</b>
2.1. General concept . . . . .	15
2.2. Converter vessel . . . . .	15
2.2.1. Hydrogen pre-moderator . . . . .	17
2.2.2. Deuterium converter . . . . .	17
2.3. Cooling system . . . . .	17
2.4. UCN extraction system . . . . .	18
2.4.1. Replika guides . . . . .	19
2.4.2. Beam tube exit into the experimental hall . . . . .	20
2.4.3. UCN switches . . . . .	22
<b>3. Deuterium</b>	<b>23</b>
3.1. Thermophysical properties . . . . .	23
3.2. Crystals from cryogenic D <sub>2</sub> . . . . .	24
3.3. Ortho- and para-deuterium . . . . .	24
3.3.1. Definition . . . . .	24
3.3.2. Ortho to para conversion . . . . .	25
3.3.3. Measurement of the ortho-para ratio . . . . .	31
3.3.4. Possible para-enrichment through neutrons . . . . .	34
3.4. Deuterium as superthermal converter . . . . .	35
3.4.1. Production of ultra-cold neutrons . . . . .	35

3.4.2.	Losses of ultra-cold neutrons . . . . .	36
<b>4.</b>	<b>A radiation assisted conversion experiment</b>	<b>39</b>
4.1.	Experimental concept . . . . .	39
4.2.	The experimental setup . . . . .	40
4.2.1.	Irradiation cell . . . . .	40
4.2.2.	Raman setup . . . . .	42
4.2.3.	The Munich tandem accelerator . . . . .	45
4.3.	Equipment test and calibration . . . . .	46
4.3.1.	Irradiation cell . . . . .	46
4.3.2.	Raman spectrometer . . . . .	47
4.3.3.	Tandem accelerator . . . . .	54
<b>5.</b>	<b>Beam time and results</b>	<b>55</b>
5.1.	Beam parameters . . . . .	55
5.2.	Temperature and beam control . . . . .	55
5.2.1.	Cell temperature . . . . .	55
5.2.2.	Beam stability . . . . .	57
5.2.3.	Laser and optics system . . . . .	57
5.2.4.	Crystal quality . . . . .	59
5.3.	Measurement of the $J=0$ content . . . . .	61
5.3.1.	Data at 7.8 K . . . . .	61
5.3.2.	Data at 10 K . . . . .	62
5.3.3.	Uncertainties . . . . .	63
5.4.	Conversion parameters . . . . .	64
5.5.	Irradiated volume . . . . .	67
5.6.	Conversion time . . . . .	68
5.7.	Equilibrium ortho concentrations . . . . .	72
5.8.	Peak widths . . . . .	73
5.9.	Small para fractions and limits of the method . . . . .	75
5.10.	Literature overview concerning $D_2$ irradiation . . . . .	77
<b>6.</b>	<b>Diffuse reflectivity of UCN guides</b>	<b>79</b>
6.1.	Loss parameters . . . . .	79
6.1.1.	Loss on wall bounce . . . . .	79
6.1.2.	Diffuse reflection . . . . .	80
6.2.	Experimental Methods . . . . .	81
6.2.1.	Fixed angle method . . . . .	81
6.2.2.	The helium method . . . . .	81
6.3.	Experimental setup . . . . .	82
6.4.	Results . . . . .	84
6.4.1.	Beam time results . . . . .	84
6.4.2.	Simulation . . . . .	85
6.5.	Conclusions . . . . .	87
<b>7.</b>	<b>Analysis of Pure Helium-4</b>	<b>89</b>
7.1.	Motivation . . . . .	89



## Contents

7.2. Experiment . . . . .	90
7.3. Results . . . . .	94
7.3.1. Count rates . . . . .	94
7.3.2. Helium-3 content . . . . .	96
7.3.3. Background rates . . . . .	97
7.3.4. Helium purity and limit of the method . . . . .	98
<b>8. Conclusion</b>	<b>101</b>
<b>Appendices</b>	<b>105</b>
<b>A. Raman spectroscopy</b>	<b>105</b>
A.1. The Raman effect . . . . .	105
A.2. Molecular energy levels in hydrogen . . . . .	106
A.3. Occupation of the different levels . . . . .	107
<b>B. Data analysis</b>	<b>109</b>
B.1. Raman intensities . . . . .	109
B.2. The Voigt function . . . . .	110
B.3. Determination of the correction factors . . . . .	111
<b>Bibliography</b>	<b>113</b>
<b>Danksagung</b>	<b>119</b>



# List of Figures

---

1.1.	Scheme of the superthermal UCN production principle . . . . .	6
1.2.	Scheme of the UCN/VCN turbine source at the ILL. . . . .	9
1.3.	Layout of the UCN source at PSI. . . . .	10
1.4.	Cutview of the LANL UCN source. . . . .	11
1.5.	Energy eigenvalues for the different levels in the earths gravitational field . . . . .	14
2.1.	Cut view of the FRM II reactor vessel. . . . .	16
2.2.	Cut through the aluminium converter vessel of the new UCN source. . . . .	16
2.3.	Atomic force microscope picture of the Replika guide surface. . . . .	20
2.4.	Radial autocorrelation function calculated for the Replika guides. . . . .	20
2.5.	Floor plan of the experimental hall. . . . .	21
2.6.	Cut view of a UCN switch. . . . .	21
3.1.	The phase diagram of deuterium. . . . .	23
3.2.	Level scheme of the rotational levels of deuterium. . . . .	26
3.3.	The deuterium para concentration vs. temperature. . . . .	26
3.4.	The $J=0$ concentration in the UCN source at the FRM II depending on the temperature. . . . .	30
3.5.	The recombination rate and $J = 1 \rightarrow 0$ conversion rate compared over temperature. . . . .	31
3.6.	Deuterium ortho concentration under irradiation at the FRM II. . . . .	32
3.7.	Raman measurement on a gaseous deuterium sample with natural ortho-para-ratio. . . . .	32
3.8.	Comparison of thermal conductivities of different hydrogen species. . . . .	33
3.9.	Dynamical scattering cross-section of solid deuterium at 7 K. . . . .	34
3.10.	UCN upscattering cross-section vs. temperature. . . . .	37
4.1.	Aluminium irradiation cell used in the experiment. . . . .	41
4.2.	Scheme of the optics used in the experiment. . . . .	43
4.3.	Scheme of the Raman spectrometer light path. . . . .	44
4.4.	Picture of the beam line at the Munich Tandem accelerator lab. . . . .	45
4.5.	Deuterium frozen in the irradiation cell. . . . .	46
4.6.	Measured Raman spectrum of silicon. . . . .	47
4.7.	Raman spectrum of a silica-core glass fibre. . . . .	48
4.8.	Measured Raman spectra of gaseous deuterium. . . . .	49
4.9.	Raman spectrum of liquid hydrogen at 15 K. . . . .	50
4.10.	$J = 0$ content in the liquid hydrogen sample over time. . . . .	50

4.11. Raman spectrum of deuterium at 7.1 K. . . . .	51
4.12. Ortho content of deuterium during cooldown and freezing. . . . .	52
4.13. Ortho fraction of the D <sub>2</sub> sample over time. . . . .	53
4.14. Ortho fraction in the deuterium sample at different temperatures. . . . .	53
5.1. Comparison of two temperature trends during irradiation. . . . .	56
5.2. Comparison of Raman intensities at two different ortho concentrations $c_o$ after freeze out. . . . .	59
5.3. Laser power monitor data trends. . . . .	60
5.4. $J=0$ content in the deuterium during the first beam time. . . . .	61
5.5. $J=0$ content in the deuterium during the second beam time. . . . .	63
5.6. Ortho fraction during the beam days used for the analysis. . . . .	65
5.7. Fits to the experimental data. . . . .	66
5.8. Summary of $J=1$ to $J=0$ conversion times in solid D-T from 1.8 to 14 K. . . . .	69
5.9. Calculated conversion time for a deuterium crystal under irradiation. . . . .	70
5.10. Calculated evolution of the $J=0$ concentration for different temperatures of the ultra-cold neutron source at the FRM II. . . . .	71
5.11. Ortho concentration vs. temperature for the new UCN source at the FRM II. . . . .	72
5.12. Relative UCN output of a deuterium source for different concentrations of para deuterium. . . . .	73
5.13. Raman peak width vs. measured ortho concentration in the two beam times. . . . .	74
5.14. Vibrational Raman lines of deuterium for two different $J=0$ concentrations. . . . .	76
6.1. Sketch of the helium transmission experiment. . . . .	82
6.2. The experimental setup at the ILL PF2/TES beam. . . . .	83
6.3. Relative count rates vs. helium pressure in the guide system. . . . .	84
6.4. Logarithmic plot of the helium transmission curve for 2 m guide length. . . . .	85
6.5. View of the simulated setup. . . . .	86
6.6. Comparison of simulated and experimental data. . . . .	87
7.1. Total tritium activity over time in the cooling systems of the UCN source for two different <sup>3</sup> He concentrations. . . . .	90
7.2. Scheme of the helium filling device used to fill the glass cuvettes with pure helium. . . . .	91
7.3. Picture of the detector used for the tritium detection. . . . .	92
7.4. Schematic layout of the detector setup. . . . .	93
7.5. Typical spectrum of the tritium detector at $U = 2600$ V. . . . .	95
7.6. Background subtracted count rates for the three measured cuvettes. . . . .	96
7.7. Comparison of the background measurement and the actual measurement of cuvette no. 2. . . . .	97
7.8. The background count rate in the detector after measuring the cuvettes. . . . .	98

*List of Figures*

B.1. Comparison of different fitting functions. . . . . 110



# List of Tables

---

1.1. Coherent scattering lengths and the resulting Fermi potentials for different materials . . . . .	3
3.1. Para- and Ortho- definitions in the different hydrogen species. . . .	25
5.1. Average temperatures of the deuterium crystal during irradiation on the three different beam days used for the analysis. . . . .	62
5.2. Fit results and their respective uncertainties. . . . .	66
5.3. Calculated irradiated volumes during the experiments. . . . .	68
5.4. Results of the exponential fits to the data curves. . . . .	69
5.5. Results of the linear fits to the peak width data. . . . .	75
6.1. Calculated values for the mean path lengths of UCN through the helium volume. . . . .	88
7.1. Measured count rates for the different cuvettes with statistical uncertainties. . . . .	95





# Chapter 1.

## Introduction

---

### 1.1. Ultra-cold neutrons

Neutrons can be characterized as "ultra-cold" if they are totally reflected from a given material wall under all angles of incident. Typically such ultra-cold neutrons (UCN) have energies below 300 neV or velocities smaller than  $8 \text{ m/s}$ . UCN can then be stored in material or magnetic bottles to observe them for long times ( $\sim 10^3 \text{ s}$ ). They are used to determine the lifetime of the free neutron [Mam89, Pic05] or its possible electric dipole moment (EDM)[Alt10]. One can also investigate quantum states of the gravitational interaction [Abe11]. Measurements of the lifetime of the free neutron make it possible to measure the coupling constants of the weak interaction. Since the neutron lifetime is also an important parameter in primordial nucleosynthesis a precise measurement would greatly improve current theories and simulations of the early universe.

A non-zero neutron electric dipole moment gives rise to a CP violation which then could explain the matter-antimatter asymmetry observed in our universe.

With the observation and investigation of quantum gravity states of the free neutron it is possible to test Newton's law of gravity down to  $\mu\text{m}$  scales which is inaccessible to most other measurement methods.

### 1.2. UCN physics

Although neutron physics in general, the interaction of neutrons with matter and the neutron  $\beta$ -decay are well understood, there are still some discussions and open issues when discussing neutron physics at the lower end of the energy spectrum [Ste91, Ste10, Ser10]. This section shall give an overview of the current state of the physics with ultra-cold neutrons.

### 1.2.1. Strong interaction

As mentioned above, neutrons can be totally reflected from material walls under certain circumstances. The force responsible for this reflection is the strong interaction. The interaction potential can be described by a square-well potential with a depth  $V_0 = 40 \text{ MeV}$  and a width of  $R_0 A^{\frac{1}{3}}$  (constant nuclear density) with  $R_0$  being on the order of  $1 - 2 \text{ fm}$  and  $A$  the atomic number.

There is also the possibility of a nucleus capturing the incoming neutron which is called absorption. The reaction rate for this process is proportional to  $|M|^2 / \Phi_{\text{inc}}$ , where  $M$  is the matrix element describing the absorption and  $\Phi_{\text{inc}}$  is the incoming neutron flux. Since the energies observed with cold and ultra-cold neutrons are much smaller than the strong interaction potential the perturbed wave function of the neutron will be practically independent of the incident neutron energy and therefore the absorption cross section  $\sigma_{\text{abs}}$  follows  $1/v_n$ . [Gol91]

#### Neutron scattering on a single nucleus

To solve this scattering problem one considers an incoming plane wave  $e^{i\vec{k}\vec{r}}$  describing the incoming neutron with its wave vector  $\vec{k}$  and distance from the scattering area  $\vec{r}$ . Inside the nuclear radius  $R$  one finds the nuclear potential described above with  $V = V_0$ . The solution  $u = r\psi$  inside the potential can be written as

$$u \sim A \sin(Kr) \quad K = \sqrt{\frac{2m(E + V_0)}{\hbar^2}} \quad (1.1)$$

which satisfies the boundary condition  $u = 0$  at  $r = 0$  [Gol91]. One can then write for the total wave function

$$\psi = e^{i\vec{k}\vec{r}} + f(\theta) \frac{e^{ikr}}{r}. \quad (1.2)$$

Since

$$kR \ll 1 \quad (1.3)$$

the scattering is dominated by s-wave scattering [Gol91] and one can thus write

$$f(\theta) = -a. \quad (1.4)$$

Here,  $a$  is the so called scattering length and can be interpreted as the radius of a hard sphere producing the same wave function for  $r \gg R$ . The scattering length is positive for almost all elements except for a handful of materials with hydrogen being one of them. Table 1.1 shows the scattering lengths and the Fermi potentials for different materials, which are often used in UCN experiments.

Table 1.1.: Coherent scattering lengths and the resulting Fermi potentials for different materials [Sea92].

Materials	Scattering length [fm]	Fermi Potential [neV]
Solid Hydrogen	-3.74	-51.6
Solid Deuterium	6.67	107.7
Liquid Helium-4	3.26	16.0
Beryllium	7.79	250.8
Graphite	6.65	196.3
Diamond	6.65	305.7
Oxygen	5.80	87.4
Aluminium	3.45	53.5
Titanium	-3.44	-50.7
Vanadium	-0.38	-7.2
nat. Nickel	10.3	245.1
Nickel-58	14.4	346.8
Iron	9.45	208.9
Stainless Steel	8.16	187.4
Copper	7.72	169.9

### The Fermi pseudo-potential

As the energy of a neutron is typically much smaller than the interaction potential of a nucleus the neutron wave function in the presence of the potential will be very different from the incoming wave function thus forbidding to use perturbation theory to calculate the outgoing wave. Fermi was the first to realize that since the interaction region is small compared to the neutron wavelength one could replace the potential with a potential of much smaller depth but larger radius and thus be able to calculate the wave function outside the region of interaction [Fer36].

Using Born approximation one finds for the so called Fermi potential

$$V_F = \frac{2\pi\hbar^2 a}{\mu} \delta^{(3)}(\mathbf{r}), \quad (1.5)$$

with  $\mu$  being the reduced mass of the scattering system.

If one then considers scattering from a system of fixed nuclei, one first has to substitute the scattering length  $a$  with the bound scattering length

$$a_B = \frac{m}{\mu} a \quad (1.6)$$

with the neutron mass  $m$ . This then yields the Fermi potential for the scattering problem of a neutron incident on a solid body [Gol91]

$$V_F = \frac{2\pi\hbar^2}{m} N a, \quad (1.7)$$

using the material number density  $N$ .

Considering this, it is easy to see that a neutron with energy smaller than the Fermi potential of a given material will be totally reflected.

### 1.2.2. Magnetic interaction

Neutrons have a magnetic moment  $\vec{\mu} = -1.913\mu_N\vec{s}$  with the nuclear magneton  $\mu_N = \frac{e\hbar}{2m_P}$ . Thus they can be stored in magnetic bottles since the magnetic potential arising from a magnetic field amounts to

$$V_{\text{mag}} = \vec{\mu} \cdot \vec{B} = \pm 60.4 \cdot B \frac{\text{neV}}{\text{T}}. \quad (1.8)$$

A magnetic field of roughly 3.5 T can produce a potential barrier close to that of a stainless steel wall. One must pay attention though because it is not possible to store both spin states in a magnetic bottle. As one can see from Eq. 1.8 one spin state is repelled by the magnetic field gradient while the other one is accelerated by the field.

### 1.2.3. Gravitational interaction

In contrast to many other nuclear particles UCN are strongly affected by gravitation. The gravitational potential is

$$V_{\text{grav}} = mgh = 102 \frac{\text{neV}}{\text{m}} * h. \quad (1.9)$$

This has several effects when dealing with ultra-cold neutrons. If an experiment consists of a large bottle the UCN density will show a gradient along the height axis, which one might have to take into account when interpreting experimental results. On the other hand one can use gravitation to ones advantage. For example there is no need to close bottle experiments to the top side, since neutrons with an energy low enough cannot escape the storage volume. Or it is possible to accelerate UCN by letting them fall down a certain height and decreases absorption and reflection on entrance windows of detectors.

### 1.2.4. Weak interaction

The free neutron itself is an unstable particle with a lifetime of  $(880.3 \pm 1.1)$  s [Oli14]. The weak interaction is responsible for the decay

$$n \rightarrow p + e^- + \bar{\nu}_e. \quad (1.10)$$

The understanding of the  $\beta$  decay of the free neutron is of great interest. Measuring the lifetime of the free neutron with a better accuracy will allow to put better limits on variables of the weak interaction, mainly the  $V_{ud}$  element of the CKM matrix and thus, the unitarity of said matrix. Other new experiments are currently built and underway to determine the strength of the different parameters in the famous Jackson formula [Jac57], which labels the contributions of the different particles (i.e. coupling of the different momenta, coupling of angular momentum to the momenta of the decay particles) of the  $\beta$  decay with different letters. The new **Proton Electron Radiation Channel** (PERC) [Dub08] at the FRM II, for example, will enable experimentalists to measure most of these quantities at the same beam under the same experimental conditions. Previous experiments already determined parts of this so-called “neutron alphabet” [Bae08, Mä09, Men13].

### 1.3. Ultra-cold neutron production

Producing ultra-cold neutrons is a tedious and laboursome task. The only practical way to slow down neutrons is to have them interact with a material. These interactions, of course, can lead to the loss of the neutron. Finding the right process with the least losses to produce a high UCN density has been one of the great challenges for UCN physicists over the last decades.

#### 1.3.1. Production by moderation

Using a maxwellian shaped spectrum as an approximation for a reactor neutron source, a calculation shows that in a thermal spectrum of  $T = 300$  K only a fraction of  $3 \cdot 10^{-8}$  of particles has an energy of less than 300 neV. This was calculated by simply integrating the the Maxwell-Boltzmann distribution up to the cutoff energy for UCN. One prominent way of increasing the amount of UCN is moderation. By having the neutrons interact with a cold medium they are moderated towards the temperature of the medium and the amount of UCN is increased. Typical cold sources use exactly this mechanism to produce cold neutrons. For example at the FRM II a liquid deuterium moderator with a temperature of 20 K is used to achieve this. Considering again a Maxwell distributed energy spectrum, a fraction of  $2 \cdot 10^{-6}$  of UCN can be found in such a moderator.

If one wanted to further increase the UCN fraction, one would have to go to even lower temperatures of the moderator. In order to increase the UCN content to more than 2/3 one has to lower the moderator temperature to 2 mK. In a high flux, high radiation neutron source environment it is simply impossible to keep the thermal load to the moderator within acceptable limits.

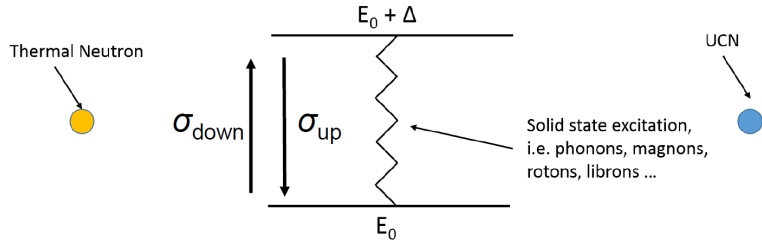


Figure 1.1.: Production of ultra-cold neutrons in a solid state crystal in a simplified two-level picture. Thermal neutrons excite a solid state excitation and, in a single process, lose nearly all their kinetic energy and exit the converter as an ultra-cold neutron. The down-scattering cross-section  $\sigma_{\text{down}}$  describes the loss of neutron energy and the energy gain of the converter, while it is vice-versa for the up-scattering cross-section  $\sigma_{\text{up}}$ .

### 1.3.2. Superthermal production

In 1975 the idea of the superthermal conversion process was born [Gol75]. Contrary to the classical moderation process, the neutrons are not brought into thermal equilibrium with its surroundings but only a balance between the production and loss processes is achieved.

Considering a simple two-level system like it is depicted in fig. 1.1 a neutron enters a solid state body and scatters on the body by exciting a solid state excitation. If the neutron energy and the excitation energy match, the neutron will lose almost all its kinetic energy in that single process. This process is called “down-scattering”, which is mainly governed by the cross-section  $\sigma_{\text{down}}$ , where the neutron loses, and the converter system gains energy. Vice-versa up-scattering is linked to the cross-section  $\sigma_{\text{up}}$ .

The excitation can be of the whole spectrum of solid state excitations, for example phonons, rotons, magnons, librions, etc. Typical excitation energies of solid state bodies lie in the order of several meV. Thus thermal neutrons need to be pre-moderated to temperatures matching the spectrum of solid state excitations of the material used for the conversion process.

The equality of production and loss processes in the superthermal UCN production is expressed in the so-called “Principle of detailed balance” [Gol91].

$$\sigma_{\text{up}} = \frac{E_{\text{UCN}} + \Delta}{E_{\text{UCN}}} e^{-\frac{\Delta}{k_{\text{B}}T}} \sigma_{\text{down}} \quad (1.11)$$

Here  $\Delta$  denotes the energy of the solid-state excitation. The down-scattering cross section  $\sigma_{\text{down}}$  is more or less constant with temperature [Yu86, Fre10]. Thus one can easily see that the up-scattering process (left-hand side) can be greatly suppressed by simply cooling down the converter medium and thus making the factor  $e^{-\frac{\Delta}{k_{\text{B}}T}}$  arbitrarily small. Further cooling of the moderator only makes sense if other loss channels do not start to dominate over the up-scattering loss. In

Deuterium for example, the absorption losses, which are generally independent of temperature, and up-scattering losses are equal around 5 K [Liu00, Sea92]. Thus cooling the Deuterium further below this temperature would not yield a higher UCN output.

### Available materials

There are several materials available for the use as a superthermal UCN converter. Choosing an appropriate material for a specific application is crucial for building a high power UCN source. The following is a (incomplete) list of criteria an ideal converter material has to fulfil:

- A high neutron scattering cross-section is essential in order to have an interaction in the first place.
- A low absorption cross-section minimizes losses in the source itself.
- The solid state excitation spectrum needs to match the spectrum of incoming neutrons. A pre-moderation might be necessary to shape the incoming spectrum according to ones needs.
- A low fermi-potential helps increasing the phase-space which one can transport through UCN guides to the experiments.
- A low atomic mass is helpful in two ways: First, it decreases nuclear heating coming from the neutron source radiation and thus facilitates the converter cooling. Due to kinematics the energy lost in elastic scattering is greater on average if the neutron and the scattering particle have a similar mass.
- Thermophysical properties like heat capacity and thermal conductivity are crucial to the temperatures which one can achieve in the converter.
- The properties as a solid are crucial to the choice of a converter material. The preparation of the crystal has strong effects on the structure of the crystal and thus on the extraction efficiency for UCN.
- Chemical properties are important for security reasons. For example, explosive, flammable or corrosive materials can pose security risks.
- A high natural abundance reduces cost for obtaining a high purity converter.

These requirements are met by a few materials, which are briefly described in the next section. This list is not necessarily complete, yet it covers the materials, where the most effort towards new UCN sources has been made.

- **Hydrogen**

Hydrogen was among the first materials to be considered as a UCN producing material. The very high neutron scattering cross-section and the low mass make it a perfect candidate. However, hydrogen also has a high absorption cross-section for neutrons when compared to its heavier isotope deuterium. Thus, only a thin film source would be possible, which then limits the UCN output due to its smaller volume. While a UCN source using hydrogen is certainly feasible, the UCN output will be lower compared to deuterium.

- **Deuterium**

Deuterium was one of the first materials to be considered for a superthermal source [Gol75]. It has a low atomic mass, which increases UCN output and decreases nuclear heating. The optimal operating temperature for such a source is 5 K, which can be achieved by cooling with liquid helium. Thus, deuterium can be used in a reactor environment even in close proximity to the reactor fuel element. One has to take care though, because Deuterium is flammable when being mixed with oxygen.

- **Helium**

Helium has one big advantage over all other materials for UCN production: It has an absorption cross-section of exactly 0 barn. On the other hand with helium one can only use neutrons with a wavelength of  $8.9 \text{ \AA}$ , which matches the rotonic excitation of Helium. In order to minimize upscattering losses one has to cool the helium down to  $\sim 0.5 \text{ K}$ . Thus an installation close to a reactor fuel element is very difficult and costly. But high UCN densities can be achieved when conducting an experiment within the helium.

- **$\alpha$ -Oxygen**

Oxygen has a lower production cross section for UCN than  $\text{D}_2$  [Liu08], even though magnon excitations enhance the production. But oxygen has a very low absorption cross section which makes up for the lower production. Building an oxygen UCN source would require large volumes. This is difficult to achieve because oxygen has two phase transitions in its solid state, one of which is crucial to the optical and UCN properties of the crystal.

- **$\alpha$ - $^{15}\text{N}$**

Nitrogen-15 would be an ideal candidate for a UCN converter material. It has a high production cross-section combined with a very low absorption cross-section. Unfortunately it is quite rare (0.37% natural abundance) and any  $^{14}\text{N}$  impurities dramatically decrease the converter performance. Until now it could not be shown that it is possible to produce UCN with



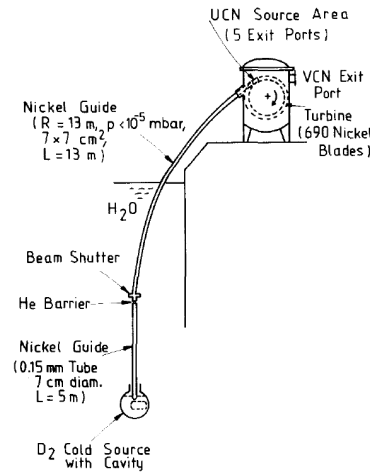


Figure 1.2.: Scheme of the UCN/VCN turbine source at ILL. A straight and a curved guide tube conduct slow neutrons ( $\lambda > 20 \text{ \AA}$ ) from the “vertical” cold source to a Garching-type turbine where one half of the beam ( $3.4 \times 7 \text{ cm}^2$ ) is decelerated to the UCN regime by multiple reflection on the receding nickel blades, thereby producing a  $16 \times 8 \text{ cm}^2$  wide UCN beam with a current density of  $2.6 \cdot 10^4 \text{ UCN cm}^{-2} \text{ s}^{-1}$  and a total UCN current of  $3.3 \cdot 10^6 \text{ s}^{-1}$  (for  $v_z < 6.2 \text{ m/s}$ ). The second half of the beam will bypass the turbine wheel and will be used for cold-neutron experiments. The guides and the turbine blades were produced on an all-metal basis using the replica-technique. Picture and captions taken from [Ste86].

nitrogen-15, because of  $^{14}\text{N}$  impurities.

### 1.3.3. Existing UCN sources

Over the past decade there have been great efforts around the world to build new strong UCN sources based on the superthermal converter principle [Mar08, Ang09, Sau13, Zim15]. Since 1986 the strongest multi-purpose user source worldwide still is the UCN turbine installed at the Institut Laue-Langevin in Grenoble, France.

#### The ILL turbine

The working principle of the UCN turbine in Grenoble is shown in figure 1.2. A liquid deuterium cold source produces cold neutrons which are then vertically extracted. A nickel coated bend tube guides the neutrons upwards to the turbine. While travelling upwards the neutrons already lose part of their energy (see section 1.2.3). In the turbine itself 690 nickel blades are turning at a velocity of  $20 \text{ m/s}$  [Ste86]. A neutron travelling with the velocity  $v$  and reflecting off one of the blades with velocity  $V$  will have a velocity  $v - V$  with respect to the blade before the collision and  $V - v$  after the collision which corresponds to a velocity of  $2V - v$  in

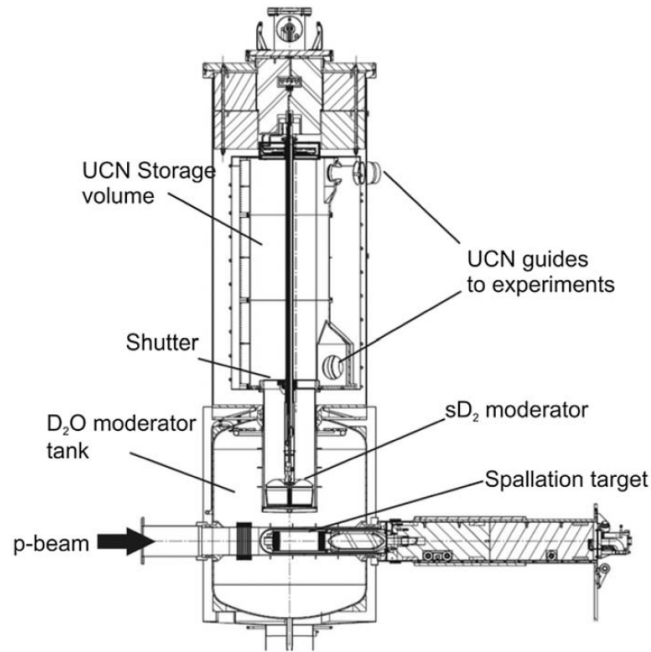


Figure 1.3.: Picture and caption taken from [Ang09]. Layout of the UCN source at PSI. The proton beam hits the spallation target from the left. Spallation neutrons will be thermalized in the ambient temperature  $D_2O$  moderator, further cooled and downscattered into the UCN regime in the cold  $sD_2$ . The UCN reach the storage volume via a vertical neutron guide where they can be trapped and distributed to the experiments.

the laboratory frame [Gol91]. UCN densities which have been achieved in storage vessels connected to the turbine vary from  $19\text{ cm}^{-3}$  to  $41\text{ cm}^{-3}$  [Gol91].

### The PSI deuterium source

At the Paul-Scherrer-Institute in Villigen, Switzerland a new deuterium based source for ultra-cold neutrons was recently installed [Ang09]. “Protons from the 600 MeV PSI ring cyclotron with a continuous wave intensity of  $I_p \geq 2\text{ mA}$ , i.e. at a power of more than 1.2 MW, hit a spallation target made of lead-filled zirconium tubes.” [Ang09].

The neutrons from the spallation target are then moderated in  $3.5\text{ m}^3$   $D_2O$  as depicted in Figure 1.3. In the center of the  $D_2O$  moderator there is an aluminium vessel containing up to  $30\text{ dm}^3$  of deuterium, which acts as the UCN converter as well as as pre-moderator.

The UCN are then extracted vertically and are brought into a storage volume. From there on they can be guided further to the experiments. Densities of  $30\text{ cm}^{-3}$  have been reached at the beam port position [Rie13].

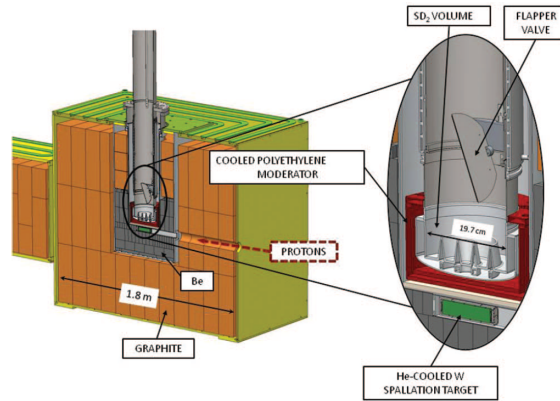


Figure 1.4.: Picture and caption taken from [Sau13]. Cutaway view of the LANL UCN source. The graphite cube is 1.8 m on a side. This entire assembly is surrounded by the biological shield, consisting of at least 3 m of steel and 2 m of concrete in all directions.

### The Los Alamos UCN source

Since 2008 a deuterium based UCN source is in operation at the Los Alamos National Laboratory. A detailed description of the source can be found in [Sau13]. Protons with an energy of 800 MeV from the LANSCE accelerator are delivered to a helium-cooled tungsten alloy-spallation target, which is sitting right beneath the UCN converter. The sD<sub>2</sub> converter has a cylindrical shape with a diameter of 19.7 cm and a height of 5.7 cm. It is contained in a 2 cm thick aluminium cryostat, which is cooled with liquid helium. The cryostat is coated with <sup>58</sup>Ni to reflect and contain the UCN. There is an array of fins on the bottom of the cryostat to improve the thermal coupling between the aluminium and the deuterium. A moderator made of polyethylene is mounted between the cryostat and the spallation target to cool down the neutrons before they enter the deuterium. A flapper valve directly above the converter can block neutrons from returning to the source between two pulses. The source setup, including the tungsten target and the biological shielding can be seen in figure 1.4. Proton pulses with a peak current of 10 mA are delivered in 5 pulses of length 625 μs at 20 Hz, with a gap between the pulse groups of 5.0 s. A peak flux of 1.33 CN/s/cm<sup>2</sup> was measured by replacing the solid deuterium with an argon crystal. A UCN density of  $(52 \pm 9) \text{ cm}^{-3}$  was measured at the source exit outside the biological shielding.

## 1.4. Experiments with UCN

The ability of ultra-cold neutrons to be stored for several hundred seconds and its property of bouncing off of material walls make them a probe for fundamental research as well as an examination object itself. This section shall give an overview over the applications for ultra-cold neutrons.

### 1.4.1. Lifetime of the free neutron

The neutron lifetime  $\tau_n$  is a crucial parameter to any theory concerning the early universe and primordial nucleosynthesis. It influences the abundance of helium and other light elements shortly after the Big Bang. The lifetime  $\tau_n$  is also a vital parameter to further understand the weak interaction and its coupling constants. Together with other experiments it is possible to determine the matrix element  $V_{ud}$  of the Cabbibo-Kobayashi-Maskawa (CKM) matrix, and test the unitarity of the CKM matrix, which then helps testing the three-generation Standard Model.

The current value for the neutron lifetime is  $(880.3 \pm 1.1)$  s [Oli14]. This value has been under debate for some time now, so new measurements are trying to determine the neutron lifetime with improved precision. One of those experiments is the so called “PENeLOPE” experiment [Pic05, Mat09]. It is foreseen to be one of the first experiments conducted at the new UCN source of the FRM II.

PENeLOPE has a major advantage over previous experiments. It traps the neutrons magnetically, thus eliminating wall collisions and any systematic effects arising from those collisions. The experiment will consist of the following steps:

- The storage volume is filled with polarized UCN.
- A ring made out of a neutron absorbing material is lowered into the storage volume down to the desired height to get rid of any higher energy neutrons.
- The superconducting magnets are ramped up.
- Since only one neutron spin state can be trapped in the experiment, there has to be a short amount of time waiting for the wrong spin state to disappear.
- The system is left untouched for a varying decay time during which the decay protons are detected.
- The magnetic field is turned off and the remaining neutrons in the trap are counted.

By repeating this cycle and employing two different measurement principles at the same time a precision of down to 0.1 s is possible.

### 1.4.2. Electric dipole moment of the free neutron

One of the most interesting problems in current cosmology physics is the observation of the matter-antimatter asymmetry, which cannot be explained within the

Standard Model (SM). The Standard Model can only explain part of the observed asymmetry, which within the SM arises from the CP violating decays of Kaons and the B-meson. Sakharov mentioned that in order to account for the matter - antimatter asymmetry one needs baryon number violation, a departure from thermal equilibrium and other sources of CP violation [Sak67].

Electric Dipole Moments (EDMs) of fundamental particles provide a CP violating mechanism, assuming that the combined CPT symmetry is always conserved. The SM predicts a neutron EDM of  $d_n \sim 10^{-32 \pm 1} \text{ e} \cdot \text{cm}$ . However, SUSY and many other extensions of the SM predict much larger values, which are close to the current experimental limit of  $d_n < 2.9 \cdot 10^{-26} \text{ e} \cdot \text{cm}$  [Bak06].

nEDM experiments are based on Ramsey's method of separated oscillatory fields. The Hamiltonian is given by [Alt10]

$$\hbar\omega = -\frac{\vec{S}}{|S|} \left( \vec{\mu}\vec{B} - \vec{d}\vec{E} \right). \quad (1.12)$$

Hereby,  $\vec{\mu} = g\mu_N\vec{N}$  is the product of the g-factor and the nuclear magnetic moment, the spin  $\vec{S}$  is 1/2 and the parameter  $\vec{d}$  is the electric dipole moment. By measuring the Larmor precession  $\omega$  with parallel and anti-parallel orientations of  $\vec{B}$  and  $\vec{E}$  the EDM is extracted from the phase shift  $\Delta\omega$  between those measurements [Alt10]

$$\vec{d} = \frac{\hbar\Delta\omega}{4E}. \quad (1.13)$$

The uncertainty for this measurement can be written as [Alt10]

$$\delta d = \frac{\hbar}{2E\alpha T\sqrt{N}}, \quad (1.14)$$

where  $N$  is the number of neutrons counted in the experiment and  $\alpha$  is a ‘‘quality’’ parameter for the measurement, including the polarization loss during the measurement time  $T$ .

In order to improve the limit down to  $5 \cdot 10^{-28} \text{ e} \cdot \text{cm}$  one needs strong sources for ultra-cold neutrons as one can easily see from eq. 1.14.

### 1.4.3. Quantized states in the earth's gravitational field

An ultra-cold neutron with mass  $m_n$  which falls due to gravity and bounces off a flat surface is an example of a quantum bouncer [Abe11]. The system forms a potential well, with the flat surface as a hard sphere potential on one end, and gravity with a linearly increasing potential on the other. If the energy of the neutrons is small enough, one can find discrete energy levels which form in the potential well. The existence of such discrete levels was shown in the last decade [Nes02] and the first energy eigenvalues  $E_n = \hbar\omega$  of the lowest levels  $|n\rangle$  are between 1 – 5 peV [Abe11], as depicted in Figure 1.5.

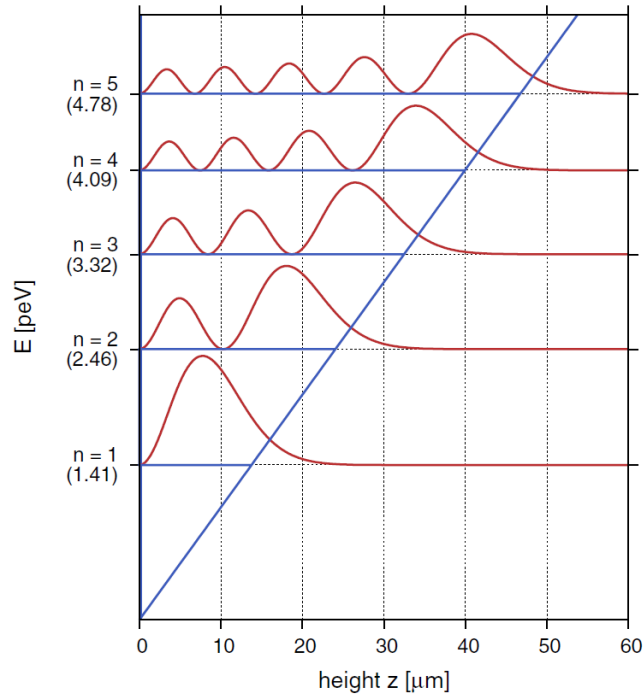


Figure 1.5.: Energy eigenvalues (blue) and neutron density distribution (red) for level one to five. [Abe10]

These experiments enable the investigation of Newton's laws of gravity on very small scales down to a few  $\mu\text{m}$ . There have been several new theoretical descriptions solving different problems in current astrophysics and cosmology. One of these theories predicts large extra dimensions in space-time. These were introduced by Arkani-Hamed, Dimopoulos and Dvali [AH98] to solve the hierarchy problem of particle physics. Differences between these theories and Newtonian gravity could be tested at very small distances.

## Chapter 2.

# The ultra-cold neutron facility at the FRM II

---

Several institutes all over the world are currently building new sources for ultra-cold neutrons [Sau13, Kor07, Lau11, Mar08]. The Forschungs-Neutronenquelle Heinz Maier-Leibnitz (FRM II) is one of these institutes [Fre07, Fre14]. This chapter provides an overview of the concept foreseen at the FRM II and the physical and engineering challenges of the project.

### 2.1. General concept

At the FRM II a deuterium based source for ultra-cold neutrons is planned. Figure 2.1 shows a cut view of the FRM II reactor. The Deuterium crystal sits almost at the point of highest thermal neutron flux [Rö09]. The source is cooled with liquid Helium from the backside. Hydrogen, which acts as a pre-moderator for the neutrons, is also fed to the converter vessel from the backside. After down-scattering the UCN leave the deuterium crystal into the guide volume and are guided towards the SR6 beam tube exit.

The UCN source itself will sit at a position  $\sim 60$  cm away from the reactor fuel element. Between the source and the actual beam tube there is a double-walled aluminium tube acting as a safety barrier. Due to the high thermal load from neutrons and gammas this tube needs to be cooled as well during the operation of the UCN source.

### 2.2. Converter vessel

The converter vessel is a double-walled aluminium toroid as depicted in Figure 2.2. The vessel is cooled with a supercritical helium circuit (8.7 kg in total @  $T = 5$  K

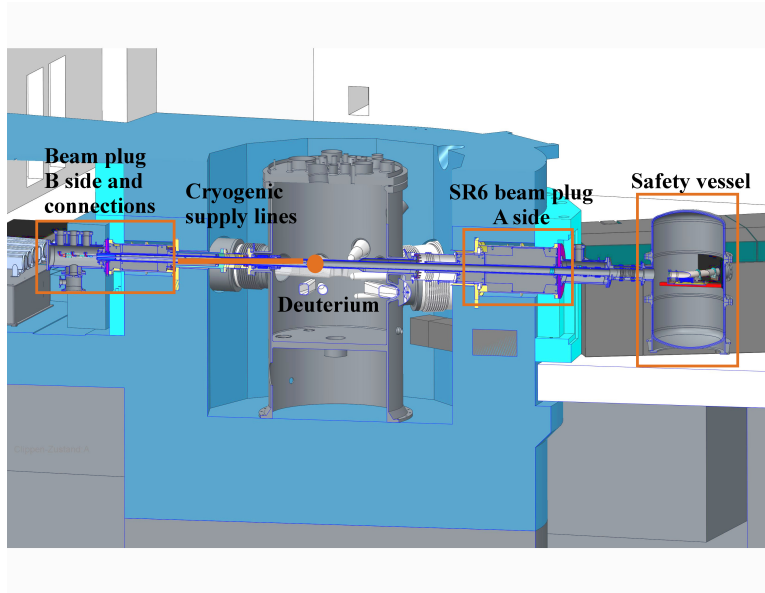


Figure 2.1.: Cut view of the FRM II reactor vessel. The UCN source is sitting near the point of highest thermal flux within the through going SR6 beam tube. All cryogenics and supply lines feed the source from the backside (left side in the picture). The ultra-cold neutrons are extracted to the right side and are guided towards the safety vessel.

and  $p = 3.4$  bar). The inside toroid is filled with 12.5 mol solid hydrogen as a pre-moderator. It shifts the energy spectrum of the incoming thermal neutron flux to a slightly colder regime. However, the hydrogen layer is not thick enough to bring the neutrons in thermal equilibrium. On the outside there is up to 12.5 mol solid

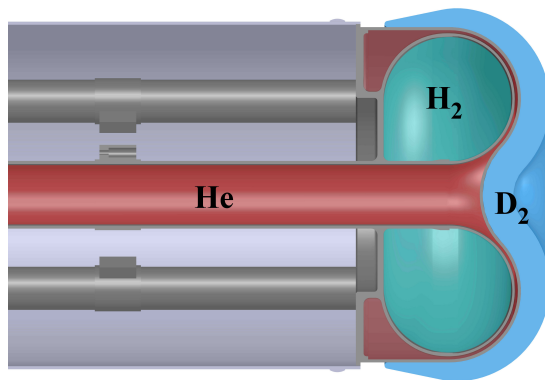


Figure 2.2.: Cut through the aluminium converter vessel of the FRM II UCN source. The vessel is cooled with liquid helium (red) flowing through the double-walled vessel. The inside of the toroid is filled with solid hydrogen (turquoise). Deuterium is frozen onto the outer surface (blue).



deuterium frozen to the Al surface, which is the main part of the UCN source, as it acts as the conversion material, where the neutrons will lose nearly all of their energy.

### 2.2.1. Hydrogen pre-moderator

As discussed in Chapter 1 the production of ultra-cold neutrons in the superthermal conversion process relies on the excitation of solid-state excitations, such as phonons, rotons, magnons. In solid deuterium such excitations have typical energies between 4 – 12 meV [Fre10]. The thermal spectrum coming from the FRM II on average has a higher energy than the energy of the deuterium phonon spectrum. The solid hydrogen pre-moderator shifts the energy spectrum of the incoming neutrons towards lower energies by elastic collisions. The width of the H<sub>2</sub> layer is too small to completely moderate the neutrons, but since the spectrum now better matches the deuterium phonon spectrum the overall UCN output should be increased.

### 2.2.2. Deuterium converter

The deuterium converter is the main part of the UCN source planned at the FRM II. The triple point of deuterium is 18.6 K [Sou86]. Since the whole source is mounted horizontally one cannot go through the liquid phase to form a solid crystal but one rather has to resublimates directly from the gas phase. This process needs to be done slowly and carefully to ensure a transparent crystal while maintaining vacuum conditions of  $< 10^{-5}$  mbar. This process has been tested previously [Wlo11] and it could be shown that at flow rates of deuterium gas of less than 30 sccm a clear crystal can be created.

The total volume of the D<sub>2</sub> will be  $\sim 180$  cm<sup>3</sup>. This corresponds to a layer thickness of roughly 15 mm. The source will operate at a temperature of 5 K. At this temperature the temperature-independent absorption cross-section  $\sigma_{\text{abs}}$  becomes greater than the temperature dependent upscattering cross-sections from a UCN to a cold or thermal neutron  $\sigma_{\text{up}}$ . A further decrease in temperature would not increase the UCN output.

## 2.3. Cooling system

The total heat load due to neutrons, gamma and beta radiation from the surroundings onto the aluminium converter nose will be  $\sim 55$  W [Rö09]. The combined heat load on deuterium and hydrogen will be  $\sim 27$  W. This heat has to be

transported away by the supercritical helium flowing through the double-walled Al vessel.

The cooling system is comprised of several stages. First there are two helium compressors. The compressed helium is then liquefied in the two main cooling machines (coldboxes), each with a cooling power of 500 W at 4 K temperature. The liquid helium from one or both machines then cools the supercritical helium going to the UCN source via a heat exchanger. In order to minimize this amount of tritium produced within the helium used for cooling, the UCN source will be cooled with specially purified  $^4\text{He}$  [Hen87] where the fraction of  $^3\text{He}$  is smaller than  $10^{-9}$ .

The cooling power of only one coldbox is sufficient to run the UCN source even when the new facility for the production  $^{90}\text{Mo}$  at the FRM II is operating. With the second coldbox the cooldown phase can be greatly quickened.

The double-walled safety tube which encloses the whole UCN source also needs to be cooled. The space between the two tubes that make up the double-wall will be flushed continuously with Helium, which is pre-cooled to 220 K. The temperature of the safety tube will then reach a maximum temperature of about 350 K [Pfi14].

## 2.4. UCN extraction system

The experiment for the search of the electric dipole moment (nEDM) [Alt10] of the free neutron is situated in the Neutron Guide Hall East of the FRM II roughly 30 m away from the ultra-cold neutron source. Thus a highly efficient extraction and transportation system for the UCN is of utmost importance.

The first step is the extraction of the UCN out of the deuterium itself. Several effects contribute to the loss of neutrons after downscattering into the UCN regime.

- Assuming that UCN are produced with an isotropic momentum distribution in space, half of the neutrons will have a momentum vector in the direction towards the aluminium vessel and the cryogenics supply. If the UCN exceed the critical velocity of aluminium ( $v_c = 3.2 \text{ m/s}$ ,  $V_F = 54 \text{ neV}$ ) the UCN will enter the aluminium and will be lost there. Since the neutrons gain 107 neV upon leaving the deuterium, almost all neutrons with the wrong momentum direction will be lost. The Al vessel can be covered with a layer of Ni ( $V_F = 252 \text{ neV}$ ) in order to reflect the UCN back into the deuterium.
- Thermal upscattering of the UCN caused by 1-phonon scattering of the neutrons on the deuterium lattice is one of the major losses. The temperature dependence of the upscattering cross-section is even more critical. At 5 K

$\sigma_{\text{up}}$  is  $\sim 0.25$  barn, whereas it increases to  $\sim 2$  barn at 10 K [Liu00]. Since the deuterium of the UCN source is cooled only from the back side, there will be a temperature gradient within the deuterium especially with the surrounding walls at 400 K due to radiative heating.

- UCN can also be upscattered on para-deuterium molecules (cf. chapter 3 for details). The cross-section for this is 31 barn and almost temperature independent [Liu00].
- Ultra-cold neutrons can be absorbed in the deuterium or any hydrogen contamination within the  $\text{D}_2$ . The absorption cross-sections at 2200 m/s are 0.519 mbarn for deuterium or 332.6 mbarn for hydrogen respectively [Sou86]. From this one can see that the purity of the  $\text{D}_2$  used for the UCN source needs to be at least 99.99 %.

Additional to these loss effects there are several types of scattering of the UCN which can lead to the eventual loss of the neutron. These types include isotropic elastic scattering, small angle scattering and incoherent elastic scattering on crystal cracks and other defects of the crystal lattice [Bry07].

### 2.4.1. Replika guides

Once the ultra-cold neutrons are produced and extracted out of the deuterium crystal they have to be transported to the experiments. Since the UCN are produced near the reactor fuel element they have to be transported through an area of high radiation until they reach the biological shielding of the reactor. For this reason one cannot simply use glass guides with a reflective surface sputtered onto it. Glass guides would not withstand the high radiation fluence.

At the E18 chair of the Technical University of Munich a new type of so-called “Replika” guides has been developed [Hub11]. These guides are made of a Nickel-Vanadium (NiV) alloy. The NiV is sputtered onto a glass target until a layer thickness of  $\sim 100$  nm is reached. Then a layer of pure Ni is electroplated onto the NiV until it reaches a total thickness 0.5 mm. The layer is then loosened from the glass, thus replicating the roughness of the glass surface. Afterwards the flat piece is rolled to a round guide and electron beam welded along the seam. These guides have lengths of 500 mm per piece.

Figure 2.3a shows an atomic force microscopic (AFM) picture of the surface of a Replika piece. One can see some dents and spikes and dust on the surface but the majority of the surface is flat within 1 nm. This can be seen on the zoomed figure 2.3b.

Figure 2.4 shows the autocorrelation function  $G(r)$  calculated from Figure 2.3b. It quickly drops to half the maximum value ( $r = 0$  not shown in fig. 2.4 at about

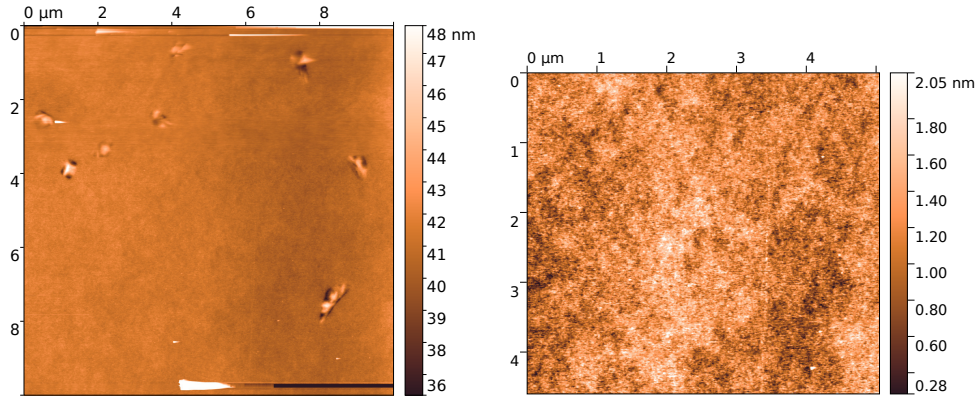


Figure 2.3.: Atomic force microscope (AFM) picture of the Replika guide surface. (a) Full  $10\ \mu\text{m} \times 10\ \mu\text{m}$  scan. (b) Zoom on an area without scratches and dust particles. The surface is flat within 1 nm.

20 nm. This indicates that the nano-structures on the surface of the Replika piece have a characteristic lateral dimension of 40 nm. One can also see another peak in the plot at  $1.5\ \mu\text{m}$  indicating that the surface also has a certain “waviness” with a repeating surface structure.

#### 2.4.2. Beam tube exit into the experimental hall

Figure 2.5 shows a floor plan of the experimental hall and the adjacent neutron guide hall east. After the UCN leave the biological shield of the reactor they first pass through a safety buffer volume. The UCN guide in this section will be S-shaped. If the aluminium converter vessel was damaged in some way so that the liquid helium can evaporate into the guide volume, this safety vessel will contain

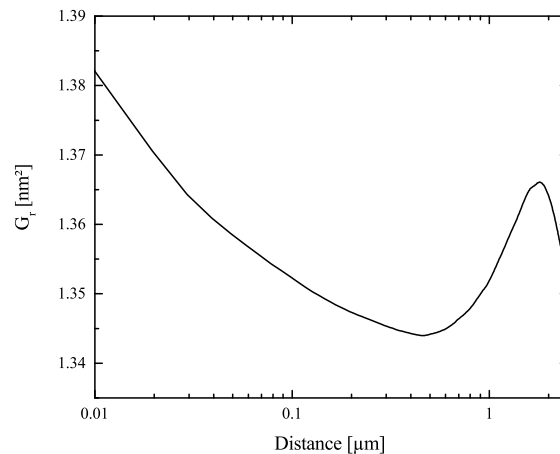


Figure 2.4.: Radial autocorrelation function calculated from Figure 2.3b. There is a strong correlation up to 20 nm and another longer correlation at  $\sim 1.5\ \mu\text{m}$ .

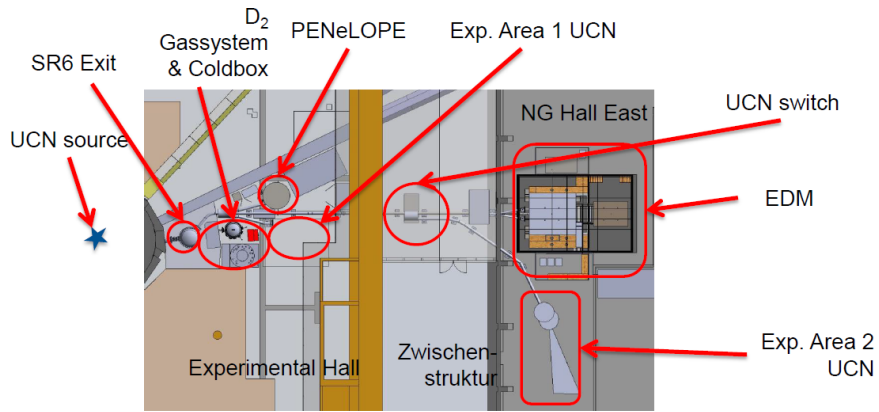


Figure 2.5.: Floor plan of the experimental hall with the guide system for the ultra-cold neutrons.

all of the 8.7 kg of helium inside. In this case the UCN guide would be moved aside by the pressure of the evaporating helium so that it can easily flow into the safety volume. This will also happen any time the source is heated up, so that the deuterium is evaporated.

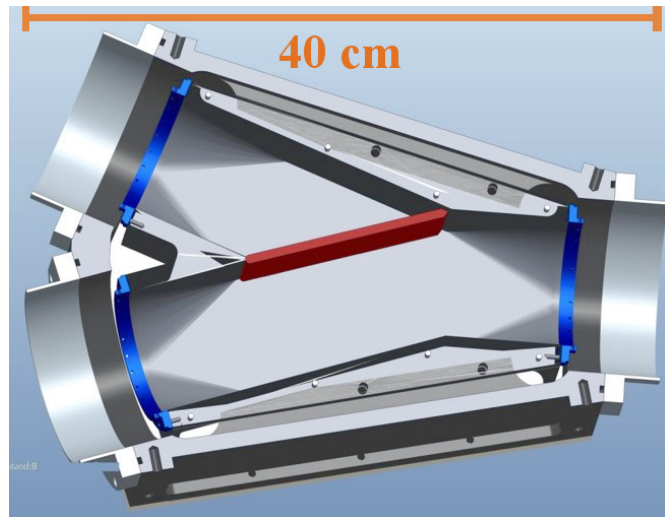


Figure 2.6.: Cut view of the UCN switch foreseen for the UCN guide system. A flap valve (red in the picture) controls the UCN flux into either direction.

### 2.4.3. UCN switches

After passing the SR6 exit the UCN will be guided to the experiments (see figure 2.5). The first of these experiments will be the neutron lifetime experiment PENELOPE (cf. chapter 1.4.1, [Pic05, Mat09]). Within the experimental hall of the FRM II there will also be a second experimental area which will be occupied based on a proposal round system. The other experiments located at the Munich UCN source will be in the neutron guide hall east. There will be another experimental area given away in a proposal system and the nEDM experiment (cf. chapter 1.4.2, [Alt10]).

In order to supply all these experiments with ultra-cold neutrons, highly transmitting UCN switches are needed. A new type of such switches has been developed and tested (see figure 2.6). The switch contains a flap valve which will direct the complete flux to one direction (left or right) or if put into the middle position it directs half the flux into either direction. A transmission of  $0.919 \pm 0.011$  has been determined if the complete UCN flux is diverted into one of the outputs. By using several of these switches one can supply all of the planned experiments.

Such a design can also be used by the experiments itself. The UCN can be filled into an experiment on one side of the switch and after the storage time, they can be directed to a neutron detector which is located on the other port of the switch.

# Chapter 3.

## Deuterium

---

Deuterium will be used as the main part of the new ultra-cold neutron source at the Forschungs-Neutronenquelle Heinz Maier-Leibnitz (FRM II). This chapter discusses some of the properties of deuterium which are crucial to the UCN source. Thus, it will focus mainly on the solid properties.

### 3.1. Thermophysical properties

Chemically, deuterium behaves very much like hydrogen. It has a natural abundance of 0.015%. Figure 3.1 shows the phase diagram of deuterium. The triple point can be identified lying at  $T = 18.7\text{ K}$  and  $P = 171\text{ mbar}$  [Sou86].

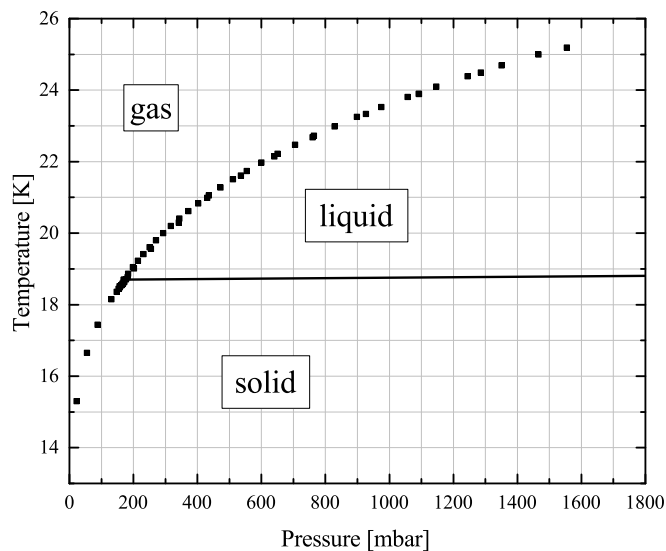


Figure 3.1.: The phase diagram of deuterium. The triple point lies at  $T = 18.7\text{ K}$  and  $P = 171\text{ mbar}$  [Sou86]. The data points were taken from [Hog51, Dia85, Gil34, Jen80]. The solid line represents the melting curve.

The deuterium nucleus, the deuteron, is a compound nucleus made from a proton and a neutron. The binding energy is 2.2 MeV [Kes99]. It is a spin 1 particle and thus, a boson.

## 3.2. Crystals from cryogenic $D_2$

When solidifying one can either go through the triple point via cooling down along the vapour pressure line or if the cold deuterium is connected to a buffer volume at a constant pressure one first liquefies the gas and afterwards goes through the liquid  $\rightarrow$  solid transition.

In any of those two cases solidification of deuterium requires great care and a slow and steady temperature gradient. The molar volumes of the liquid and solid phase at the triple point differ by as much as 12% [Sou86]. Thus, making the liquid  $\rightarrow$  solid transition too fast, very likely results in a darkened, opaque crystal. During the course of this work, it was found that temperature gradients of less than 50mK/h are sufficient to get a clear, transparent crystal. It is also helpful to have a temperature gradient along one axis of the cell, in which the deuterium is frozen. Bringing the solid down to  $\sim 5$  K should be done at temperature gradients not exceeding 1 K/h. During the change in temperature from 18K to 5K deuterium shrinks by 2.2%. Cooling down faster than the gradient mentioned before again results in cracking of the crystal. This then adds considerably to the neutron scattering properties which has been extensively studied in [Bry07].

Solid deuterium at high  $J = 0$  concentrations (high ortho concentration) will freeze out in the hcp lattice structure, although deuterium snow at 5 to 7K can also form in the fcc lattice [Kru78].

## 3.3. Ortho- and para-deuterium

One peculiarity of the hydrogen family is of particular importance for the production of ultra-cold neutrons. This is the capability of the hydrogens to have energy stored in its rotation about the center of the hydrogen molecule. This chapter will focus on this very phenomenon.

### 3.3.1. Definition

A homonuclear, diatomic molecule such as hydrogen and deuterium is subject to the symmetry rules of quantum mechanics. Hydrogen and deuterium differ in the fact that the former nucleus is a spin  $s = \frac{1}{2}$  fermion, while the latter is a  $s = 1$



boson. Thus, in the case of hydrogen the total molecular wave function needs to be antisymmetric with respect to particle permutation while it needs to be symmetric in the case of deuterium.

The molecular wave function can be split into three parts: nuclear, rotational and vibrational.

$$\Psi_{\text{mol}} = \Psi_{\text{nuc}} \Psi_{\text{vib}} \Psi_{\text{rot}} \quad (3.1)$$

The vibrational part is manifestly symmetric [Sil80]. The nuclear spin  $S$  and the rotational quantum number  $J$  are either symmetric (S) or antisymmetric (AS). Table 3.1 sums up the different allowed combinations for hydrogen and deuterium.

Table 3.1.: Para- and Ortho- definitions in the different molecular hydrogen species.

Species	Spin	Rotation	Degeneracy	Designation
Hydrogen	$S = 0$ (AS)	even- $J$	$g_s = 1$	para
	$S = 1$ (S)	odd- $J$	$g_s = 3$	ortho
Deuterium	$S = 0, 2$ (S)	even- $J$	$g_s = 6$	ortho
	$S = 1$ (AS)	odd- $J$	$g_s = 3$	para

Historically, the ortho-species was defined to be species with the greatest degeneracy. This is why for hydrogen the odd- $J$  states are designated “ortho” while in deuterium it is the even- $J$  states. Since this causes a lot of confusion, throughout this work the following definition will be used: The designation “ortho” and “para” will always mean deuterium species as given in table 3.1. For all other purposes and explicitly when talking about deuterium and hydrogen at the same time, even and odd  $J$  will be used. Fig. 3.2 shows a scheme of the rotational levels of deuterium. The ortho levels have even rotational quantum numbers  $J$ , while the para levels have odd  $J$ . For temperatures below 20 K only the lowest rotational levels  $J=0$  and  $J=1$  will be occupied, so that the ortho-/para ratio and the rotational level occupation ratio coincide:  $\frac{c_{\text{ortho}}}{c_{\text{para}}} = \frac{P(J=0)}{P(J=1)}$ .

### 3.3.2. Ortho to para conversion

This chapter shall give a quick overview over the different possibilities to convert deuterium sufficiently into its ortho species.

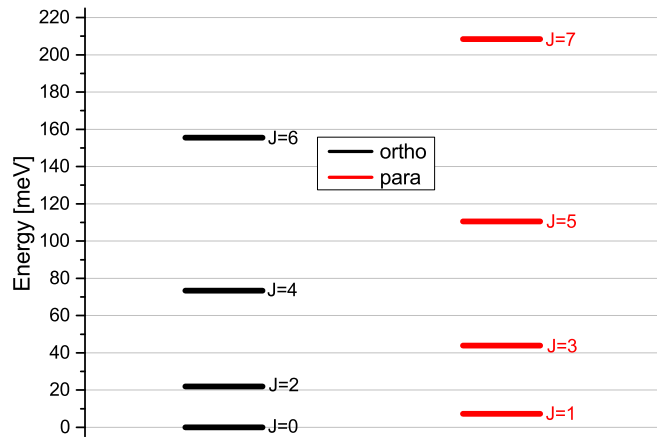


Figure 3.2.: Level scheme of the rotational levels of deuterium. The black bars show the ortho levels (even rotational numbers) and the red ones show the para levels (odd numbers). The lowest para level has an excitation energy of 7.3 meV.

### Natural conversion

For single deuterium molecules only transitions with  $\Delta J = \pm 2$  are allowed. Thus it will stay in its respective ortho or para state. A change from ortho to para-deuterium would require a change of the spin state with a simultaneous change of the rotational state of the molecule which is highly suppressed due to the magnetic moment of deuterium only being one third that of hydrogen [Mot56]. Nonetheless the  $J = 1$  content within a macroscopic deuterium sample is a function of temperature as depicted in figure 3.3.

For temperatures above 100 K the para concentration is at its high-temperature equilibrium value of  $\frac{1}{3}$ . At the triple point temperature of 18.7 K the concentration has a value  $c_p = 1.5\%$ . Transitions between the two species is mediated

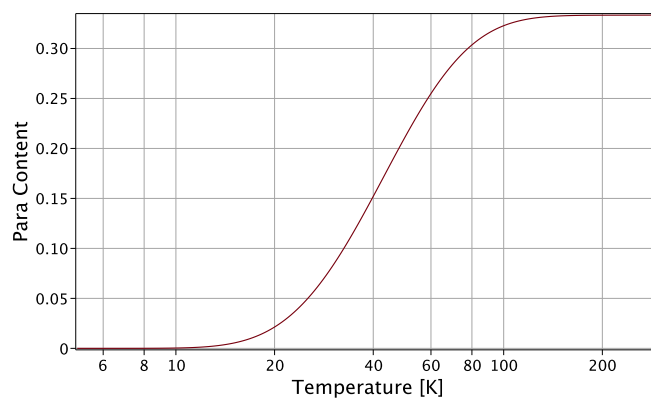


Figure 3.3.: The deuterium para concentration vs. temperature. The values change significantly only for temperatures well below 100 K.

through two types of interactions [Mot56]: The first type is a dipole-dipole interaction between  $D_2$  molecules which are either an interaction between the respective spins of two molecules or an interaction between rotational magnetic moment of one molecule with the nuclear spins of the other one. The second type of interaction is the coupling of the nuclear quadrupole moment and the total quadrupole moment of the other molecule.

The natural conversion of para to ortho  $D_2$  happens at a rate of  $6 \cdot 10^{-4} \text{ h}^{-1}$  [Sil80]. So it takes roughly half a year for deuterium to completely self convert to acceptable para concentrations in a UCN source. This gives rise to the need of a rapid conversion mechanism, which will be discussed in the next sections.

### Catalyzed conversion

As already stated above the change from para to ortho deuterium requires a spin flip and thus a strong magnetic moment in the vicinity of the  $D_2$  molecule. Such a magnetic moment can be found in oxidized materials which leave electrons in the shell of the oxygen atom unpaired. The typical choice for such materials is either chromium-oxide ( $CrO$ ) or ferrous hydroxide ( $Fe(OH)_2$ ).

The typical catalysis procedure is to have a evacuated cell filled with the catalyser material at a temperature slightly above the critical point. The deuterium is then liquefied into the cell and boiled at vapour pressure conditions for several hours or days. With this method it could be shown that the conversion rate can be enhanced up to values of  $0.35 \text{ h}^{-1}$  [Fre08].

### Radiation-assisted conversion

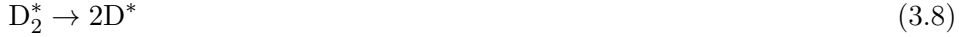
Besides catalytic materials the ortho-fraction in deuterium can also be increased by irradiation. Since a great part of this work deals with deuterium irradiation and its effects on the para-ortho ratio, this type of conversion shall be explained in more detail in this section. It is well established that atomic deuterium produced by radiation effects is responsible for the  $J = 1 \rightarrow 0$ -transition in deuterium [Sou86, Col91, Atc03, Sat88, She94]. Atomic deuterium is paramagnetic, because of its unpaired single electron. Thus, it provides the necessary magnetic moment to flip the spin of the surrounding molecules.

In essence, any kind of radiation, be it neutron,  $\gamma$ , or  $\beta$  radiation will ionize the deuterium either directly through electromagnetic interactions or indirectly by first colliding with an atom, which then causes ionization. The main ionization

processes in deuterium are[Sou86]



Lower energetic particles may also excite the electronic system of the deuterium without ionizing it, leading to the following reactions [Sou86].



This leads to 1.14 directly formed atoms per created ion pair [Sou86]. Since  $\text{D}_2^+$  is only stable in high vacuum, it will convert to  $\text{D}_3^+$  according to [Sou86]



This leads to another free deuterium atom, now formed indirectly. The  $\text{D}_3^+$  ions will at some point recombine with an electron according to the reaction [Sou86]



This reaction is the main source of atomic deuterium under irradiation. On average there will be  $5.1 \pm 0.3$  atoms created per ion pair [Sou86]. Even though this value has been determined in hydrogen gases, experiments have shown that it still holds true in solids [Col91].

Based on the work of [Col91, Atc03], in the following paragraphs there will be derivation of an expression for the  $J = 0$  content in the ultra-cold neutron source of the FRM II. The conversion to ortho-deuterium due to irradiation can be written in the following way

$$\begin{aligned} \frac{\partial[\text{D}_2^o]}{\partial t} &= -\frac{1}{2}k[\text{D}_2^o] \\ &\quad + \beta(T) [\text{D}]c_o^{\text{eq}}(T) [\text{D}_2^p] \\ &\quad - \beta(T) [\text{D}] (1 - c_o^{\text{eq}}(T)) [\text{D}_2^o] \\ &\quad + \frac{2}{3}\alpha(T) [\text{D}]^2. \end{aligned} \quad (3.11)$$

Hereby,  $[\text{X}]$  denotes a number density. All of these quantities in square brackets in eq. 3.11 are time- and temperature dependent. Eq. 3.11 omits the terms for self-conversion, which is assumed to be much slower than the irradiation conversion. The first term describes the molecular break-up of deuterium, in this case only of the  $J = 0$ -fraction. The atom production rate  $k$  can be calculated, knowing that for every 36.6 eV lost by the irradiation particle, one ion-electron-pair is created

[Whi63], and that 5.1 atoms are created per ion [Sou86]. In the case of the UCN source this yields a value of

$$k = 3.65 \cdot 10^{-7} \text{ s}^{-1} \quad (3.12)$$

using the values for the  $\gamma$  irradiation of the UCN source found in [Rö09]. The second and third term in eq. 3.11 describe the transitions between ortho- and para-deuterium. The transition rate  $\beta(T)$  was set equal for both transitions. This is likely not perfectly correct, but the respective transition rates are on the same order of magnitude [Sat88]. The transitions pull the para-ortho-ratio towards the equilibrium value  $c_o^{eq}(T)$ . The last term in eq. 3.11 describes the recombination of two deuterium atoms to form a molecule. The binding energy of deuterium is 4.55 eV, so the recombination takes place at the high temperature limit, meaning that two-thirds of the deuterium will recombine in the ortho state.  $\alpha(T)$  is the recombination rate, which is a strong function of the temperature. An expression for it can be found in [Isk86].

The time dependence of the atomic deuterium density [D] can be neglected, since the conversion from ortho to para deuterium is much slower than the time needed to saturate the atomic deuterium concentration. Thus, a solution for eq. 3.11 can be found.

$$\begin{aligned} [D_2^o] = & \frac{1}{3(2 \cdot W_{op} + k)} \cdot \\ & \cdot \left[ \left( 3[D_2] \left( 2 \cdot W_{op} (c_0 - c_o^{eq}(T)) + k c_0 \right) - 4W_r[D] \right) e^{-\frac{1}{2}(2 \cdot W_{op} + k)t} + \right. \\ & \left. + 6c_o^{eq}(T) W_{op}[D_2] + 4W_r[D] \right] \end{aligned} \quad (3.13)$$

$c_0$  is the ortho concentration at  $t=0$ ,  $W_{op} = \beta(T) [D]$  and  $W_r = \alpha(T) [D]$ . The atomic deuterium density [D] can be calculated with [Ros76, Atc03]

$$\frac{d[D]}{dt} = k[D_2] - 2\alpha(T) [D]^2. \quad (3.14)$$

Eq. 3.13 has been calculated under the assumption that the atomic deuterium density [D] is in its equilibrium value  $\lim_{t \rightarrow \infty} [D](t) = \sqrt{\frac{k[D_2]}{2\alpha(T)}}$ . [D] will reach its equilibrium value after roughly one day. For temperatures above 9 K where the ortho-para-equilibrium is reached after several days, taking the equilibrium value for [D] is a good assumption. For the values below 9 K this assumption does yield wrong values for the time constants involved. On the other hand the ortho concentrations for  $t \rightarrow \infty$  are still correct. For any practical purposes this does not pose a significant problem.

Getting an expression for  $\beta(T)$  is a bit more difficult. Values for conversion rates of deuterium have only been measured in a D–T mixture [Col91]. For tritium the self-conversion due to irradiation has also been measured [Sat88]. Both papers

see the transition rate  $W_{\text{op}}$  at roughly  $10^{-4} \text{ s}^{-1}$  at 5 K. For the calculations done here, the values from [Col91] for 5 K have been used to yield

$$\beta(5 \text{ K}) = \frac{W_{\text{op}}}{[\text{D}]} = 4.3 \cdot 10^{-24} \text{ cm}^3 \text{ s}^{-1}. \quad (3.15)$$

The temperature scaling for  $\beta$  is now also taken from [Col91].

$$\beta \propto qD \quad (3.16)$$

The value  $q$  is the probability for a deuterium atom in a single site to convert a neighbouring molecule and  $D$  is the diffusion constant. An expression for  $D$  can be found in [Ebn72] and  $q$  can be written empirically as [Col91]

$$q = 1 - e^{-t_{\text{D}}/t_0} \quad (3.17)$$

with  $t_0$  being the shortest time for which  $q$  is just 1 and  $t_{\text{D}}$  being the average time an atom spends at its site

$$t_{\text{D}} = \frac{R_0^2}{4D}. \quad (3.18)$$

With the intermolecular distance  $R_0 = 3.6 \cdot 10^{-8} \text{ cm}$  [Sou86] and  $t_0 \sim 1 \text{ s}$  [Col91] one can now write

$$\beta(T) = \frac{\beta(5 \text{ K})}{q(5 \text{ K}) D(5 \text{ K})} q(T) D(T). \quad (3.19)$$

Figure 3.4 shows the ortho concentration in the UCN source for the  $t \rightarrow \infty$  case of eq. 3.13. One can see that up to 9 K the deuterium will be almost completely in its  $J=0$  state. For higher temperatures there is a sharp drop almost down to the high temperature equilibrium values of the ortho concentration. This is in contrast to measurements on tritium where only minor deviations from the thermal

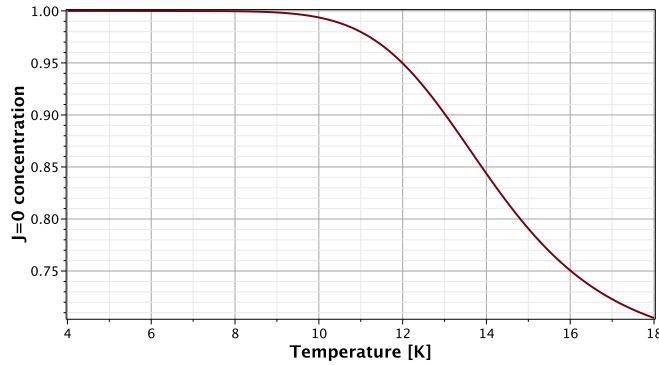


Figure 3.4.: The  $J=0$  concentration in the UCN source depending on the temperature. Up to 9 K the deuterium will be completely in its ortho state. At higher temperatures the ortho concentrations drop rapidly towards the high temperature equilibrium due to the recombination of deuterium atoms.

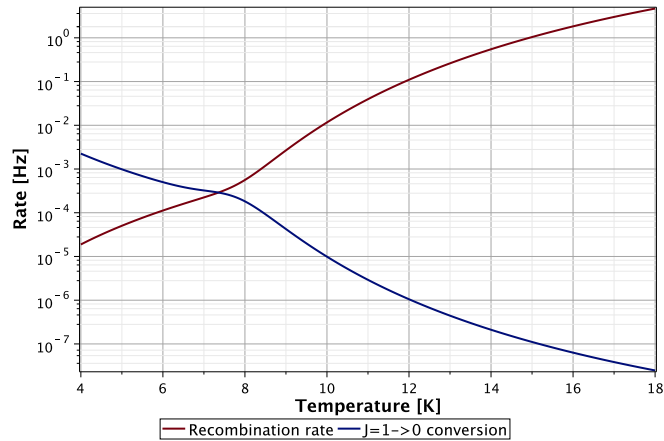


Figure 3.5.: The recombination rate and  $J = 1 \rightarrow 0$  conversion rate compared over temperature.

equilibrium values were found due to irradiation [Sat88]. The reason for this is the unusually high temperature dependence of the diffusion and recombinations constant in solid deuterium [Isk86, Sat88, Col91]. While in tritium at temperatures between 10 – 15 K the atoms formed from irradiation still have enough time to convert tritium to the  $J = 0$  state before they recombine, the picture in deuterium is completely different. The atoms recombine too quickly and as explained before the newly formed molecules will have the high temperature equilibrium ortho concentration. This can be seen in figure 3.5. The recombination rate is increasing by several orders of magnitude while the conversion rate  $J = 1 \rightarrow 0$  goes down by orders of magnitude. Since both quantities are governed by the atom density, they have the same line shape.

A measurement of this strong irradiation effect on solid deuterium would be very interesting not only with regard to the ultra-cold neutron source planned at the FRM II. Such a measurement would be governed by the time constants involved for the different temperatures. In figure 3.6 the ortho concentration is plotted versus the irradiation time. There are big differences in the conversion time depending on the temperature especially in the region from 8 – 10 K. To measure the effect, one would irradiate a deuterium crystal for one day at different temperatures while constantly measuring the  $J = 0$  concentration by one of the methods discussed in section 3.3.3.

### 3.3.3. Measurement of the ortho-para ratio

The ortho-fraction in deuterium under irradiation can vary between  $\frac{2}{3}$  and 1 as was shown previously. It is crucial to determine the ortho-para-ratio in a fast and reliable way. Some of the possible methods will be discussed in this section.

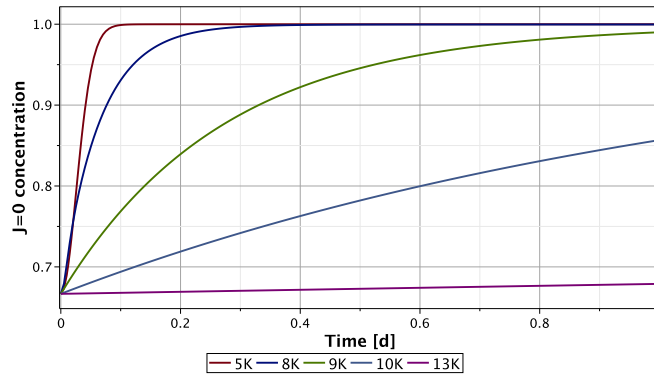


Figure 3.6.: Deuterium ortho concentration under irradiation over the course of one day for different temperatures.

### Raman spectroscopy

Raman scattering is the inelastic scattering of light off solids as opposed to Rayleigh scattering, where the light scatters elastically. Photons can only change the rotational quantum number by  $\Delta J = \pm 2$  and therefore cannot change the ortho and para states. Figure 3.7 shows an exemplary Raman measurement on a gaseous sample with natural ortho-para-composition. One can clearly distinguish the different rotational level changes. The peaks labelled  $S(0)$ ,  $S(1)$ , ... correspond to the transitions  $J = 0 \rightarrow 2$ ,  $J = 1 \rightarrow 3$ , and so on. Raman scattering has been used throughout this work to determine the ortho-para-ratio, since it allows an absolute measurement. When applied to solid deuterium, there is one peculiarity one has to keep in mind. The  $J = 2$  states are non-degenerate as opposed to the  $J = 0$  ground state. Out of the ten possible  $J = 2$  states only three couple to the ground state. Thus, a splitting of the first transition into three separate peaks can be observed [VK60, Bha62].

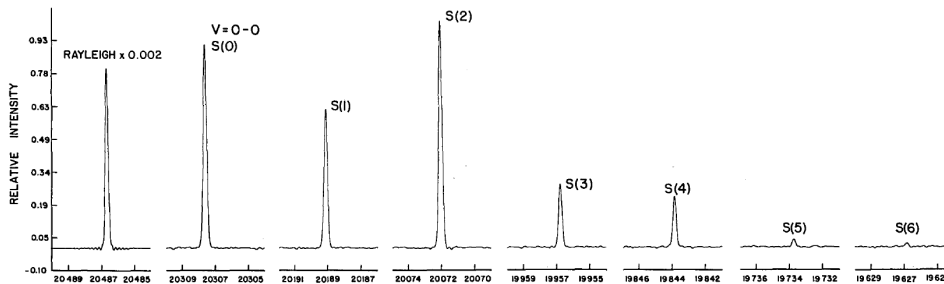


Figure 3.7.: Picture taken from [Jen86]. Raman measurement on a gaseous deuterium sample with natural ortho-para-ratio.



## Nuclear magnetic resonance

Nuclear Magnetic Resonance (NMR) techniques have been widely used in the study of the fundamental quantities of the hydrogen family. It uses the difference in molecular spins to determine the ortho-para-ratio. It has been especially successful in the determination of mobility and recombination rates within hydrogen crystals and in the determination of conversion rates in the solids [Isk86, Col91, Sat88]. NMR was not used during the course of this work, partly because of space reasons, because in the experimental area for the irradiation experiment hardly any additional space would be available. Also, an NMR setup is quite costly, since it requires a strong magnet with several teslas of magnetic field.

## Thermal conductivity

The thermal conductivity in solid hydrogens changes significantly with the  $J=1$  content. As one can see from figure 3.8 the thermal conductivity of solid deuterium changes by more than one order of magnitude between the natural composition and an almost complete  $J=0$  crystal. This means that if one is able to measure the thermal conductivity accurately enough, one can determine the  $J=1$  content of the sample.

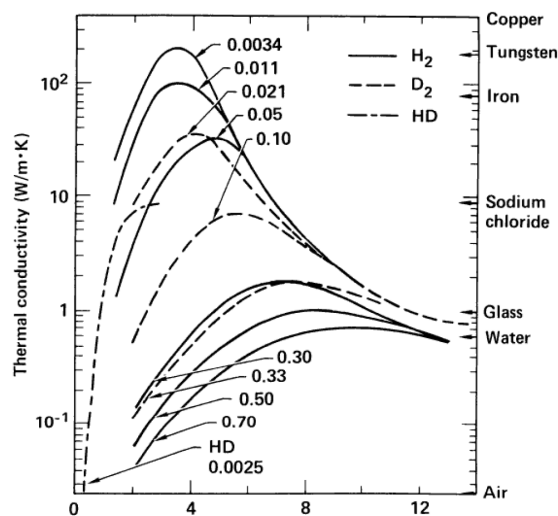


Figure 3.8.: Comparison of thermal conductivities of different hydrogen species with different  $J=1$  concentrations [Sou86].

Measuring the thermal conductivity of cryocrystals is quite challenging. As mentioned before deuterium shrinks and cracks during solidification and further cooling. This causes it to detach from surrounding walls which makes accurate measurements of the thermal conductivity difficult. A newer approach is to use the so-called  $3\omega$  method [Cah90]. In this method a single wire with an AC current

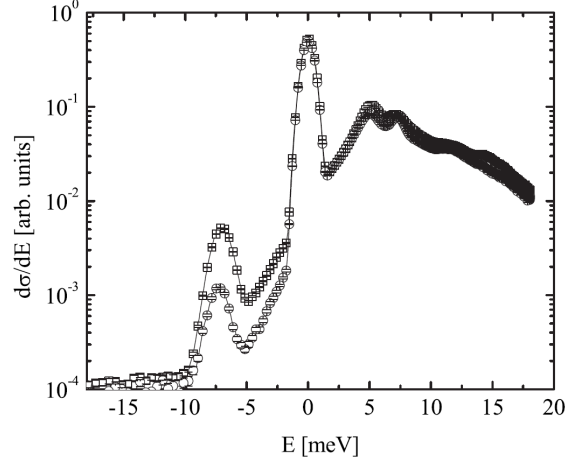


Figure 3.9.: Dynamical scattering cross-section of solid deuterium at 7 K. The square symbols show the natural para-ortho ratio. The circles show  $c_o = 98\%$ . [Fre09]

is used as heater and thermometer. It has been shown that this method can work down to 13 K [Gra12] and yield values which are in good agreement with literature [Sch14]. Unfortunately the method is limited to temperatures between 8 – 10 K depending on the purity of the platinum wire, which makes an accurate measurement of the ortho-para-content difficult, as can be seen in fig. 3.8.

### 3.3.4. Possible para-enrichment through neutrons

The radiation assisted conversion from para to ortho-deuterium is mainly driven through the  $\gamma$  radiation onto the deuterium and in small parts through fast neutrons bombarding the crystal. Fig. 3.9 shows the dynamical scattering cross-section of  $D_2$  at 7 K. The peaks at  $\sim 7.5$  meV on either side of the elastic scattering peak correspond to scattering on the rotonic excitation. On the energy loss side (positive values) this corresponds to a  $J=0 \rightarrow 1$  transition of a  $D_2$  molecule. A quick estimate on the order of magnitude of this effect shall be done here.

The scattering cross section for the particular channel can be estimated as [Mor15]

$$\frac{d^2\sigma}{d\omega d\Omega}(J=0 \rightarrow 1) = c_o \frac{k'}{k_0} (2b_{\text{eff}})^2 j_1^2\left(\frac{\bar{q}a}{2}\right) e^{-\frac{\langle u^2 \rangle \bar{q}^2}{3}} \cdot 3 \cdot \delta(\omega' - \omega_0) \quad (3.20)$$

For thermal neutron scattering  $\frac{k'}{k_0} \approx 1$ . For the transition  $J=0 \rightarrow 1$   $b_{\text{eff}}^2 = \frac{3}{8}b_{\text{inc}}^2$  [Liu00]. The average momentum transfer is  $\bar{q} \approx 1.9 \text{ \AA}^{-1}$ , the average molecule spacing  $a = 0.74 \text{ \AA}$ , the average molecular displacement  $\langle u^2 \rangle = 0.25 \text{ \AA}^2$ . This then

results in a value for the cross-section

$$\sigma(J=0 \rightarrow 1) \approx 0.3 \text{ barn.} \quad (3.21)$$

Even in the peak flux density of the FRM II of  $\phi_{\text{max}} \sim 10^{14} \text{ cm}^{-2}\text{s}^{-1}$  this only results in a conversion rate of

$$R(J=0 \rightarrow 1) \approx 10^{12} \text{ cm}^{-3}\text{s}^{-1}. \quad (3.22)$$

This is orders of magnitude smaller than the radiation assisted catalysis effect discussed before ( $R_{\text{rad}}(J=1 \rightarrow 0) \approx 10^{18} \text{ cm}^{-3}\text{s}^{-1}$ ) and neutronic conversion from ortho to para deuterium can thus be neglected.

### 3.4. Deuterium as superthermal converter

#### 3.4.1. Production of ultra-cold neutrons

In general the UCN production rate  $P$  per unit volume can be written as

$$P = \int_0^{E_{\text{UCN}}^{\text{max}}} \int_0^{\infty} \sigma(E_0 \rightarrow E_{\text{UCN}}) \phi(E_0) dE_0 dE_{\text{UCN}}. \quad (3.23)$$

$\sigma(E_0 \rightarrow E_{\text{UCN}})$  denotes the downscattering cross section from initial thermal energies to the UCN energy regime and  $\phi$  is the flux density at a specific energy. The differential cross section for UCN production can be calculated using the incoherent approximation [Tur65, Yu86]

$$\begin{aligned} \sigma(E_0 \rightarrow E_{\text{UCN}}) = & \sigma_0 \left(1 + \frac{1}{\mu}\right)^2 \frac{\tau}{2E_0} \frac{g(|\epsilon|)}{\epsilon} \left(1 - e^{-\epsilon/k_{\text{B}}T}\right)^{-1} e^{-\frac{E_0 + E_{\text{UCN}}}{\mu\tau}} \cdot \\ & \cdot \left( (E_0 + E_{\text{UCN}} + \mu\tau) \sinh\left(\frac{2\sqrt{E_0 E_{\text{UCN}}}}{\mu\tau}\right) - \right. \\ & \left. - 2\sqrt{E_0 E_{\text{UCN}}} \cosh\left(\frac{2\sqrt{E_0 E_{\text{UCN}}}}{\mu\tau}\right) \right) \end{aligned} \quad (3.24)$$

where  $\sigma_0 = 7.64$  barn,  $\mu$  is the mass ratio between a deuterium atom and a neutron,  $\epsilon = E_0 - E_{\text{UCN}}$ ,  $g(|\epsilon|)$  is the generalized density of states (GDOS) and

$$\tau = \frac{\hbar^2}{2M\gamma}. \quad (3.25)$$

Here  $M$  is the atom mass and

$$\gamma = \frac{\hbar^2}{2M} \int_0^\infty \frac{1}{\epsilon} \coth\left(\frac{\epsilon}{2k_{\text{B}}T} g(\epsilon)\right). \quad (3.26)$$

The GDOS  $g(\epsilon)$  has been measured quite extensively [Nie71, Fre09]. With this one can now calculate the production rate according to eq. 3.23 for the case of the new UCN source at the FRM II. Both the GDOS from the cited papers as well as a Debye phonon spectrum with  $\Theta_{\text{D}} = 110$  K for  $\text{D}_2$  yield roughly the same values of

$$P = 2.1 \cdot 10^5 \text{ cm}^{-3}\text{s}^{-1}. \quad (3.27)$$

### 3.4.2. Losses of ultra-cold neutrons

There are several ways for an ultra-cold neutron to be lost within the deuterium after its production, some of which have already been discussed before.

- Upscattering on a para- $\text{D}_2$  molecule without a phonon contribution
- Upscattering on a  $\text{D}_2$  molecule with a 1-phonon contribution
- Loss due to absorption in the deuterium

From table 3.1 one can see that due to the different degeneracies the ratio  $\frac{J_{\text{even}}}{J_{\text{odd}}}$  will be  $\frac{1}{3}$  for hydrogen and 2 for deuterium. At low temperatures  $< 20$  K only the lowest rotational states  $J = 0, 1$  will be occupied. For deuterium the energy separation between those two states is 7 meV [Sil80]. UCN, that have already been created within the deuterium solid, can scatter on a  $J = 1$  molecule and gain 7 meV energy and are thus lost as ultra-cold neutrons. Figure 3.10 shows the different contributions to the upscattering cross-section in solid deuterium. One can see that the  $J = 1 \rightarrow 0$  relaxation with no phonon involvement is almost

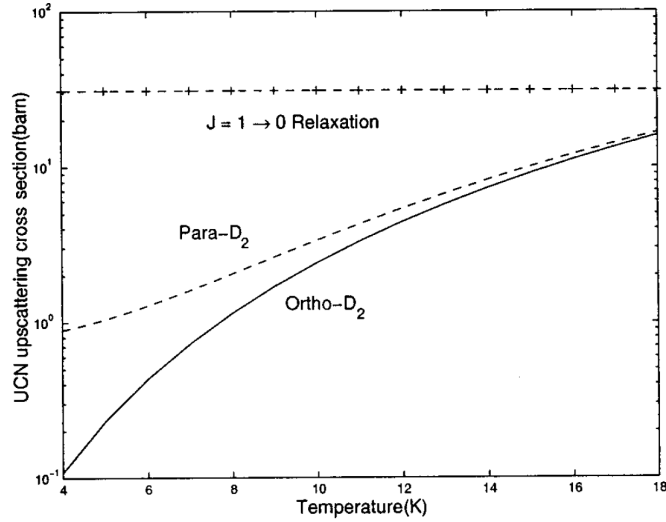


Figure 3.10.: UCN upscattering cross-section vs. temperature. One phonon upscattering in  $J = 0$  (solid line) and  $J = 1$  (dashed) is shown. Also the 0-phonon  $J = 1 \rightarrow 0$  relaxation is shown [Liu00].

two orders of magnitude stronger than the other 1-phonon contributions. Thus, a very low odd- $J$  content of  $\sim 1\%$  is necessary in order to bring the losses of this particular channel down.

The first two cases have been discussed in ch. 3.3.1 and in [Liu00]. Assuming a ortho-fraction of 98.5% which can be easily achieved through catalysis, the lifetime of a UCN in the  $D_2$  volume can be calculated and yields a value of 51 ms at 5 K temperature [Mis04]. For  $c_o \rightarrow 1$ , which could be achieved through radiation catalysis, the lifetime can be increased to 146 ms [Mis04]. These values are on the same order of magnitude as the loss through absorption, which can be easily calculated.

$$\tau_{\text{abs}} = (n\sigma_{\text{abs}}v)^{-1} \approx 140 \text{ ms} \quad (3.28)$$

The total lifetime of a UCN in the deuterium is then

$$\begin{aligned} \tau &= \left( \frac{1}{\tau_{\text{up}}} + \frac{1}{\tau_{\text{abs}}} \right)^{-1} \approx 29 \text{ ms} (c_o = 98.5\%) \\ &\approx 46 \text{ ms} (c_o = 100\%) \end{aligned} \quad (3.29)$$

which in turn yields UCN densities within the converter of

$$\begin{aligned}\rho_{\text{UCN}} &= P \cdot \tau \approx 5800 \text{ cm}^{-3} (c_o = 98.5 \%) \\ &\approx 9300 \text{ cm}^{-3} (c_o = 100 \%) \end{aligned} \tag{3.30}$$

## Chapter 4.

# A radiation assisted conversion experiment

---

In chapter 3.3.2 an expression for the ortho concentration in an irradiated sample was derived. This chapter will focus on the experimental determination of the validity of this expression. In order to do this an experiment was built, set up and conducted at the Munich Tandem-Accelerator lab (Maier-Leibnitz Laboratorium MLL). In two separate beam times at two different temperatures of the deuterium, the parameters of the para-ortho conversion during irradiation could be determined.

### 4.1. Experimental concept

In order to simulate the irradiation of solid Deuterium at the FRM II an experiment was set up for the Tandem-Accelerator in Munich. The general idea was that a  $sD_2$  sample is irradiated by a proton beam and at the same time its ortho concentration is monitored by a Raman spectroscopy setup. In the UCN source at the FRM II gammas will have the biggest contribution to the energy deposition in the deuterium converter. In the experiment described here, protons will be used, because the effect of protons and gammas on the deuterium is fairly similar. Both particles will ionize the solid which then leads to the formation of single atoms. The difference between the two incident particles is the rate, at which they dissociate the deuterium. Knowing the energy deposition of the respective particles in the material, it is possible to extrapolate from the proton measurement to the case of gamma irradiation. Another difference is that the protons will be stopped within the solid. This, however, is a negligible effect since the total number of protons used in the experiment will be many orders of magnitude below the number of deuterium molecules, so that the measurement device will be unable to detect the protons.

The following chapters will discuss the experimental setup and its parts in closer detail.

## 4.2. The experimental setup

The experiment is divided into three separate parts. First, the irradiation cell, which contained the solid deuterium and could be held at different temperatures. For this purpose the cell was mounted on a cold head and could be heated with a resistive heating element. A transparent window was mounted on one side of the cell, so that the Raman light could enter. The cell was set into an isolation vacuum to shield it against convection heating from the walls. The second part was the Raman optics and spectrometer. The optics transported the light from the laser source to the cell, where the laser beam was focussed into the cell. The light then took the same path back. A dichroic mirror separated the Rayleigh and Raman scattered light, so that mostly the Raman light was transported to the spectrometer via glass fibre. Last but not least, the beam line from the particle accelerator to the experiment had to be built. It consisted of two X slit systems and one Y slit system, which could measure deviations of the beam center and also the lateral extent of the beam. A two stage quadrupole focussing lens was used to focus the proton beam onto the irradiation cell. An X-Y steerer system could divert the beam in the respective directions and a Faraday-Cup could measure the total beam current.

### 4.2.1. Irradiation cell

Figure 4.1 shows the irradiation cell used in this experiment. It was made completely of aluminium ( $\text{AlMg}_3$ ). Aluminium is non-magnetic so there is a negligible effect on the ortho-para-concentration of the deuterium inside the cell. The inner volume of the irradiation cell had a diameter of 12 mm and a length of 17 mm which resulted in a cell volume of  $V_{\text{D}_2} = 1.9 \text{ cm}^3$ .

The cell was mounted on a cryo cooler with power of 1.5 W at 4 K (Sumitomo Heavy Industries RDK-415D with CSW-71 compressor). With this it was possible to cool the experiment down to temperatures of 7 K. Lower temperatures were not possible due to the two holes in the cryo-shielding for the laser and the proton beam. The temperature could be monitored with two sensors of the Cernox type (CX-1050-AA). The sensors were located directly below and above the irradiation volume. A small ( $\varnothing 4 \times 40 \text{ mm}$ ) resistive heater was used to regulate the temperature of the cell. The heating power was controlled by a LabView PID loop, so that a desired, constant temperature was achieved. With this setup it was possible to freeze deuterium in a clear, transparent crystal.

The protons were fed into the deuterium from the left in figure 4.1. Before entering the inner volume of the cell, the protons had to pass an aluminium window with a thickness of 1.5 mm. The protons lost part of their energy in the transmission process. Initially they had an energy of 20.5 MeV. After passing through the window they had an average energy of  $E_p \approx 11 \text{ MeV}$  [Ber05]. In the second



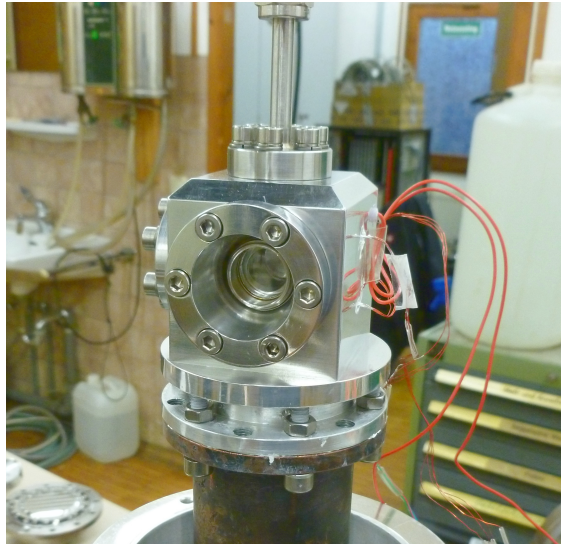


Figure 4.1.: Aluminium ( $\text{AlMg}_3$ ) irradiation cell used in the experiment. The proton beam came in from the left. The Raman laser was focused into the cell from the front side. The cell was cooled by a Sumitomo Heavy Industries RDK-415D cryo-cooler from below. The deuterium gas was filled in from the top.

beam time the thickness of the entrance window was reduced to 1.0 mm, so that the protons had an entrance energy of  $\approx 16$  MeV and could penetrate the whole crystal. From the entrance window on, the protons lose energy as discussed in chapter 3.3.2 until they are stopped on average 6 mm behind the entrance window (for the first beam time) or almost at the end of the cell (for the second beam time). This has been simulated beforehand with the SRIM software package [Zie10].

Deuterium gas was fed into the cell from the top. A one meter long  $\varnothing 8 \times 1$  mm stainless steel tube, which connects the irradiation cell to the gas connector of the vacuum vessel, ensured low thermal conductivity to the cell. The gas handling system consisted of a  $\sim 15$  l dump volume, a vacuum meter (Leybold ITR90), a vacuum pump, a digital manometer to measure the dump pressure, and several valves to control the gas flow into the dump and into the cell. A needle valve was used to slowly feed gas into the irradiation cell. Directly outside of the isolation vacuum of the cell, a pressure meter (tecsis P3249S073101) was installed to monitor the pressure inside the cell. In the case of sudden evaporation of the crystal and a subsequent rapid pressure increase, a safety valve opened to let the gas flow back into the dump.

The laser light entered the cell from the front which is made from a CF16 window flange. The whole cryo-setup was placed in an isolation vacuum, which had a vacuum sealed glass window in front of the CF16 window flange. An aluminium shield around the cell together with several layers of super-insulation foil reduced the thermal load on the cell due to heat radiation.

### 4.2.2. Raman setup

#### Optics

Focussing the laser beam onto the target and collecting as much light as possible are the most crucial tasks for any kind of Raman type setup, even more so, if the target is within a cryogenic cell enclosed in an isolation vacuum. For this experiment a reflection geometry was chosen, since focus point and collection point are the same by definition. A scheme of the setup can be seen in fig. 4.2.

A laser diode (Thorlabs DJ532-40) with a wavelength of  $\lambda = (532 \pm 1)$  nm and a maximum power of  $P = 40$  mW was used as a light source. According to the manufacturer it had a bandwidth of 30 MHz, which is sufficiently narrow for Raman spectroscopy. The beam was collimated by two plano-convex lenses with  $f = 25$  mm. A mirror diverts the beam by  $90^\circ$ . After that the beam reached a dichroic mirror (SEMROCK LPD02-532RU-25) which acted as a beam splitter. The laser line was reflected with an efficiency of more than 99 % while more than 90 % of the Raman light was transmitted. On the transmitting side a power meter was installed to monitor the laser stability.

Towards the irradiation cell the beam was first widened by two achromatic lenses with  $f = 30$  mm and  $f = 150$  mm respectively. This ensured that the collected light was narrow enough on its way back and did not travel past the dichroic mirror without actually going through. The focussing into the irradiation cell (through the vacuum window and the cell window) was finally realized with a lens pair of a plano-convex and a meniscus lens each with  $f = 300$  mm to yield a combined focal length of  $\sim 150$  mm. Raman light, which had been created in the irradiation cell could now take the same path back. It then passed through the dichroic mirror. Afterwards the beam was narrowed again by a pair of plano-convex lenses ( $f = 50$  mm and  $f = 15$  mm) so that the beam could be focussed into a glass fibre with a core diameter of  $400 \mu\text{m}$ .

#### Raman spectrometer

In order to enter the spectrometer the Raman light needed to be focussed into the entrance slit of the spectrometer. At the end of the glass fibre the light was again collimated by a lens with  $f = 11$  mm. A lens with at least  $f = 100$  mm was needed so that all the light entering the spectrometer would be transported through the device. The combination of those two lenses would magnify the glass fibre spot onto the entrance slit by a factor of  $\sim 9$ . A telescope tube was used to reduce this effect. The space between the two lenses was 5 times as long as between the focussing lens and the entrance slit. Tests showed that the spot on the entrance slit was only  $500 \mu\text{m}$  in diameter.

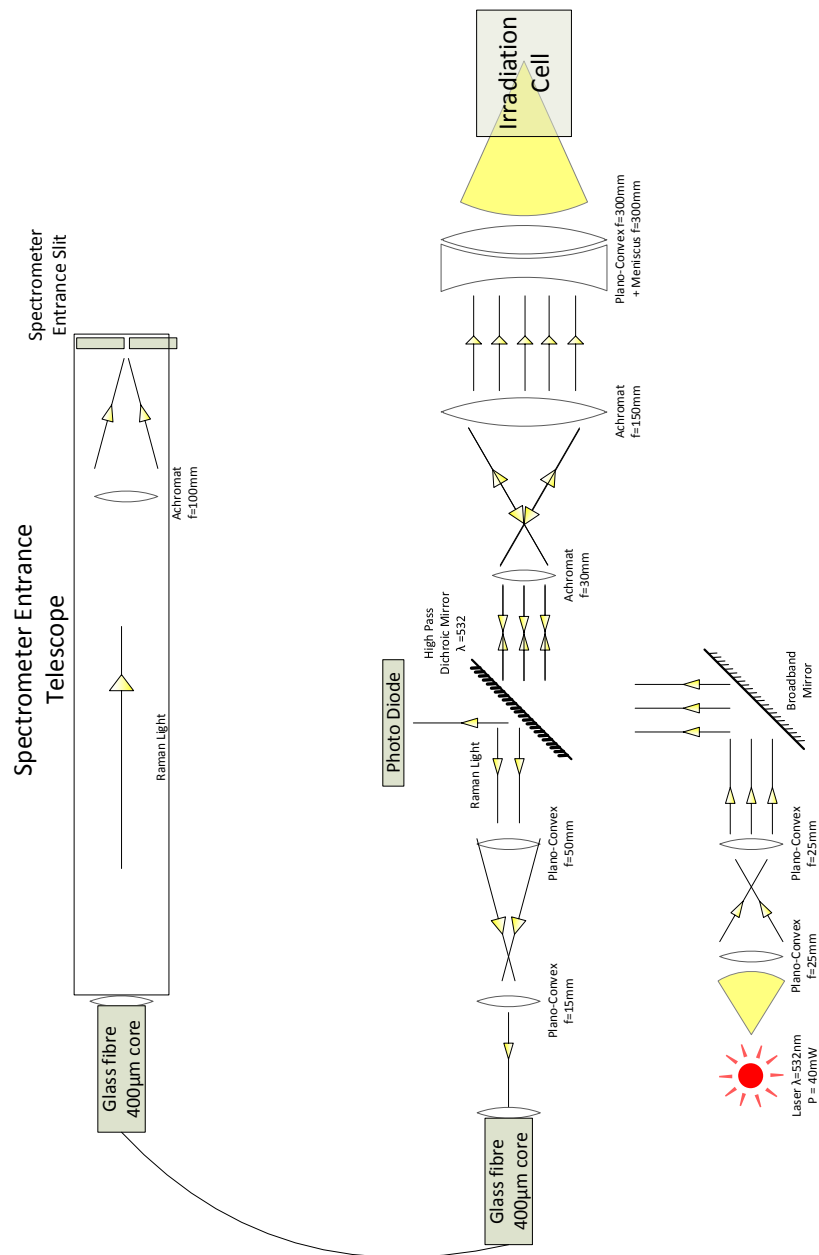


Figure 4.2.: Scheme of the optics used in the experiment. A reflection type setup was used. A dichroic mirror separated the laser light and the raman light from the  $D_2$ . The raman light was transported to the spectrometer with a glass fibre.

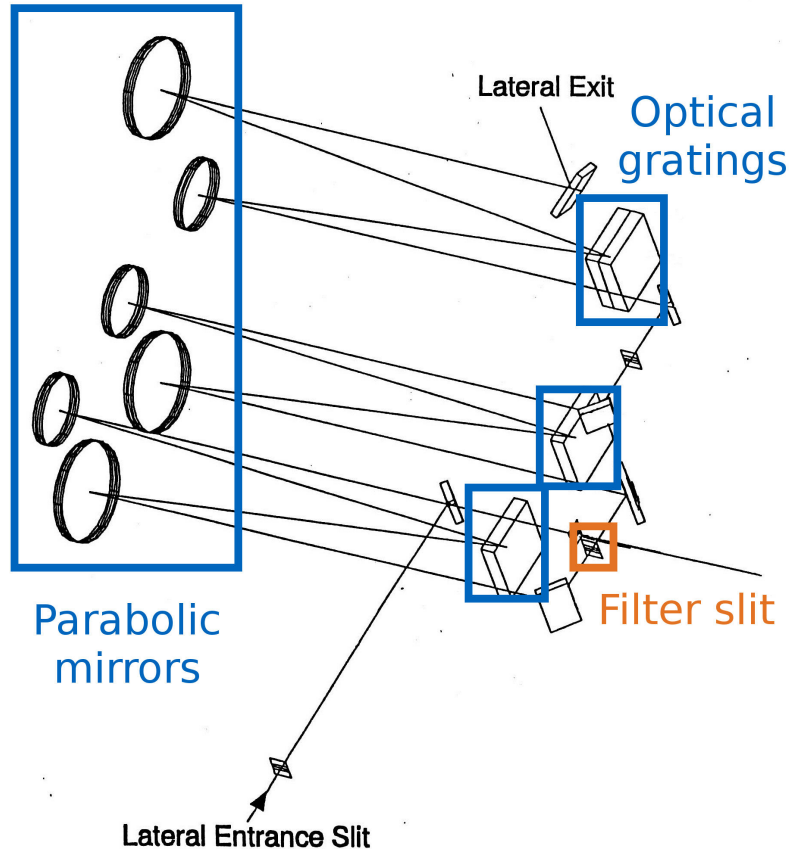


Figure 4.3.: Graphic taken from [Job94]. Scheme of the Raman spectrometer. The light passes a total of three optical gratings. The first two gratings, together with a  $500\ \mu\text{m}$  slit, comprise the filter (subtractive mode) stage of the spectrometer. The actual splitting of the different colors is done by the third grating.

The spectrometer itself was of the T64000 type of Jobin Yvon / Horiba GmbH. It had three diffractive gratings with a grating size of  $1800\ \text{mm}^{-1}$ . It was operated in subtractive mode meaning that the first two gratings filtered out undesired wavelengths. In detail, after passing the first grating the light was guided through a  $500\ \mu\text{m}$  slit. At this position, the slit was more narrow than the diffracted and collimated light beam. Thus, undesired wavelengths were filtered out. The width of this optical window in terms of wavelength is  $\sim 30\ \text{nm}$ . The second grating then reversed the effect of the first grating. The light, which passed the filter stage, was then again a collimated, pseudo-white (without the filtered colours) beam. The third grating then did the actual splitting of the different colour contributions. Figure 4.3 depicts a scheme of the above mentioned light path through the spectrometer. Two stepping motors drove the two different grating systems. The first system changed the filter window, meaning which part of the spectrum was guided to the third grating. The last grating decided which part of the spectrum is centred onto the camera.

The light signal was detected via a CCD (charge coupled device) camera (SBIG ST-2000XM). The entrance slit of the spectrometer was adjusted in such a way that only 70 rows of the CCD chip are illuminated. Since only these rows needed to be read out, noise is greatly reduced. A C++ program was written to combine all the functions of the spectrometer, i.e. varying the two grating stages as well as controlling and reading out the camera. The CCD chip was cooled down to  $-14^{\circ}\text{C}$  by an integrated Peltier element.

### 4.2.3. The Munich tandem accelerator

The experiment was conducted at the  $0^{\circ}$  (Hall 3) beam line of the Munich Tandem Accelerator laboratory (MLL). The accelerator can deliver many kinds of isotopes up to energies of 25 MeV for single charged ions.

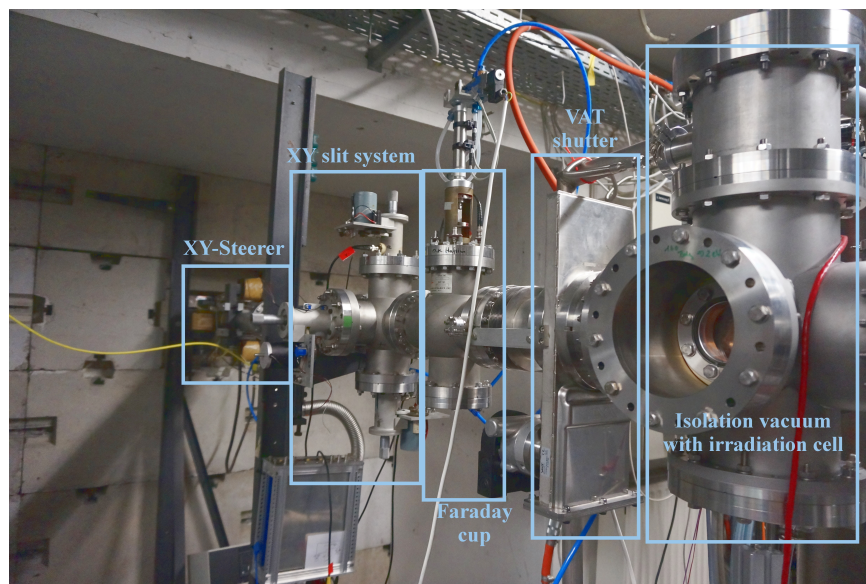


Figure 4.4.:  $0^{\circ}$  beam line of the Munich Tandem Accelerator (MLL) in Hall 3. From left to right one can see the beam steerers, a beam slit system, the Faraday cup and a vacuum gate.

During this work a 20.5 MeV proton beam was used to irradiate the target. Before the beam reached the experiment it went through several stages of quadrupole magnets guiding the beam along the tube. The last quadrupole was set to focus the beam into the target cell. A view of the beam line in Hall 3 of the MLL is shown in figure 4.4. On the left, the steerers can be seen, which were small electromagnets used to divert the beam along the  $x$  and  $y$  axis. Next, there was a beam slit system, with which it is possible to center the beam on the target with the help of the steerers. The beam current could be monitored with a Faraday cup, which could be driven into the beam when necessary. A vacuum shutter separated the beam line vacuum from the cryo-isolation vacuum of the irradiation cell when the beam was off.

### 4.3. Equipment test and calibration

#### 4.3.1. Irradiation cell

The freezing of gases in the irradiation cell was studied extensively. The lowest temperature achieved with the setup was  $(7.10 \pm 0.05)$  K. Although the cold head, used in these experiments, could in principle deliver colder temperatures, the fact that there were two holes in the cryo-shield around the cell resulted in a higher end temperature. The holes were necessary in order to let the laser light and protons enter the cell. The total power through heat radiation, which heats the cell through the holes, is 250 mW. The cryo-shield, mounted on the first stage of the cold head, could be cooled down to 50K. This means a heat load on the cell of 5 mW.

Deuterium has a triple point temperature of 18.6 K [Sou86]. At temperatures below 30 K the cell temperature could be controlled with an accuracy of less than 5 mK. Since the heater for the cell was mounted in the top part, the upper temperature sensor always saw a higher temperature than the lower sensor. At the triple point of  $D_2$  the difference between the two sensors was  $\sim 1.5$  K. At the lowest temperatures the difference was 0.4 K. Temperatures given from here on will mean the lower (colder) sensor. The  $D_2$  was first liquefied into the cell. The pressures in the experiment varied between 1.5 and 1.7 bar. The  $D_2$  started to liquefy at 22 – 24 K for the lower sensor or 24 – 26 K for the upper sensor.

For the solidification the  $D_2$  was first cooled to 18.7 K and afterwards the temperature was lowered with  $< 0.2$  K/h down to 16.5 K, where both temperature sensors showed less than 18.6 K. Further cooling of the solid was done with 1 K/h. A



Figure 4.5.: Deuterium frozen in the irradiation cell. The crystal is transparent and can hardly be seen. The diameter of the inner cell volume is 12 mm.

resulting crystal can be seen in figure 4.5. In first tests hydrogen was also used in the cell. The principal techniques stayed the same as described before, yet the freezing temperature for hydrogen is 14.0 K.

### 4.3.2. Raman spectrometer

A description of the theory of Raman spectroscopy on hydrogen cryo-solids can be found in Appendix A. Tests on the Raman spectrometer itself were done in several stages. Possible sources of backgrounds could thus be found before the irradiation experiment was conducted. First a mercury lamp together with several other gas lamps was used to shine light directly into the entrance slit of the spectrometer. It was found that the filter stage (gratings one and two) of the spectrometer has a transmittance window of  $\sim 30$  nm of wavelengths, which can pass through simultaneously without adjusting the positioning of the filter stage. The CCD camera could observe  $\sim 13$  nm of this window. It was decided to use a window where the first 4 Raman peaks of deuterium can be observed at the same time. A relationship between the pixel column of the CCD and the corresponding inverse wave number was also found [Hei15].

#### Tests with silicon

A first test with the laser beam was done with a silicon sample. Silicon has its main Raman line at  $(520.2 \pm 0.5)$   $\text{cm}^{-1}$  [Par67]. This concurs with the  $J=2 \rightarrow 4$

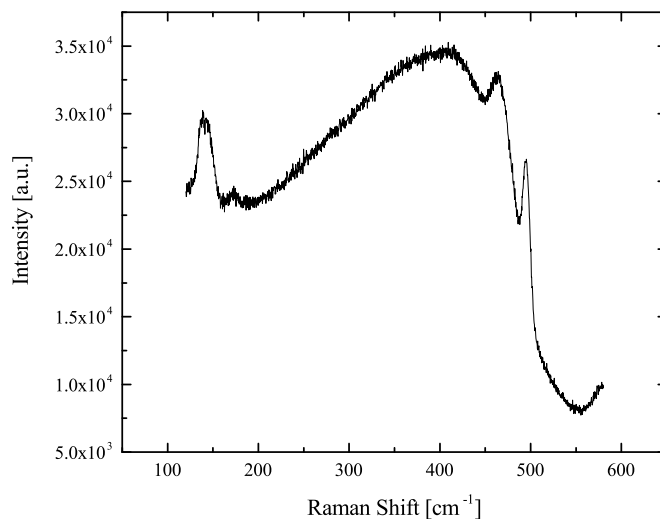


Figure 4.6.: Measured Raman spectrum of silicon. The silicon peak can be observed around  $500 \text{ cm}^{-1}$ . The other parts of the spectrum consist mainly of background from Raman light coming from the glass fibre. The exposure time was 1800 s.

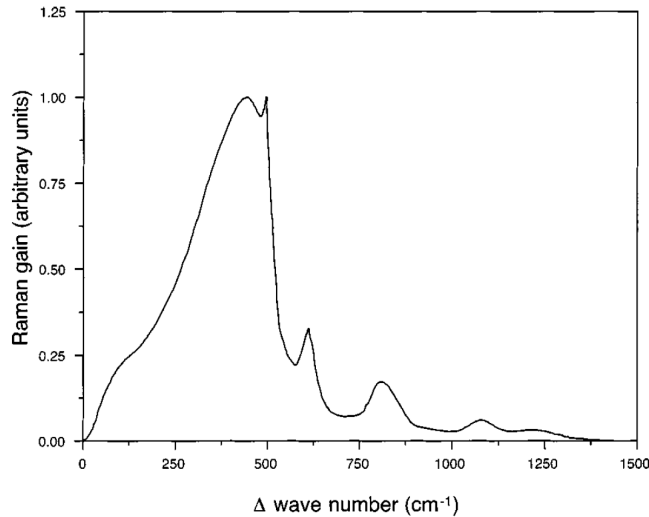


Figure 4.7.: Raman spectrum of a silica-core glass fibre. Graph taken from [Hol02]. Data from [Sto89].

transition of  $D_2$ . Thus, the same measurement window as for  $D_2$  could be used for silicon. Figure 4.6 shows a typical Raman measurement of silicon. The silicon Raman line can be distinguished from the background, which covers most of the spectrum. However, the silicon peak does appear at  $495\text{ cm}^{-1}$ . This is due to a preliminary calibration in these first tests. The background is mainly produced in the glass fibre as it resembles quite accurately the Raman spectrum of  $\text{SiO}_2$  as can be seen in fig. 4.7. This fibre background did not pose a significant problem in the later measurements, since it was greatly reduced due to the slightly different optics geometry used. However, the first peaks visible on the very left in the spectrum still appeared in the spectrum later on. While they did not disturb the measurements on liquids and solids, they did increase the uncertainty on gas measurements as they partly shadowed the  $J=0 \rightarrow 2$  transition of  $D_2$ .

### Calibration of the spectrometer

The experiment will focus on the first two transitions of solid deuterium. Since they both appear in the same measurement window of the spectrometer ( $100 - 600\text{ cm}^{-1}$ ), it is sufficient to calibrate the signal within this one window. For other windows, e.g. the vibrational lines of deuterium which appear around  $3000\text{ cm}^{-1}$ , the uncertainty of the calibration is bigger.

In order to calibrate the pixels of the CCD to a corresponding Raman shift a gas phase spectrum of deuterium was taken. For the four observable peaks their position on the CCD was related to their respective Raman shift. Thus, a calibration function was found. Figure 4.8 shows the measurements used for the calibration. The deuterium peaks are clearly identifiable up to the first five peaks.



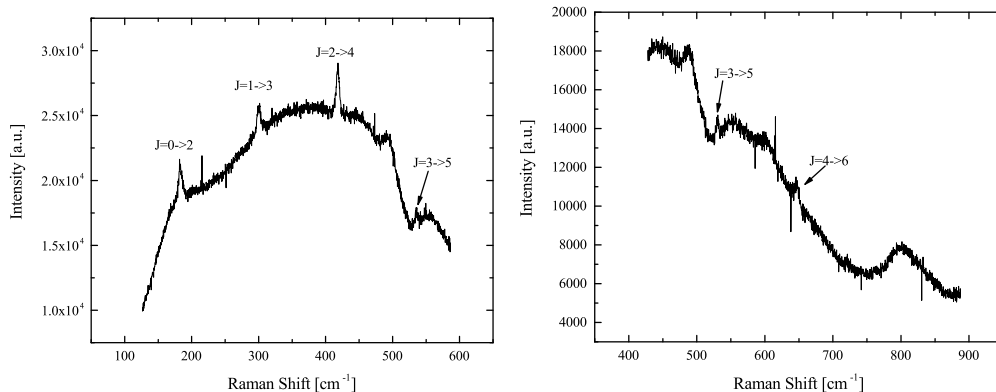


Figure 4.8.: Measured Raman spectra of gaseous deuterium. The first five Raman peaks are visible. The background comes from Raman scattering in the glass fibre.

For other measurement windows it was found, that for every turn of the measurement window index on the spectrometer, the observation window shifted by 1.5 nm. Thus, a total calibration function for every measurement window was found. It was also observed, that the central wavelength of the laser shifts by up to  $10 \text{ cm}^{-1}$ . The data shown here were not corrected for this fact, since only the relative intensities of the different peaks are important.

### Tests on hydrogen and deuterium

Next, Raman tests on cryogenic hydrogen and deuterium were conducted to see if there are any deviations from the literature values for natural conversions between the para and ortho species due to the materials or the geometry used in the experiment. Figure 4.9 shows a typical Raman spectrum of liquid  $\text{H}_2$  at 15 K. Only the transitions  $J = 0 \rightarrow 2$  and  $J = 1 \rightarrow 3$  are visible. All other rotational levels are unoccupied. The illumination time on the CCD sensor was 300 s. No background is visible, which facilitates the analysis as only the area under the peaks needs to be counted. Hydrogen has a ratio of even  $J$  to odd  $J$  of 0.25 at room temperature. The conversion rate, however, is much faster than for  $\text{D}_2$  [Sou86]. In this case the  $\text{H}_2$  had been frozen solid for a period of 15 min, before it was reliquified to a temperature of 15 K. At that time the  $J = 0$  content was calibrated to be at 0.25. Details on the analysis of the spectra and the Raman cross-sections for the different rotational levels can be found in Appendix B.

The sample was held at 15 K for three days. Figure 4.10 shows the  $J=0$  content in the sample over time. It increased monotonously towards its equilibrium value of 1. The data have been fitted with an exponential fit.

$$c_o(t) = 1 + (c_o(0) - 1) e^{-\frac{t}{\tau}} \quad (4.1)$$

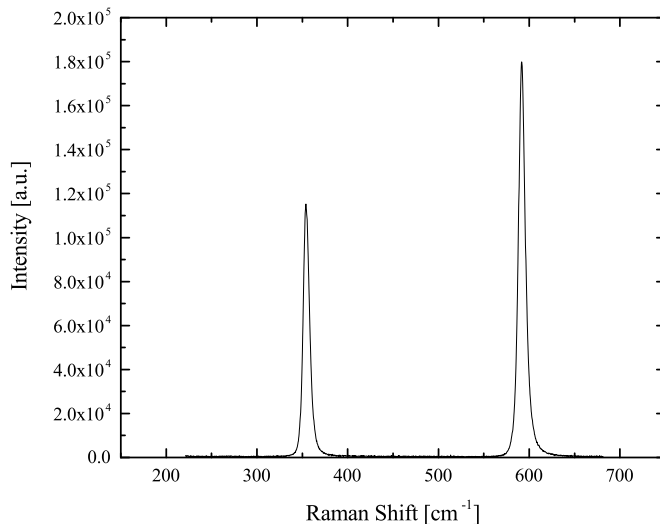


Figure 4.9.: Raman spectrum of liquid hydrogen at 15 K. The exposure time was 300 s. The corrected  $J = 0$  content is 0.250.

The conversion time  $\tau$  was determined to be  $(63.7 \pm 2.3)$  h, which is faster than the value given in [Sou86]. While it is also mentioned in [Sou86] that the conversion rate increases with pressure, the pressure in this experiment (1.5 bar) was by far insufficient to increase the conversion rate by this much [Dic65]. The reason for the increased conversion rate might be due to the cell geometry or the vibrations from the cold head. However, an exact reason could not be determined.

The peaks in fig. 4.9 have enough statistics so that the statistical uncertainty becomes negligible. The actual data treatment is far more crucial concerning uncertainties. At a first glance the data appear to be free of background, yet it

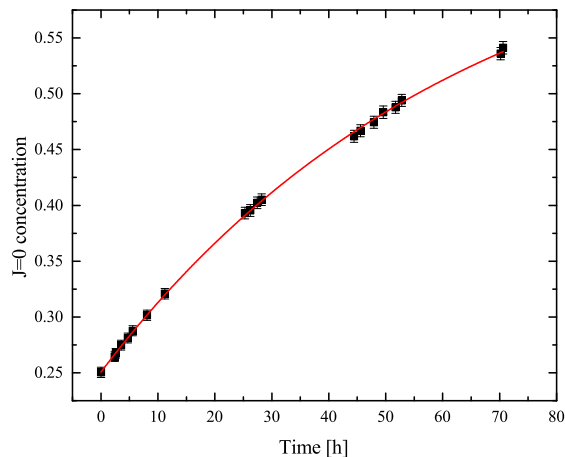


Figure 4.10.:  $J = 0$  content in the liquid hydrogen sample over time. The  $J = 0$  content increased monotonously. The fitted conversion time constant was  $(63.7 \pm 2.3)$  h

is known that there is a small background at  $200\text{ cm}^{-1}$  and there is an overall background in images with longer exposure times. This background has to be subtracted first. As the laser output is not perfectly constant and highly sensitive to variations in air temperature, it was not possible to subtract a "standard" background. Also, in the  $\text{D}_2$  measurements there is a small peak from HD contamination. The background was interpolated by manually setting data points for each spectrum. The peaks were then fitted with a Voigt function, since it describes the peaks most accurately. This treatment results in an uncertainty for the  $J=0$  content in the order of  $10^{-3}$ .

The Voigt function is a convolution of a Gauss and a Lorentz curve. Thus, it includes both broadening mechanisms, which is useful, since in this experiment, several broadening mechanisms along the path of the Raman light are at work. Not only are the deuterium peaks broadened already within the deuterium, but also in the optics system and the spectrometer, especially the entrance slit. Details on the Voigt fitting function can be found in Appendix B.

The width of the peaks was dependent of the state of the sample. For gases the FWHM was around  $5\text{ cm}^{-1}$ , for liquids  $10\text{ cm}^{-1}$  and  $13\text{ cm}^{-1}$  for the solids. The broadening of the peaks can be explained in the following way. In a perfect  $J=0$  or  $J=1$  crystal the peak width would be comparable to the gas phase measurements. The transition  $J=0 \rightarrow 2$  forms a roton band which splits into three distinguishable sub-levels in the solid [VK60]. Any para-deuterium molecules in the crystal lattice act as a impurity, which the  $J=2$  roton cannot excite. The roton band is therefore broadened depending on the  $J=1$  content in the crystal [Bha62]. Due to this broadening the splitting of the roton band into three states could not be observed. Further analysis on the peak width can be found in chapter 5.8.

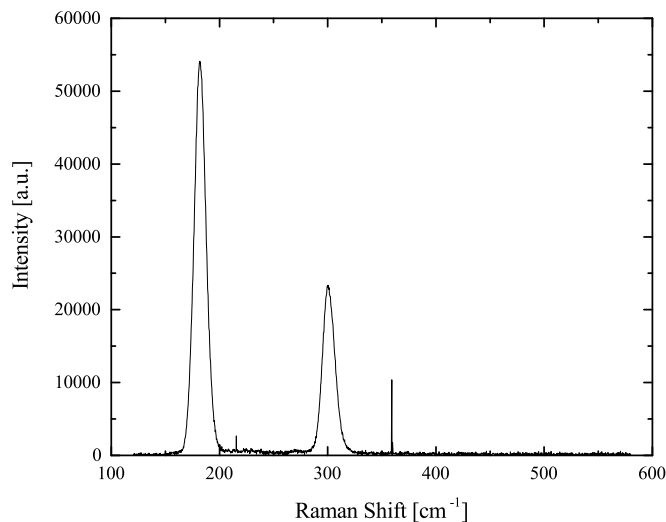


Figure 4.11.: Raman spectrum of deuterium at 7.1 K. The transitions  $J=0 \rightarrow 2$  and  $J=1 \rightarrow 3$  can be clearly identified. The narrow line to the right of the deuterium peaks stems cosmic rays hitting the CCD.

Figure 4.11 shows a typical Raman spectrum of deuterium. The two transitions  $J = 0 \rightarrow 2$  and  $J = 1 \rightarrow 3$  are clearly visible. The small, narrow line on the right side comes from cosmic rays which can hit the CCD pixels. The data treatment is the same as before.

The effect of the freeze out on the ortho content of the sample has also been studied. This can be seen in figure 4.12. The  $D_2$  was first cooled down to 30 K. Subsequently the deuterium was liquefied and held at different temperatures. The uncertainty of the values for the liquid decrease in comparison to the gas because the statistics is far greater. The freeze out process then seems to enhance the ortho fraction slightly by 0.01. However, the fit does have problems accurately fitting the liquid data, which is why the uncertainty is larger. Due to a higher background in the gas measurement, the uncertainty of the data point at 30 K is also increased.

The deuterium was kept at 7.1 K for several days to observe the natural increase in the ortho fraction. Since the deuterium magnetic moment is only a third of the hydrogen magnetic moment, the self-conversion is greatly reduced (cf. chapter 3.3.2). The self-conversion over time can be seen in figure 4.13.

The conversion time  $\tau$  was then determined using eq. 4.1 to be  $(1841 \pm 227)$  h with a starting ortho fraction  $c_0(0) = (0.685 \pm 0.002)$ . The rather large uncertainty stems from the fact, that the measurement time was only about 6% of the self-conversion time. Together with the uncertainty of each data point of  $(2 - 4) \cdot 10^{-3}$ , this results in the large relative uncertainty of 12.3%. The liter-

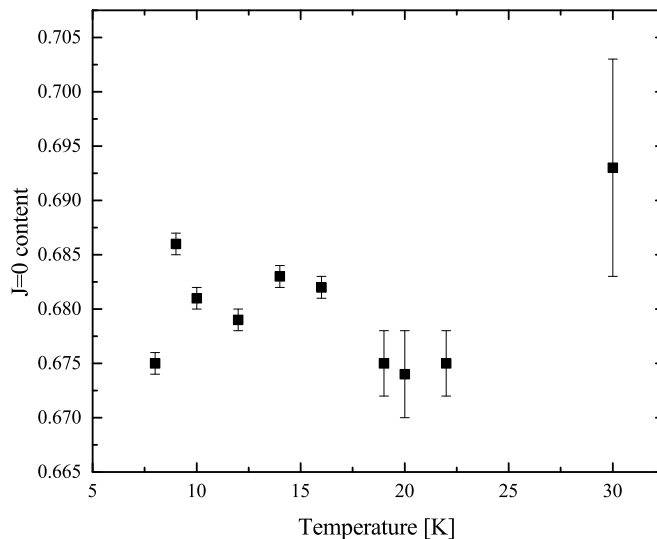


Figure 4.12.: Ortho content of deuterium during cooldown and freezing. The statistical uncertainties of the Raman peaks in the solid are significantly smaller, since the Voigt fit reproduces the data better. Molecular motion in the liquid changes the shape of the peak, so that the fitting procedure is less accurate.

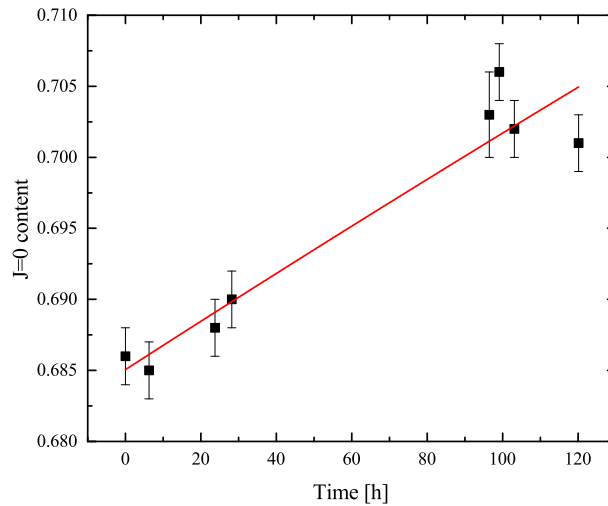


Figure 4.13.: Ortho fraction of the  $D_2$  sample over time. The red line represents an exponential fit.

ature value for the self-conversion time is 1900 h [Mil75] or  $6 \cdot 10^{-4} \text{ h}^{-1}$  [Sil80]. Extrapolating the self-conversion for the duration of a beam time (10 days), the ortho fraction in the sample will increase by  $(0.040 \pm 0.005)$ . Any enhancement due to irradiation would have to be significantly bigger than this.

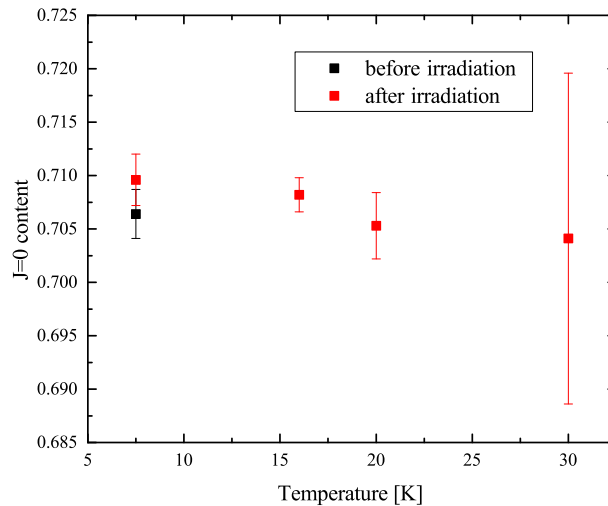


Figure 4.14.: Ortho fraction in the deuterium sample at different temperatures. The black point is the ortho fraction before the 1 h irradiation, while the other data points are after irradiation. A small enhancement of the ortho fraction is visible after irradiation. After the crystal is liquefied again and the irradiated portion of the crystal is diluted with the non-irradiated liquid, the ortho fraction drops to its original value.

### 4.3.3. Tandem accelerator

During a small test run of roughly 1 h duration the setup could be tested. At the same time the parameters of the accelerator, which were later used in the actual beam time, were found out. Fig. 4.14 shows the ortho concentration in the sample at different temperatures. The black point is the starting ortho fraction before the irradiation. The beam current incident on the sample was set to 2.6 nA. The red points in fig. 4.14 are after irradiation. One can see a small enhancement in the ortho fraction, which remains even after warming up the crystal to 16 K. Once the crystal is liquefied, the ortho fraction drops back to its original value, since the liquid is now a dilution between irradiated and non-irradiated D<sub>2</sub>.

# Chapter 5.

## Beam time and results

---

The setup, as it was described above, was irradiated at the Tandem Accelerator Laboratory in Munich. Protons were used as irradiation particle. While protons of course lose energy differently than gammas in a solid, both particles eventually lead to an ionization and excitation of the  $D_2$ , which then can be dissociated. In the later analysis, this dissociation rate ( $k$ ) was fitted along with the ortho-para conversion parameter ( $\beta$ ), so that the actual irradiation particle can be neglected. Afterwards, by knowing the value for  $k$  at the FRM II, extrapolations could be made for the case of the new UCN source.

### 5.1. Beam parameters

The proton current was varied between 2.0 – 3.5 nA for the first beam time and between 2.5 – 6.0 nA for the second. The energy was set to 20.5 MeV and varied only on the  $10^{-3}$  level. With the XY-slit system in front of the experiment the beam dimensions could be estimated. For the first experimental run a beam dimension of 6 mm  $\times$  6 mm was estimated. At the end of the first run the beam size was increased to 8 mm  $\times$  8 mm, as it was found, that this enhances the ortho/para transition seen in the system. In the second beam time, a broader beam of 8 – 10 mm  $\times$  8 – 10 mm was used from the beginning.

### 5.2. Temperature and beam control

#### 5.2.1. Cell temperature

The beam was set up in such a way, that there was a maximum temperature increase of the cell. It is worth noting, that all temperatures reported here are the temperatures of the sensors directly next to the deuterium but mounted within the irradiation cell. Thus the exact temperature of the inner part of the deuterium

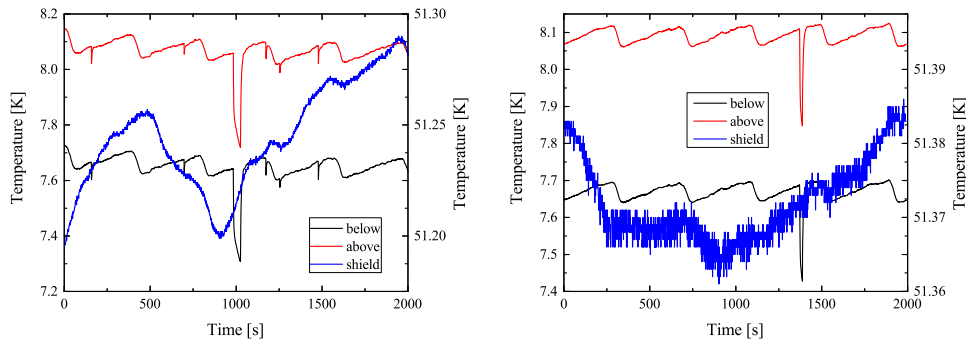


Figure 5.1.: Comparison of two temperature trends during irradiation. In both cases the regular temperature variation due to a change in irradiation strength can be observed. The upper sensor (red line) sees a temperature, which is 0.4 K higher than the lower sensor temperature (black line). The blue line represents the temperature of the cryo-shield surrounding the cell. The right  $y$ -axis is the corresponding scale. In the left figure the temperature variation also slightly shows in the data of the shield. It does not on the right side indicating that the beam completely hits the cell.

remains unknown. The temperature increase of the cell was directly proportional to the beam current. The increase was between 0.3 – 0.4 K. Over the two beam times the temperature (without beam) of the cold head increased slightly. This did not pose a problem to the measurement itself, but the temperatures in general increased by 0.4 K during the experiments. Unfortunately, no reason for this increase could be found, yet it is possible that rest gas was being continuously frozen on the outside of the irradiation cell and thus increased the thermal conductivity onto the cell, which in turn limited the achievable lowest temperature.

Figure 5.1 shows two temperature trends on different days of irradiation. Each sample contains  $\approx 30$  min of data. The upper temperature sensor of the cell (red) is always  $\approx 0.4$  K warmer than the lower sensor (black). This temperature gradient along the cell (and thus, along the deuterium) was constant throughout the beam times. It is possible to identify a sawtooth profile in the temperature sensors of the cell (black and red). This is due to an irregular beam current coming from the accelerator source. The blue line represents the temperature of the cryo-shield surrounding the cell. This temperature usually varied with the temperature conditions in the experimental hall. On the left picture of fig. 5.1 one can also identify some of the sawtooth profile features indicating that part of the beam hit the shielding. This is not the case for the right side picture, indicating that the full beam hit the cell. The temperature drops in both pictures (around 1000 s and 1400 s) the times where the beam was interrupted to measure the beam current.

In a second beam time the experiment was repeated at 10 K. In this experimental run, the protons were able to penetrate the whole length of the irradiation cell, since the entrance window was thinner than before. However, the energy remained at 20.5 MeV. A PID control loop kept the temperature of the cell bottom at



10 K, while the upper part was at 10.6 K. The temperature remained stable within 10 mK, as the beam was either on or off. Switching between both states had the crystal warm up or cool down by approximately 50 mK. This however, did not have any negative effects on the measurement, as the crystal quality remained the same.

For all calculations done here, where the temperature of the deuterium is needed, the average between the two temperature sensors was taken, since it most likely represents a temperature in the middle plane of the cell.

### 5.2.2. Beam stability

Apart from the sawtooth pattern mentioned above, several parameters of the accelerator changed over the course of several hours which made corrections to the beam necessary.

Downstream of the Tandem accelerator a  $90^\circ$  bending magnet is placed, which is used by all other experiments at the facility. This experiment did not use the magnet but the beam had to go straight through. Since it always used, it is fair to assume, that it was magnetized into saturation and some rest field remained after turning off the magnet. Thus the beam had to be shot into the magnet slightly out of the beam axis in order to have the rest magnetisation of the magnet bend the beam back into the straight forward direction. Over the course of the beam time this rest magnetisation varied slightly which was accounted for by an auxiliary coil in the magnet.

Space charges within the Tandem accelerator tank itself led the beam to divert from its original position over time. This resulted in a non-constant irradiation profile. This might not have been recognized during irradiation. Ultimately those space charges led to a spark roughly once per day and an intermediate shutdown of the accelerator was necessary. Afterwards the beam had to be adjusted, thus, for the analysis one has to pick out times where the machine ran constantly for several hours.

### 5.2.3. Laser and optics system

The laser was set to a LED current of 340 mA and a temperature of  $24.2^\circ\text{C}$ . This resulted in a light power output of 19 mW. The light output of the laser remained stable within 3%. The Raman spectrometer entrance slit was set to a width of  $50\ \mu\text{m}$ . The CCD camera was set to a temperature of  $-14^\circ\text{C}$ .

Unfortunately the optics system had to be re-adjusted twice during the first beam time. After that beam time it was found that there was a difference in the trans-

mission profile of the two relevant Raman lines before and after the adjustments. Each set of data was calibrated to a para-ortho ratio of a freshly frozen deuterium crystal with its natural ortho-para-ratio. For the one day between the two adjustments no calibration is available. However, using the second calibration for this intermediate time yields values which are very reasonable. Those data are marked separately in plots. The calibration values used here have to be used in addition to the corrections made for the difference in the Raman cross-section for the different deuterium rotational transitions. The correction factor  $\kappa$  is effectively the value by which the  $J=0 \rightarrow 2$  line is reduced, hence the effective intensity ratio  $R$  is calculated

$$R = \kappa^{-1} \frac{S(0 \rightarrow 2)}{S(1 \rightarrow 3)}, \quad (5.1)$$

with  $S(i \rightarrow f)$  being the counts in the different Raman peaks. The actual ortho fraction  $c_o$  was calculated in the following way.

$$c_o = \frac{R}{f + R} \quad (5.2)$$

In this case,  $f = 1.699$  is a dimensionless quantity describing the ratio of the partial density functions for the relevant  $J = 0 \rightarrow 2$  and  $J = 1 \rightarrow 3$  excitations and the differences in the photons coupling to the excitations. Details can be found in Appendix B.

The values for  $\kappa$  during the beam times were

$$\begin{aligned} \kappa_1 &= 0.636 \pm 0.002 \\ \kappa_2 &= 0.768 \pm 0.003 \\ \kappa_3 &= 0.749 \pm 0.002. \end{aligned}$$

This calibration procedure is also described in Appendix B. The correction factors  $\kappa$  and their uncertainties were calculated as weighted means from 5 to 10 measurements on a freshly frozen crystal with a known (natural) ortho/para ratio. Incidentally, the value for  $\kappa_2$  can be explained assuming that the laser emitted light at 531 nm, which is still within the specifications of the laser. The transmission for the  $J = 0 \rightarrow 2$  line is then 0.77 according to the manufacturer [Sem16]. This assumption is also supported by the high reflectivity of the laser line of  $\sim 0.995$ . For 532 nm the manufacturer states a transmission of 0.03, for 531 nm it is 0.01. In contrast to  $\kappa_2$  it is unclear why  $\kappa_1$  is even smaller. The only change to the optics system was the exact positioning of the 3 last lenses (see fig. 4.2), while the distances between those three lenses remained the same. It seems, that for the first few measurement days, where  $\kappa_1$  applies, the transmission of the dichroic mirror was worse for the  $J = 0 \rightarrow 2$  line. This might be due to a slightly different angle with which the light hit the mirror, which was then fixed after the re-adjustment.

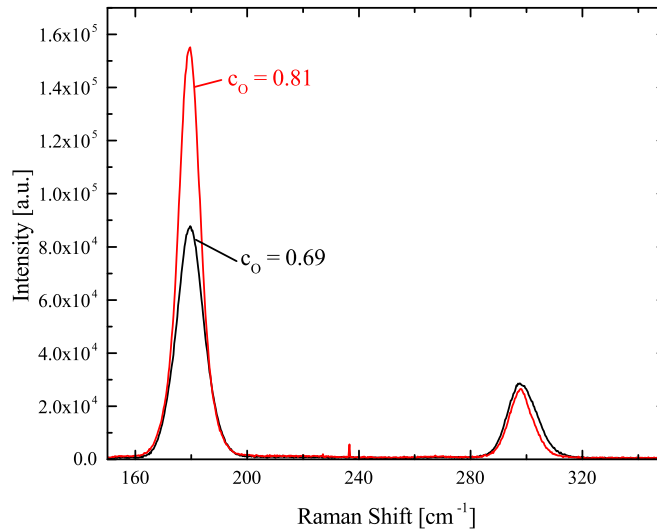


Figure 5.2.: Comparison of Raman intensities at two different ortho concentrations  $c_o$  after freeze out.

$\kappa_3$  was applied during the second beam time where the optics system was completely re-adjusted before the beginning of the run. The optics system was left untouched for the second beam time, so that  $\kappa_3$  was used for all the data of that run. The values for  $\kappa_2$  and  $\kappa_3$  are very similar, however, they do not coincide within the uncertainties. Obviously, the calibration factor  $\kappa$  has to be determined any time the optics system is altered..

#### 5.2.4. Crystal quality

A major issue for the Raman spectroscopy on solid deuterium is the crystal quality. While the freezing procedures were all tested and evaluated before the actual experiment, there was no way of visually inspecting the crystal during the beam time. However, the laser signal provided a few hints. First, as discussed in chapter 3, the thermal conductivity of solid deuterium improves drastically when going from a natural ortho composition to a highly enriched ortho crystal. Under the experimental conditions and with the measured ortho concentrations, the thermal conductivity can be expected to double from 2 to 4 W/m · K. This meant, that after refreezing the crystal the signal intensity was often greatly improved and even more so for the later beam days with an increased ortho content, as can be seen in fig. 5.2. One can also observe a difference in the width of the peaks, which will be discussed later in this chapter.

The crystal quality could also be assessed through the data from the laser power meter. While the most part of the light hitting the power meter came directly from the laser itself, part of the light returning from the irradiation cell could also hit the power meter. Thus, the data were sensitive to the current state of the

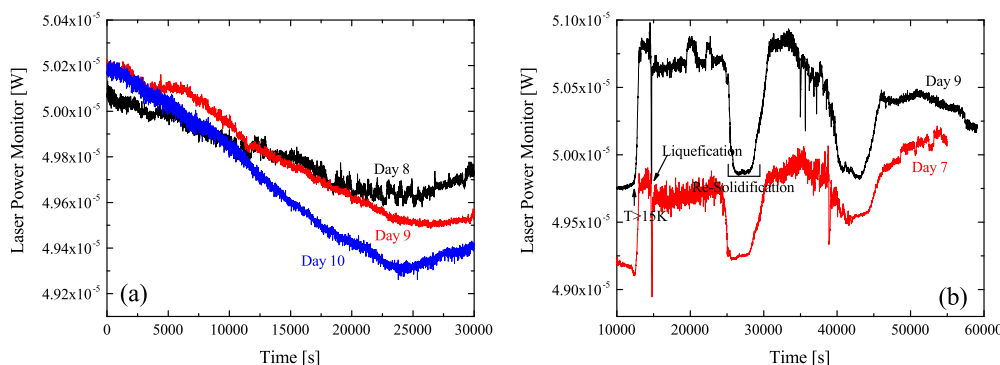


Figure 5.3.: (a) Laser power monitor data during data taking on the last three beam days. The curves all share a similar trend. The power decreases for the most part of the day until it starts increasing again in the evening. (b) Laser power monitor data during two nights, during which the crystal was melted and re-frozen. The curves share the same features across the whole time.

crystal, especially when the crystal turned opaque, the power meter would show a decrease. Fig. 5.3 (a) shows a plot of the laser power for three different beam days (days 8-10) of the first experimental run. The time axis shows the seconds after a new log-file of the laser power was started. One can see that the lines share a very similar behaviour. After the beam is turned on the laser power decreases, indicating an increase in opacity. This might be due to irradiation damage leading to cracks in the crystal. On day 9 the beam was turned on a few hours later than the laser log, and one can see the decreasing starting later that day. On all three days the laser power increases again after 6 – 7 hours. Since on all three days the ortho content increased, and thus the thermal conductivity, one can suspect that the crystal begins to anneal the irradiation damage ultimately leading to a higher signal at the power meter.

Figure 5.3 (b) shows data from the same power meter during two nights where the crystal was first liquefied and then re-frozen. First one can observe a sharp rise, which sets in, once the crystal temperature is above 15 K. It was observed previously that the crystal returns to a transparent state above this temperature regardless of its previous state. On both days there were a few hundred seconds of measurement time before the crystal was liquefied, which is expressed by a sharp drop and an immediate restoring of the laser power. This is due to the crystal melting non-uniformly in a way that not all parts of the crystal melt at the same time and thus the laser beam might be blocked by some parts still being frozen. The first of the two larger power drops can be attributed to the actual freeze out process, where again during crystal formation not all of the cell is truly transparent. The second drop could come from a bubble forming at the gas inlet, which was observed in pre-tests before the experiment. This bubble slowly descends through the cell as the temperature decreases and after it reaches the bottom of the cell it slowly becomes transparent.

### 5.3. Measurement of the $J=0$ content

#### 5.3.1. Data at 7.8 K

Measurements on the beam current were done every half hour by pneumatically inserting a Faraday cup into the beam line. After each current measurement, a Raman measurement was started. The exposure time for every data point was 600 s. After each exposure a second, dark frame was taken. The dark frame was then subtracted from the exposed frame to yield the actual Raman spectrum. This greatly reduced noise from hot pixels on the CCD. The spectra were handled in the same way as described in chapter 4.3.2.

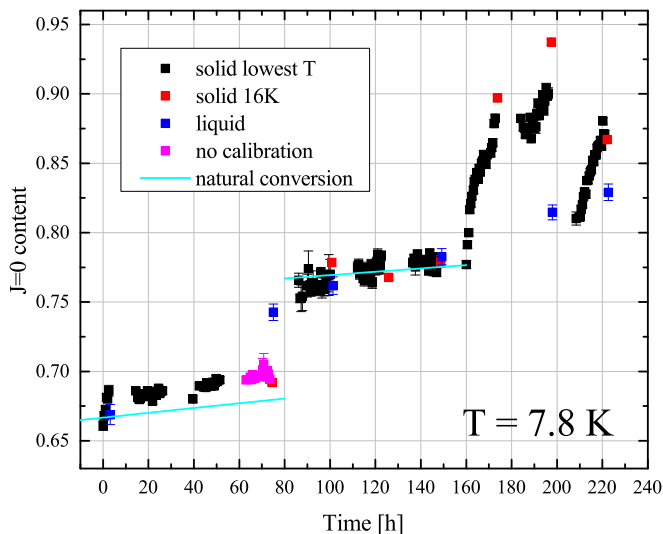


Figure 5.4.:  $J=0$  content in the deuterium during the first beam time. The  $x$  axis are the hours since the freezing of the  $D_2$ . Black data points represent measurements at the lowest achievable temperature. Red data points represent measurements at 16 K at the lower temperature sensor. Blue data points are measurements in the liquid phase at 19 K. Purple points are data where the calibration is unconfirmed. The light blue line shows the natural ortho-content in a non-irradiated system with a conversion time of 1900 h [Sou86]. Error bars indicate fitting uncertainties from the Voigt function fit.

Figure 5.4 shows the ortho content versus time. The time axis shows the hours after the first freezing of the  $D_2$ . Thus, the pauses in between the data points represent the night times where no measurements were done. The black points are data taken at the lowest achievable temperature with the beam on. The red points were taken at a temperature of 16 K for the lower sensor, while the blue points are at 19 K in the liquid phase. Purple points are the data between the two re-adjustments of the optics positioning. Those data were corrected using  $\kappa_2$ . While they seem to agree with the rest of the data, the calibration cannot be confirmed. The light blue curve shows the natural conversion of the deuterium with a conversion time of 1900 h [Sou86].

Several times during the beam time the crystal was either warmed up to 16 K over the course of half an hour, or liquefied to mix the irradiated parts of the  $D_2$  with the non-irradiated parts. Refreezing was then done as described above very slowly when near the freezing temperature or with a ramp of 1 K/h at lower temperatures.

The error bars in fig. 5.4 are statistical uncertainties from the fits used to describe the Raman spectrum. Details about the analysis can be found in appendix B.

Several stages of the experiment can be identified in fig. 5.4. In the first few hours there was a sharp rise of the  $J = 0$  content. In the following days hardly any conversion could be observed. Any change in that time can be attributed to natural conversion. Nevertheless, as can be seen from the data in the liquid, conversion must have been occurring in some part of the  $D_2$ . Thus, it is fair to assume, that the beam did not irradiate the volume, which the laser beam was analysing. For the last three beam days the beam was widened to  $8 \text{ mm} \times 8 \text{ mm}$ . As can be clearly seen, the ortho content in the sample subsequently increased sharply. Thus, those three days will have the main focus of the following analysis. The average temperatures of the deuterium crystal for those three days are given in table 5.1.

It is noteworthy, that the beam was only widened by  $\sim 2 \text{ mm}$  in each direction for the last three beam day, but conversion must have occurred before, as can be seen from the data in the liquid. This shows, that the crystal defects and deuterium atoms do not move far within the crystal lattice, but rather remain localized.

Table 5.1.: Average temperatures of the deuterium crystal during irradiation on the three different beam days used for the analysis.

Day	Temperature [K]	Uncertainty [K]
8	7.74	0.07
9	7.79	0.06
10	7.88	0.05

### 5.3.2. Data at 10 K

The measurement procedure was the same as for the previously mentioned beam time. Data were taken every half hour and the Raman exposure times were 600 s. In this beam time a PID control mechanism kept the temperature of the irradiation cell at 10 K at the lower temperature sensor. Also, a four-sector-aperture was mounted directly in front of the irradiation cell, so that the beam could be accurately centred onto the entrance window.

Figure 5.5 shows the results of the second beam time. A general increase of the  $J = 0$  content can be clearly seen. Unfortunately, at several stages during the

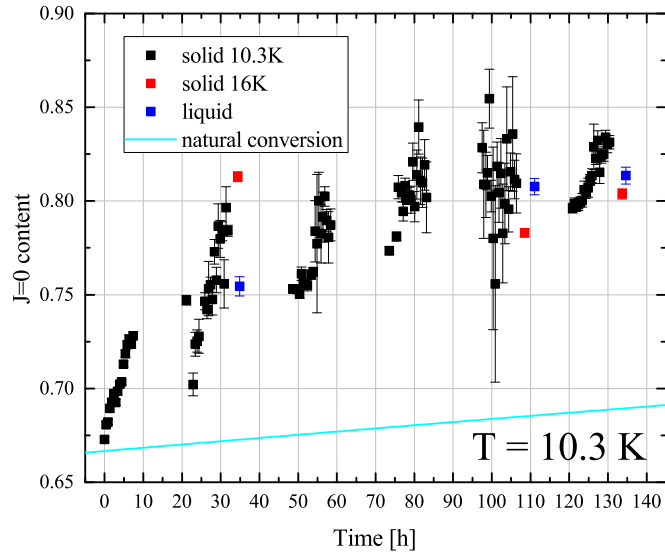


Figure 5.5.:  $J = 0$  content in the deuterium during the second beam time. The  $x$  axis are the hours since the freezing of the  $D_2$ . Black data points represent measurements at 10 K. Red data points represent measurements at 16 K at the lower temperature sensor. Blue data points are measurements in the liquid phase at 19 K. The light blue line shows the natural ortho-content in a non-irradiated system. Error bars indicate fitting uncertainties from the Voigt function fit.

experiment, the heating power supply, which kept the cell at its temperature, failed to regulate the heating voltage properly, which resulted in a sharp rise in the deuterium temperature. Subsequently the PID mechanism regulated the temperature back to its nominal value, but a large decrease in the Raman signal could be observed. Thus, it can be assumed that for those times the crystal quality is rather bad. Fig. 5.5 shows this especially for the beam days 3 - 5. The uncertainties from the Voigt function fit are greatly increased during those three days, while for the other beam days the uncertainties are comparable to the first beam time. Hence, the beam days 1, 2 and 6 were used for the analysis.

Since the temperature of the lower sensor was kept at 10 K by the PID, no drift in temperatures was observed. The upper sensor showed a temperature of 10.59 K. Hence, averaging those temperatures yields an average deuterium temperature of  $(10.30 \pm 0.05)$  K.

### 5.3.3. Uncertainties

There are several uncertainties, which contribute to the error bars and the final uncertainty for the fitted values.

- The statistical uncertainty of the fit of the individual spectra. Every peak in each spectrum is fitted with a Voigt function. The fit and the accompanying uncertainty is determined with Origin Pro 9.1.
- The statistical uncertainty of the correction factor  $\kappa$ . The correction factor has also been determined fitting several spectra with a known ortho/para ratio with Origin Pro 9.1. This uncertainty is included in all plots showing ortho contents. It has to be kept in mind, that all the uncertainties concerning the transport efficiency of the different Raman lines through the optical system to the spectrometer went into this uncertainty.
- A systematic error due to the uncertainty of the wavelength of the laser. This in turn might affect the correction factor, which arises from the difference in wavelength of the laser and the Raman lines. Since only the difference between the wavelengths is important, this error can be neglected compared to the statistical uncertainties.
- An uncertainty due to the subtraction of the background in the spectra. This uncertainty was assumed to be a fixed value 0.002 and was added linearly to all the previous uncertainties and is shown as well in all the plots. The value has been determined by repeatedly evaluating selected spectra in the same manner and observing the change in the calculated ortho fraction.
- The uncertainties of the fitted values have again be determined with Origin Pro 9.1. Since all previously mentioned uncertainties went into the fit, they already represent the final uncertainty. The relative uncertainty for each of the values is in the range of 50 %. While this seems to be a rather high uncertainty, one has to keep in mind, that in the fit function (see eq. 3.13)  $\kappa$  and  $\beta$  are summed together in almost all places of the function. This means, that the fitting algorithm has a hard time distinguishing between the two values. Thus the final uncertainty can be viewed as a value space in which it is possible to find a pair of values yielding a comparable  $\chi^2$  value.

## 5.4. Conversion parameters

Figure 5.6 shows a day-by-day comparison of the beam days of the two beam times, which were eventually chosen for analysis. On all of these days an increase in the ortho fraction of the D<sub>2</sub> between 0.03 and 0.1 was observed. The increase however, shows a different behaviour for the different days. In the left plot for the 8<sup>th</sup> irradiation day (black dots) the increase does not follow a single trend. After 2 h the slope becomes flatter. This is due to the beam slowly drifting out of the target area. This could be seen by an increase in the radiation in the accelerator hall indicating that the beam increasingly hit the walls of the Tandem accelerator. The result of this was a spark towards the end of the beam day. Other beam days



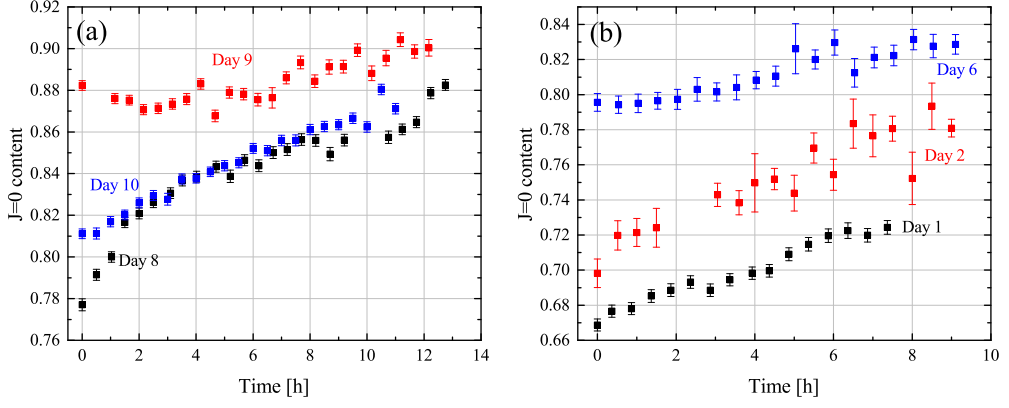


Figure 5.6.: Ortho fraction during the beam days used for the analysis. (a) shows the first beam time with temperatures of  $\sim 7.8$  K, (b) shows the second beam time with an average  $D_2$  temperature of 10.3 K. All data show clear signs for an increase in the ortho fraction of the sample. The data for the actual analysis were chosen in such a way, that stable conditions during the irradiation were insured.

show differences in the slope as well. On beam day 9 of the first beam time the ortho fraction did not increase for several hours. At first it dropped even by roughly one percent point. The reason for this might be cracking within the crystal due to the irradiation. This, in turn, might slightly shift the focal point of the laser to a position where the irradiation did not hit. Again, after re-adjusting the beam, an increase in the  $J=0$  content was observed.

For the actual analysis only those parts of the data, where stable conditions were encountered, were chosen. For the days, where the start of the increase does not coincide with the start of the beam (i.e. corrections to the beam where necessary) the data point, which resulted in the lowest  $\chi^2$  value, was chosen as  $t = 0$  point for the fit. A combined fit was done with Origin Pro 9.1. The values for the dissociation rate  $k$  and the starting ortho fraction  $c_0$  were fitted individually for every curve. The value for the conversion rate parameter  $\beta$  was set to be the same for all the fitted curves of one beam time. This assumption is well met for the second beam time, since the temperature was kept stable. For the first beam time, the small deviations in temperature were negligible in comparison to the fitting uncertainty. The recombination rate factor  $\alpha$  was again set individually as a fixed parameter for each curve according to the values of Iskovskikh et al. [Isk86]. Even though  $\alpha$  could have been fitted as well, taking a closer look at the fitting function eq. 3.13, one can see that  $\alpha$  and  $k$  are not really independent in the function so that at least one of them has to be fixed.  $\beta$  also has a slight co-dependence on  $k$ , but since  $k$  turns up in one of the fit function terms alone, it can be fitted separately.

The fitted curves are shown in fig. 5.7. First of all, one can notice, that the fits describe the curves rather well. This is also indicated by the  $\chi^2/\text{dof}$  values of  $^{51}/_{40}$  and  $^{37}/_{43}$  respectively. Especially the start of the irradiation with a slower increase

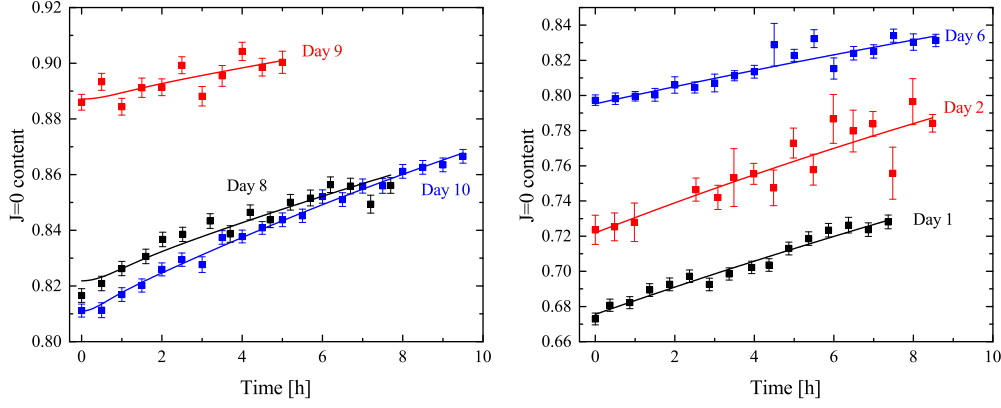


Figure 5.7.: The experimental data have been fitted with equation 3.13. The conversion rate factor  $\beta$  has been set equal for each of the two beam times. The dissociation rate  $k$  and the starting ortho fraction  $c_0$  were fitted individually for each curve.

in the ortho content is reproduced for the first beam time. For the second beam time, this behaviour is not expected, with the calculated values for the diffusion rate and the recombination rate. Table 5.2 shows the results of the fitted values for both beam times. The uncertainties were estimated by varying the window of data points, which went into the fit. As was mentioned before, the fit was set to find a combined value for  $\beta$  for each of the two beam times.

Table 5.2.: Fit results and their respective uncertainties. The conversion parameter  $\beta$  is a combined value for each beam time.  $\alpha$  was fixed for the fit and the values were taken from [Isk86]. The uncertainty for  $c_0$  comes directly from Origin Pro.

Day	$\alpha[10^{-23} \text{ cm}^3 \text{ s}^{-1}]$	$\beta[10^{-25} \text{ cm}^3 \text{ s}^{-1}]$	$k[10^{-8} \text{ s}^{-1}]$	$c_0$
Day 8	1.49	$8.5 \pm 4.0$	$5 \pm 4$	$0.821 \pm 0.002$
Day 9	1.68	$8.5 \pm 4.0$	$4 \pm 4$	$0.887 \pm 0.002$
Day 10	2.05	$8.5 \pm 4.0$	$10 \pm 4$	$0.811 \pm 0.001$
Day 1	2620	$178 \pm 80$	$12 \pm 15$	$0.676 \pm 0.002$
Day 2	2620	$178 \pm 80$	$21 \pm 15$	$0.722 \pm 0.005$
Day 6	2620	$178 \pm 80$	$13 \pm 15$	$0.795 \pm 0.002$

First of all it can be noticed, that the uncertainties for the extracted values for  $\beta$  and  $k$  are rather large and on the order of 50 – 100%. This is due to the two values not being perfectly independent in the fitting function, so that any change in the slope of the curve affects both values at the same time. Nevertheless the orders of magnitude for both values can be determined. The values for  $\beta$  for the two beam times differs by more than one order of magnitude. This is most likely due to the increased diffusion of the atoms through the crystal at higher temperatures. But it is clear that even small variations in temperature affect the mobility of the atoms greatly. Also, the recombination rate drastically changes.

Since the conversion times are similar in both beam times, the value for  $\beta$  needs to change as well, in order to compensate for the increased recombination.

The dissociation rate  $k$  also changed from one beam time to the other. This can be explained by several things. First the position of the laser focal point was set further into the cell. For the first beam time the beam had to be widened to see any effect on the ortho ratio, so that it can be assumed, that the laser was positioned in such a way that only the peripheral beam hit the focal point. The intensity of the beam was increased for the second beam time and also the focussing of the beam into the cell was improved. Although the uncertainties are very large, one can at least say that those measures worked to increase the dissociation rate.

The initial goal of the experiment was to irradiate a deuterium crystal with such an intensity, that the formation of deuterium atoms within the crystal is comparable to the situation at the FRM II. As has been discussed before, the expected value for the break-up rate is then  $k = 3.65 \cdot 10^{-7} \text{ cm}^3\text{s}^{-1}$ . This criterion was not met in the two beam times, especially for the first beam time, where the point of irradiation and the laser focal point did very likely not coincide. However, since there is no indication of a plateau forming at any point during the irradiation, it can be concluded, that up to temperatures of 10 K a conversion towards a full  $J=0$  crystal takes place.

## 5.5. Irradiated volume

With the ortho ratio values obtained for the liquid deuterium it is possible to calculate the irradiated volume. This can be done using a simple approximation where the liquid is a mixture of an irradiated component and a non-irradiated component, which remained at its ortho concentration before irradiation.

$$c_{\text{o,liq}} = v \cdot c_{\text{o,f}} + (1 - v) \cdot c_{\text{o,i}} \quad (5.3)$$

Here,  $v$  denotes the irradiated volume fraction, while  $c_{\text{o,i/f}}$  is the initial and final ortho concentration. Equation 5.3 can be easily solved for the irradiated volume. Since the beam parameters had to be adjusted on a daily basis, it is worthwhile to calculate the irradiated volume for every measurement, which has been done in the liquid phase. The calculated values are shown in table 5.3. The final ortho concentrations were calculated with the parameters from table 5.2, while the initial values were taken from the last liquid measurement for every data point.

Generally speaking only about 1/4 to 1/3 of the deuterium crystal was irradiated. In the first beam time, one can see a small jump in the volume fraction from 0.19

Table 5.3.: Calculated irradiated volumes during the experiments. The division line separates the first and second beam time.

Beam hours	Irradiated volume fraction	Uncertainty
3.2	0.08	0.37
30.9	0.34	0.05
44.7	0.23	0.11
66	0.19	0.08
90.9	0.29	0.08
102.3	0.28	0.17
16.4	0.61	0.08
41.1	0.40	0.07
50.6	0.40	0.22

to 0.29. This marks the widening of the beam towards the end of the beam time, which eventually led to the observed increase in the ortho fraction. In the second beam time, one can see the decreasing irradiated volume, which came from the improvement of the beam focussing into the cell.

For future experiments it should be considered using a widespread beam onto the target. While the beam will also hit parts of the cryo-shielding, the observed signal will be much higher and more stable, since the focal point of the Raman laser beam will always be in an irradiated area.

## 5.6. Conversion time

The  $1/e$  conversion time  $\tau$  can be extracted from the experimental data by simply fitting an exponential function to them. The results of this are listed in table 5.4. It can be noticed, that the conversion times are linked to the irradiation values  $k$  determined in table 5.2. The lower the conversion time, the higher the irradiation value, within one beam time. This is especially true for day 10 of the first beam time, and day 2 of the second. It is also noteworthy that while the dissociation rate greater for the second beam time, the conversion time  $\tau$  is roughly 30% increased. This is mostly due to the increased recombination rate of deuterium atoms. The recombination of two atoms produces a para molecule with a probability of  $1/3$ . Since the recombination is increased by three orders of magnitude, the conversion rate is slower, despite the increase in the conversion parameter  $\beta$  and the dissociation rate  $k$ .

Comparing these results with the conversion times determined by Collins et al. [Col91], differences can be noticed. Figure 5.8 shows their data. One can see, that they see a drop in conversion time from 8 to 10 K. In this work, an increase in conversion time was observed, especially considering the increased dissociation

Table 5.4.: Results of the exponential fits to the data curves.

Day	Conversion time [h]
Day 8	$31.6 \pm 2.5$
Day 9	$36.6 \pm 10.8$
Day 10	$26.8 \pm 0.7$
Day 1	$40.9 \pm 2.1$
Day 2	$31.7 \pm 2.9$
Day 6	$39.7 \pm 4.7$

rate. The authors note, that the diffusion of atoms through the crystal differs greatly from the one determined by Iskovskikh et al. [Isk86]. Two systematics could be responsible for that. First, Collins et al. measured their values in a D-T system, which need not have the same diffusion parameters as pure D<sub>2</sub>. Second, the data from Iskovskikh et al. were taken in an undamaged crystal, whereas the Collins data were taken in a D-T crystal, which irradiated and quite possibly damaged itself.

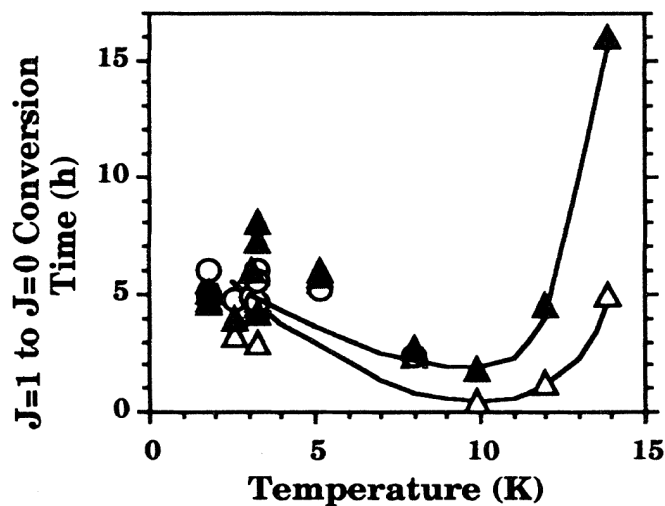


Figure 5.8.: Picture taken from [Col91]. Summary of  $J=1$  to  $J=0$  conversion times in solid D-T from 1.8 to 14 K. The tritium times are shown by empty triangles and empty circles depending on the measurement method. The deuterium times are shown by full triangles.

Other measurements, like for example Sater et al. [Sat88] have shown a minimum in conversion time around 9 K for tritium. It is very likely that this minimum also occurs in deuterium, possibly at lower temperatures, as determined in this work, while it might occur at 10 K in a D-T crystal.

The conversion time  $\tau$  is the inverse of the conversion parameter  $W_{op}$  (cf. eq.

3.13) [Col91] and can be calculated using

$$\tau = W_{\text{op}}^{-1} = \left( \beta(T) \lim_{t \rightarrow \infty} [D](t) \right)^{-1} = \left[ \beta(T) \sqrt{\frac{k[D_2]}{2\alpha(T)}} \right]^{-1}. \quad (5.4)$$

With the values for  $\beta$  determined in the two beam times, it is possible to estimate the temperature scaling of  $\beta$ . In order to reconcile the calculated temperature behaviour with the experimental data, it was necessary to decrease the value of  $t_0$  (cf. section 3.3.2) by two orders of magnitude to a value of 0.013 s. Collins et al. [Col91] state in their formalism that their value for  $t_0$  of 1 s is only empirical in nature and need not be true. In order to find a better value for  $t_0$  more measurements at different temperatures of deuterium would be necessary. For the time being, the value stated above is going to be used in all further calculations.

Figure 5.9 shows the calculated conversion time for a dissociation rate of  $k = 2.84 \cdot 10^{-6} \text{ s}^{-1}$  as it was used by Collins et al. Comparing this with fig. 5.8, a remarkable similarity can be observed. The calculated curve does reproduce the increase in conversion time towards lower temperatures. The decrease in conversion time towards 4 K can not be seen in the measured data of [Col91]. The rapid increase above 10 K is also reproduced by the calculation, albeit it does overestimate the conversion times when compared to the Collins measurements. Within the uncertainties from above the calculated absolute values also fit to the measurements. The measured data have a minimum around 10 K, which occurs between 8 and 9 K in the calculations. At 8 K the measurements show a conversion time of 3 h, while the calculation yields a value of 4 h. The conversion times then

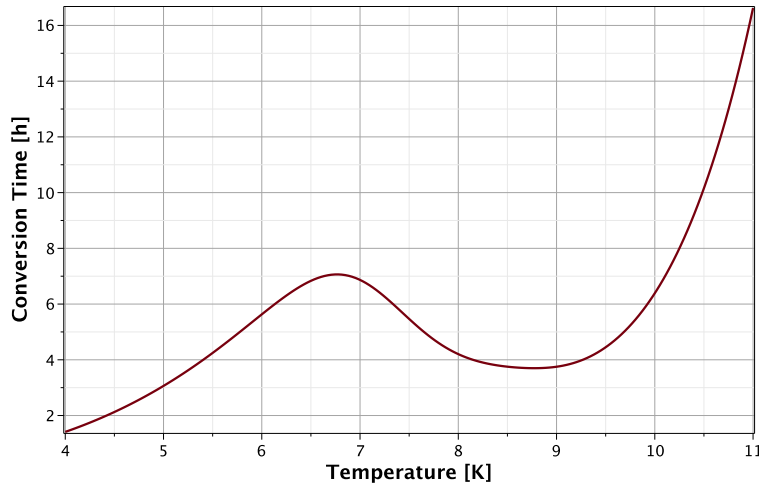


Figure 5.9.: Calculated conversion time for a deuterium crystal under irradiation with a dissociation rate of  $k = 2.84 \cdot 10^{-6} \text{ s}^{-1}$ . The increase in conversion time towards lower temperatures as seen by Collins et al. [Col91] can be partly reproduced.

almost double to a value of  $\sim 7$  h for both the calculations and the measurements, however, the maximum seen in the calculations is at slightly higher temperatures than what would be expected from the measurements.

Differences between the measurements of Collins et al. and the calculations based on the measurements done in this work could be because of the different systems in which the data were taken. Collins deduced the  $D_2$  conversion times from the signal within a D - T matrix, while the data in this work were taken in a pure deuterium crystal. With the data of this work, it cannot be determined whether the differences in the recombination and diffusion rates observed by Collins et al. and Iskovskikh et al. come from the different systems or the irradiation.

Using the value for  $k$ , which has been calculated for the ultra-cold neutron source at the FRM II ( $k = 3.65 \cdot 10^{-7} \text{ s}^{-1}$ ), it is possible to come up with a conversion time of 13h at  $T = 7.8$  K and  $\tau = 9$  h for the design temperature of 5 K. The estimated time evolution of the  $J=0$  concentration for different temperatures is shown in figure 5.10. Within two days the deuterium will have almost completely converted to its ortho state for temperatures below 10 K. For temperatures well above 10 K the conversion times increase drastically, as was already mentioned above, so that it takes weeks to convert the deuterium into equilibrium. Fig. 5.10 is significantly different from fig. 3.6. The conversion times for temperatures below 8 K are higher than what was estimated before. Also, the conversion times up to 10 K lie much closer together.

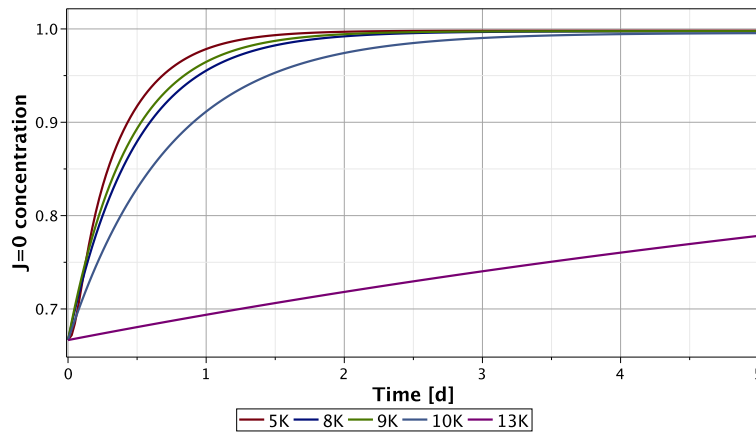


Figure 5.10.: Calculated evolution of the  $J=0$  concentration for different temperatures of the ultra-cold neutron source at the FRM II. Within two days of irradiation most of the  $D_2$  will have converted to the ortho state. For temperatures well above 10 K the conversion time increases sharply.

## 5.7. Equilibrium ortho concentrations

With the conversion parameters determined as described above, it is now possible to calculate equilibrium values for  $t \rightarrow \infty$ . This is shown in figure 5.11. The ortho concentration is shown on the  $y$ -axis while the temperature is on the  $x$ -axis. The blue line shows the natural equilibrium ortho concentration while the red line represents the values for  $t \rightarrow \infty$  calculated for the irradiation strength at the FRM II. Up to 10 K the ortho concentration is calculated to be close to 1. With increasing temperature the ortho fraction starts to drop down to values of  $< 0.75$  at 18 K.

For long irradiation times, where the concentration of deuterium atoms [D] reaches its equilibrium value the production rate of new atoms  $k$  and the recombination rate of atoms will be equal. Thus, the remaining para fraction in the deuterium can be estimated using [Col91]

$$c_{p,\text{rem}} = (1/3)k\tau. \quad (5.5)$$

$\tau$  denotes the  $1/e$  conversion time. This explains the the dip in the  $J=0$  concentration around 6 K in fig. 5.11. Since the conversion times have a maximum between 6 K and 7 K, as seen in fig. 5.9, the remaining para fraction must increase.

Nevertheless, with the equilibrium values shown in fig. 5.11 the operation of the new ultra-cold neutron source at the FRM II is well possible. No temperatures well above 10 K are expected to occur at the deuterium crystal. Fig. 5.12 shows the UCN output of a deuterium source for different concentrations of para deuterium. Very quickly the output drops by one order of magnitude already at 10 % para  $D_2$ .

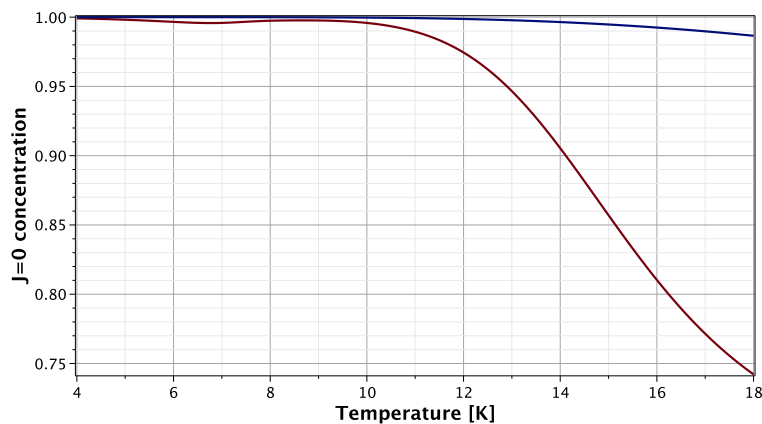


Figure 5.11.: Ortho concentration vs. temperature. The red line represents the values for  $t \rightarrow \infty$  for the irradiation strength of the FRM II. The blue line shows the natural equilibrium ortho concentration.



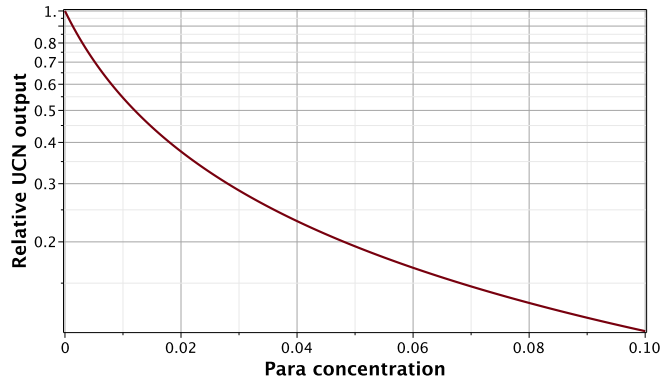


Figure 5.12.: Relative UCN output of a deuterium source for different concentrations of para deuterium. The output drops quickly even for very low para concentrations.

From fig. 5.11 it is clear, that for the UCN source at the FRM II the para values will always be below 0.5%. The deuterium, which will be frozen to the converter vessel in the SR6, will be converted to the ortho state beforehand. Values of 98.5% ortho can be expected for a conversion temperature of 20 K. This means, that the UCN output will increase by 50 – 100% over the first few days of operation, since the ortho concentration will be enhanced through the irradiation.

## 5.8. Peak widths

During the beam times with the increase in the  $J=0$  content in the crystal, it was observed that the peaks tend to become more narrow. Fig. 5.13 shows the plots for the two beam times, where the full width half maximum (FWHM) of both peaks is drawn versus the measured ortho content. It immediately becomes clear, that there is a relationship between both quantities. In the first beam time the peaks shrank by almost 1/3 of their original width. At an ortho concentration of 0.85 this trend stopped and the peak width remained almost the same. The para peak widths have a peculiar trend, as a second arm forms above  $c_o = 0.85$ .

In the second beam time only the data for the days 1, 2 and 6 are shown, since the error bars of the data for the other days would cover most of the graph. Again a clear relationship between the two quantities is visible. It can be noted that the absolute values of the two plots differ by roughly  $1 \text{ cm}^{-1}$ . Since the laser and Raman light have to travel through the crystal before reaching the focal point, it is very likely that the deuterium itself is responsible for the broadening. For the second beam time the laser was adjusted in such a way, that the focal point lies deeper in the crystal, thus the Raman light has to travel a greater distance through the crystal before reaching the optics system.

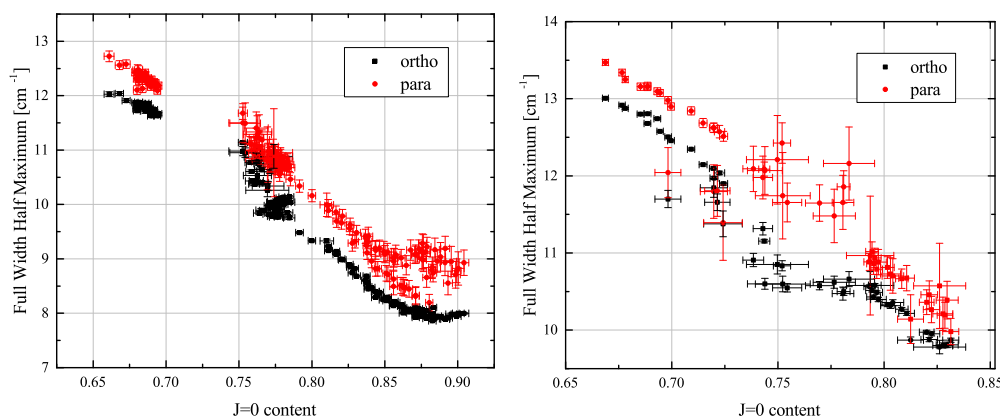


Figure 5.13.: Peak width (FWHM) of the ortho and para peaks in the Raman spectra versus measured  $J=0$  content for the first (left) beam time at 7.8 K and second (right) at 10.3 K. The peaks become more narrow the higher the ortho concentration in the  $D_2$ .

A similar dependence of the peak width on the  $c_0$  value has been observed by Bhatnagar et al. [Bha62]. They stated that the  $J=1$  molecules in the crystal provide impurity sites, which cannot be occupied by a  $J=0$  or  $J=2$  rotational excitation. Thus, the energies of the  $J=2$  rotational excitations travelling through the crystal are modified and the transition band becomes more diffuse [Bha62]. However, it must be noted, that this effect should only affect the ortho peaks, since the  $J=1$  excitations see more and more impurities, which they cannot occupy. It might also be possible, that the Raman lines are broadened by scattering on crystal defects during the travel through the crystal. The higher the ortho concentration in the crystal, the better the thermal conductivity, and thus the crystal quality. Then, the Raman light would undergo fewer scattering events and thus, the broadening of the lines would be reduced. However, if this were the case, the FWHM values would depend on the fitting uncertainties, which are also a measure for the crystal quality, since a worse crystal has less intensity in the Raman lines, which in turn reduces the fit quality. This dependence cannot be seen in fig. 5.13.

The data in fig. 5.13 have been fitted with two linear functions. The first function for values ortho values between 0.66 and 0.72 and the second one for ortho values between 0.79 and 0.85. The fitted values for the slopes are summarized in table 5.5.

For both beam times the slopes for the first fitting window are smaller than the slopes for the second window. Between the two beam times the values for the second window agree very well within the fitting uncertainty. The slopes for the ortho and para portions of the fits also agree well, indicating that there is a universal mechanism in place, which enhances the peak width during irradiation. Unfortunately, no definitive answer can be given as to why the peaks become more narrow the higher the  $J=0$  concentration within the crystal. It should be

Table 5.5.: Results of the linear fits to the data in fig 5.13. The division line separates the first and second beam time.

Fitting region	ortho/para	Fitted slope [ $\text{cm}^{-1}$ ]
0.679–0.695	ortho	$-12.85 \pm 1.95$
0.679–0.695	para	$-12.45 \pm 3.00$
0.793–0.831	ortho	$-21.35 \pm 0.81$
0.793–0.831	para	$-21.24 \pm 0.83$
0.669–0.720	ortho	$-19.03 \pm 1.20$
0.669–0.720	para	$-16.68 \pm 0.48$
0.793–0.830	ortho	$-20.97 \pm 1.41$
0.793–0.830	para	$-19.88 \pm 2.44$

added, that this effect can also be observed within the liquid deuterium, albeit with a much gentler slope.

Nevertheless, it is worth studying this effect with even higher ortho concentrations. For this the deuterium can also be ortho-enriched through a catalysis process. Due to the  $J=2$  excitations forming an excitation band in the solid, one should be able to see a splitting of the  $J = 0 \rightarrow 2$  line into three separate lines [VK60, Bha62], given that the spectrometer can resolve lines separated by  $\sim 3 \text{ cm}^{-1}$ .

## 5.9. Small para fractions and limits of the method

Even though in both beam times no ortho fractions higher than 0.94 were reached, it is useful and possible to give limits on the capabilities of the measuring equipment. The experimental limit in determining small para fractions is given by the ability to see the para peak.

On the beam days, where the deuterium crystal had the worst quality, the intensity of the para line was also the lowest. Taking this value as a minimal value for the para intensity and also an ortho peak value of a very good quality crystal, one can now estimate an ortho/para ratio. The least intensity para Raman line had an area of  $(7044 \pm 876) \text{ cm}^{-1}$ . In contrast to that, the highest intensity ortho line measured had an intensity of  $(1.338 \pm 0.003) \cdot 10^6 \text{ cm}^{-1}$ . Together with the value for the correction factor of  $\kappa = 0.77$ , an ortho concentration of  $0.993 \pm 0.001 \pm 0.002$  can be calculated. Thus, it should be easily possible to determine para fractions of  $< 0.005$ .

For para fractions of  $< 0.2$ , there is also the possibility of using the vibrational lines  $Q_1(0)$  and  $Q_1(1)$  of deuterium as means to determine the ortho/para ratio. Fig. 5.14 shows a comparison of the vibrational lines for two different ortho fractions. The spectrum was taken with a minimal entrance slit width of the Raman

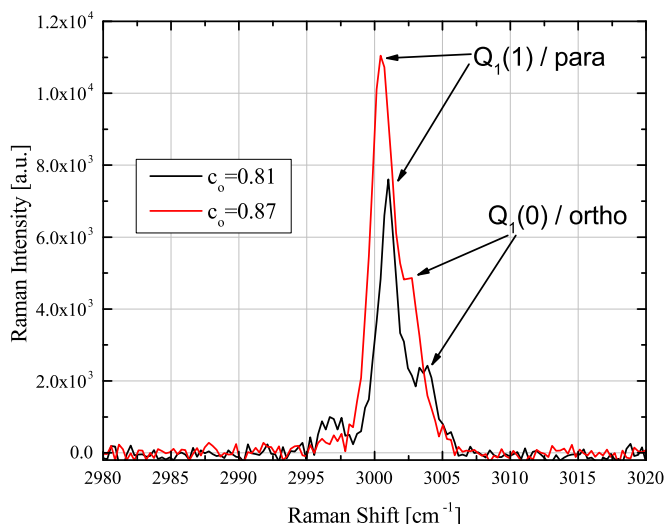


Figure 5.14.: Vibrational Raman lines of deuterium for two different  $J=0$  concentrations. Here the para line is the more intense one. Both lines should have equal intensity at  $c_o = 0.98$  [VK83].

spectrometer of  $10\ \mu\text{m}$ . Hence, the line width is greatly reduced to  $1.5\ \text{cm}^{-1}$  when compared to the rotational Raman lines. Both of the lines can be easily separated, even though they are only  $\sim 2\ \text{cm}^{-1}$  apart. The Raman shift calibration is not perfect, since the lines are expected to lie at  $2983\ \text{cm}^{-1}$  and  $2985\ \text{cm}^{-1}$ . Nevertheless, the intensities of both lines are expected to be the same at an ortho fraction of  $c_o = 0.98$  [VK83]. Examining the vibrational Raman lines at low para fractions should then prove useful, provided the intensity of those lines is big enough.

Van Kranendonk [VK83] calculated the cross-section ratio of the  $Q_1(0)$  and  $Q_1(1)$  lines  $\xi(c_o = 1)$  to be 55. For values of  $c_o$  down to 0.5  $\xi(c_o)$  is a strong function of the ortho ratio, dropping to values of  $\xi(c_o = 0.5) = 5$ . For very small ortho fractions of less than 0.02 the ratio of the cross-sections can roughly be estimated employing [VK83]

$$\xi(c_o) = 250c_o - 195. \quad (5.6)$$

Thus, it is possible to estimate the ortho/para ratio for small para contents by measuring the vibrational Raman lines. It must be stressed though, that this is only an estimate, as exact knowledge of the polarizabilities of the deuterium molecules at the laser wavelength of  $\lambda = 532\ \text{nm}$  are necessary for an exact calculation. It was unfortunately not possible to find literature values for these. However, employing eq. 5.6 it should well be possible to estimate the ortho content in a given solid deuterium sample above  $c_o = 0.995$ .

## 5.10. Literature overview concerning D<sub>2</sub> irradiation

Over the last decades there have been numerous attempts to irradiate the hydrogen family and study the effects, which arise from the irradiation. The work of Collins et al. [Col91] has already been shown extensively during this chapter.

Shevtsov et al. [She94] implanted small amounts of atomic hydrogen in a molecular hydrogen solid ( $\sim 500$  ppm). They investigated the ortho-para conversion with ESR and NMR techniques. While they saw an increase in para conversion due to the implanted atoms, they concluded that the catalyzed rate is much less than what would be expected. A possible explanation is that the diffusion of H atoms is very confined in the crystal.

Sater et al. [Sat88] measured the self-conversion of tritium, which is enhanced due to the self-irradiation. They also observed a minimum in the conversion time  $\tau$ , which occurs between 10 K and 11 K. They also studied the recombination rates and equilibrium atom concentrations in the solid tritium. They came up with a so-called “hopping-model” for the diffusion of atoms through the crystal. However, it remains unclear, whether their values can be used for the analysis of deuterium.

Atchison et al. and K. Mishima [Atc03, Mis04] studied the irradiation effects on liquid deuterium of the SINQ liquid moderator at the PSI in Switzerland. After several weeks of irradiation, they extracted a D<sub>2</sub> sample and measured an ortho fraction  $c_o = 0.762 \pm 0.007$ . This means, that irradiating deuterium at liquid temperatures for ortho conversion is no option, because only partial conversion takes place. This work could now show, that the irradiation of the solid is in fact a viable way to achieve high ortho concentrations.

Other effects rather than the change in the ortho content were also studied. Bondoux et al. [Bon09] irradiated solid deuterium with an intense beam of electrons. They did not check for any change in the ortho fraction, but rather studied, if the energy stored in atomic deuterium is released after some atom concentration is reached, or if such a quench could be initialized through temperature variations as had already been seen in solid methane [Car87]. However, they did not observe any rapid temperature changes.

Brooks et al. [Bro83, Bro85] studied the infrared absorption spectra in irradiated deuterium. It was observed that additional features appear in all hydrogens near the vibration lines in the spectra. Those features persisted for long times after the irradiation and could be quenched by heating the crystal to temperatures above 12 K. Those features were then attributed to a concentration of D<sub>3</sub><sup>+</sup>, which accumulated in the irradiated solid.

Furthermore Forrest et al. [For94, For97] observed a continuous red emission in proton-irradiated deuterium. This emission persisted even at temperatures near

the melting point and also tens of minutes after turning off the irradiation. Optical flashes could also be observed after several minutes of proton irradiation. Those flashes are linked to the continuous emission in the sense, that after irradiation, if such a flash occurs, the continuous emission also stops. They say that radiative electron attachment to unpaired atoms (forming  $D^-$ ) is the most likely explanation for these emissions. All in all, they conclude that mobilities of all species is much higher in hydrogen than in deuterium.

It becomes clear, that the irradiation of solid deuterium is an interesting field of study, where still not all effects and observations are understood. This work delivered results, which help to further understand those effects. For the first time it was shown, that irradiation in fact enhances the ortho concentration in the deuterium solid. A model has been presented in which atomic deuterium is the driving force behind the process.

## Chapter 6.

# Diffuse reflectivity of UCN guides

---

Not only the efficient production and extraction of the ultra-cold neutrons out of the deuterium converter is important. Once the UCN leave the converter, they have to be transported to the various experimental areas. At the Forschungs-Neutronenquelle Heinz Maier-Leibnitz (FRM II) the experiments for the new ultra-cold neutron source will have a maximum distance of 30 m from the source. In order to bring at least half the UCN to the those experiments one needs a guide transmission of at least  $0.977 \text{ m}^{-1}$ . Owing to the high radiation doses surrounding the UCN source at the FRM II, standard glass neutron guides cannot be used to transport the neutrons. They would be destroyed within several months. Instead so-called “Replika” guides made from a NiV alloy (cf. chapter 2.4.1) are foreseen as a guiding material for the UCN. Two parameters are crucial in the transmission of UCN guides. First, the loss probability per wall bounce  $\mu$  and second, the probability for a diffuse reflection  $d$ . This chapter will first give a short overview of the loss parameters and then will focus on an experiment designed and conducted to measure the diffuse reflectivity of the Replika guides. Parts of this chapter have been handed in for publication [Wl15].

### 6.1. Loss parameters

#### 6.1.1. Loss on wall bounce

On reflection off a surface the probability density function will enter the reflecting medium and decay exponentially. This means that there are several ways for a neutron to be lost on a collision. First, it can be absorbed in the guide material and second it can be upscattered in the medium. There is also the chance for the neutron to be absorbed on any Hydrogen contaminants on the surface of the wall material.

If one defines a loss potential [Gol91]

$$W = \frac{\hbar}{2} \sum_i N_i \sigma_i v \quad (6.1)$$

one can redefine eq. 1.7 as

$$U = V + iW. \quad (6.2)$$

Together with  $f = W/V$  one can now write for the loss probability on wall bounce  $\mu$  [Gol91]

$$\bar{\mu}(E) = 2f \left[ \frac{V}{E} \arcsin\left(\frac{E}{V}\right)^{1/2} - \left(\frac{V}{E} - 1\right)^{1/2} \right] \quad (6.3)$$

The wall loss probabilities of the Replika guides, foreseen for the UCN source, have been successfully determined in [Hub11]. They are on the order of  $10^{-4}$  for all the tested guides pieces. The total transmission was determined to be  $(0.990 \pm 0.006) \text{ m}^{-1}$ .

### 6.1.2. Diffuse reflection

Diffuse reflection is of great importance for the transmission of UCN guides. Due to the surface structure of the guide, a fraction of the UCN will not scatter specularly but diffusely. There are several models in use to describe the diffuse reflection.

- The easiest description can be made employing Lambert's law for light scattering, stating that the scattered waves will have a Cosine distribution.
- The so-called micro-roughness [Ste72, Ste91] describes the surface as a perfect plane at  $z = 0$  with small deviations from flatness with the mean fluctuation  $\langle \xi \rangle = 0$ . The probability of non-specular reflection of a UCN with wave vector  $k$ , incident at  $\theta_i$  ( $\phi_i = 0$ ) with respect to the normal surface with a mean surface roughness  $b$  and lateral correlation length  $w$  can be written as [Ste72, Atc10]

$$I_{\text{ns}}(\theta_f, \phi_f) = \frac{k_c^4}{8\pi} \cdot \frac{b^2 w^2}{\cos\theta_i} |S(\theta_i)|^2 |S(\theta_f)|^2 \times e^{-\frac{w^2 k^2}{2} (\sin^2\theta_i + \sin^2\theta_f - 2 \sin\theta_i \sin\theta_f \cos\phi_f)}. \quad (6.4)$$

There have been several other methods derived to describe the diffuse scattering of neutrons (and X-rays) [Nev80, Sin88, Pyn92]. These models not always yield consistent solutions. Up to now there has been no model which could accurately describe the diffuse scattering with one set of parameters for different lengths of



the same type of guides. In the analysis here a modified Lambert law will be used. Instead of having a cosine distribution around the normal vector of the guide plane, a cosine distribution around the vector of specular reflection is used. This model is rather easy to implement in a simulation code since it does not rely on a separate measurement of surface properties of the UCN guide.

## 6.2. Experimental Methods

### 6.2.1. Fixed angle method

In the fixed angle method the incoming UCN beam is collimated in such a way that only UCN with a specific angle towards the guide axis (typically  $40^\circ - 50^\circ$ ) can actually enter the guide volume [Plo07, Atc10]. One can now either have a second stage of slits behind the guide volume (which blocks diffusely reflected neutrons) or tilt the guide stage in such a way, that the gap is smaller at the end than in the beginning (which blocks specularly reflected neutrons).

Such an experiment has been done at PSI [Plo07, Atc10] for different materials and configurations. For NiV guides, such as are planned for the UCN source at the FRM II, they found diffuse reflectivity probabilities of 1.0%, both for a Lambert model calculation and a micro-roughness model. Although both methods yield rather similar values, the  $\chi^2$  value for the Lambert model is significantly worse.

### 6.2.2. The helium method

The helium method [Ign96] in contrast to the fixed angle method uses all of the available UCN flux. The guide volume is filled with different gas pressures of helium. If a UCN interacts with a helium atom it will be upscattered, since the RMS velocity of helium is on the order of  $1200 \text{ m/s}$ . The diffuse reflectivity on average increases the path length which a neutron takes. Thus, the longer the path length, i.e. the higher the diffuse reflectivity, the more neutrons will be lost due to the increased interaction with the helium gas. If one looks at the relative transmission vs. the helium pressure, one would expect the curves to fall steeper with increasing diffuse reflectivity.

In diffusion theory one can calculate the flux  $J(Z)$  at a position  $Z$  along the guide axis to be [Gro71, Gol91]

$$J(Z) = J(0) \left[ \cosh\left(\frac{Z}{L}\right) + \gamma \sinh\left(\frac{Z}{L}\right) \right]^{-1} \quad (6.5)$$

with

$$\gamma = \frac{L\bar{v}}{4D}. \quad (6.6)$$

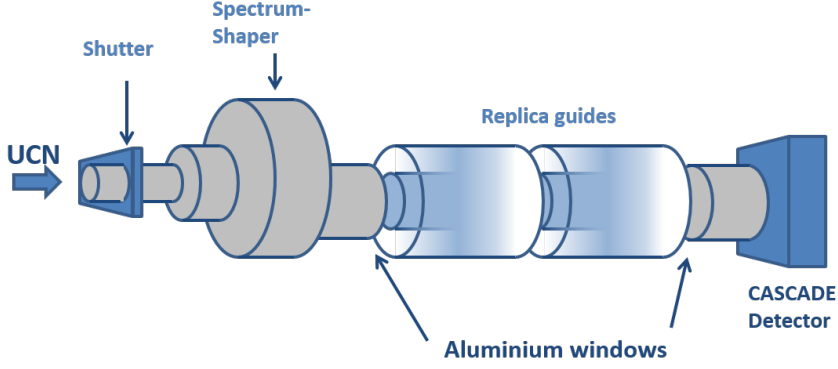


Figure 6.1.: Sketch of the helium transmission experiment. After passing a spectrum shaper the UCN enter the Replika guide volume through an aluminium foil. The guide volume is filled with different helium pressures. After passing a second foil the UCN are guided to the detector.

Here,  $L^2 = D\tau$  is the diffusion length, with the diffusion constant  $D$  and the mean lifetime of the neutrons in the guide  $\tau$  and  $\bar{v}$  is the mean velocity of the UCN. Substituting  $\frac{1}{\tau} + \frac{1}{\tau_{\text{He}}}$  for  $\frac{1}{\tau}$  one finds an expression for the pressure dependent diffusion length [Ign96]

$$L_D(p) = L_D(0) \sqrt{\frac{\tau_{\text{He}}}{\tau + \tau_{\text{He}}}}. \quad (6.7)$$

If one has reflections that can either be specular or diffuse, one finds that the diffusion constant can be written in the following way [Gol91].

$$D_{\text{spec}} = \frac{2-d}{d} D_{\text{diff}} \quad (6.8)$$

With these information it is in principle possible to fit measured data and get values for the diffuse reflectivity  $d$ .

### 6.3. Experimental setup

The experiment was conducted at the PF2/TES [Ste86] beam at the Institute Laue-Langevin. It is sketched in fig. 6.1. Neutrons first pass a VAT shutter which closes the experiment to UCN when necessary. Then they pass a stainless steel spectrum shaper, which cuts off most neutrons above an energy of 190 neV [Dau12]. The NiV Replika guides have a calculated Fermi potential of  $V_{\text{NiV}} = 227$  neV. Therefore all neutrons entering the guide volume, can be transported. The Replika guide volume was enclosed on either side with a  $100 \mu\text{m}$  thick AlMg3 window. The transmission of both windows together is more than 80 % [Atc09]. After passing the second window, the UCN are guided to the CASCADE detector [Kle14] through a 30 cm long stainless steel tube.

The guide volume could be filled with He pressures from 0 – 500 mbar. The helium had a purity of 99.996 %. Before reaching the guide volume, the helium was passed through a nitrogen trap to remove any residual water and other gaseous contaminants. The biggest uncertainty, due to gas contamination in the bottle, comes from helium-3, where the loss due to absorption has been calculated to be less than 1 %. While the concentration of other contaminants might be higher (20 ppm for N<sub>2</sub>), their neutron absorption cross-section and rest-gas collision cross-section (see eq. 6.10) is far less and they can thus be neglected.

The guide volume was evacuated to  $5 \cdot 10^{-4}$  mbar before each run. A transmission measurement could then be performed without helium. The pressure was then increased in several steps up to the desired 500 mbar. At each step a measurement was done. The measurement time was varied so that roughly  $10^5$  counts were observed. The length of the guide system was varied between 1 – 3 m.

The preamplifier signals from the detector were first amplified through a CAEN 968 amplifier module and then send to a PC where the signals were analysed in a MCA 3A. The whole experiment, including pressure sensors, valve movement, etc. were controlled from a self-written control software.

In fig. 6.2 one can see the actual experimental setup at the ILL. The Replika guide pieces are placed in vacuum cladding tubes because the Replika sheets are not thick enough to support vacuum. The detector had to be placed in a Faraday cage to reduce electronic noise.

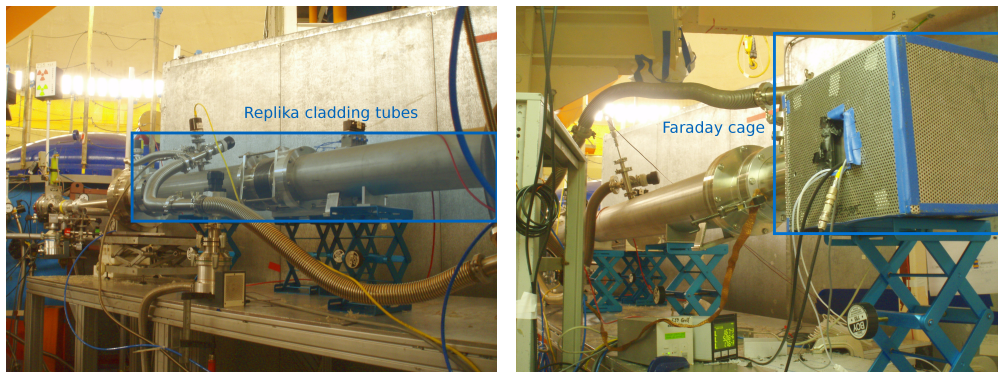


Figure 6.2.: The experimental setup at the ILL PF2/TES beam. The Replika tubes are placed in stainless steel vacuum tubes. The detector is enclosed in a Faraday cage to protect it from electronic noise. Outside the Replika guide volume the UCN are guided by stainless steel tubes.

## 6.4. Results

### 6.4.1. Beam time results

Figure 6.3 shows the count rates at different pressures normalized to the count rate at vacuum conditions. The different data points have been corrected for the respective mean reactor power at the time of the measurement. The error bars show statistical errors plus the errors due to the reactor power fluctuations. The reactor power errors have been doubled to account for the greater power fluctuations during the beam time.

The count rate for every length is decreasing with increasing helium pressure as can be expected. The transmission values for the longer guides are lower than for the shorter guide pieces, because the UCN have a longer path through the helium. In the case of no diffuse reflectivity one would expect the transmission curve to be an exponential.

$$\frac{I}{I_0} = e^{-n_{\text{He}}(\sigma_{\text{sc}} + \sigma_{\text{abs}})\bar{L}} \quad (6.9)$$

Here,  $n_{\text{He}}$  is the helium atom density,  $\sigma_{\text{sc}}$  and  $\sigma_{\text{abs}}$  are the cross-sections for scattering and absorption and  $\bar{L}$  is the mean path which a neutron takes through

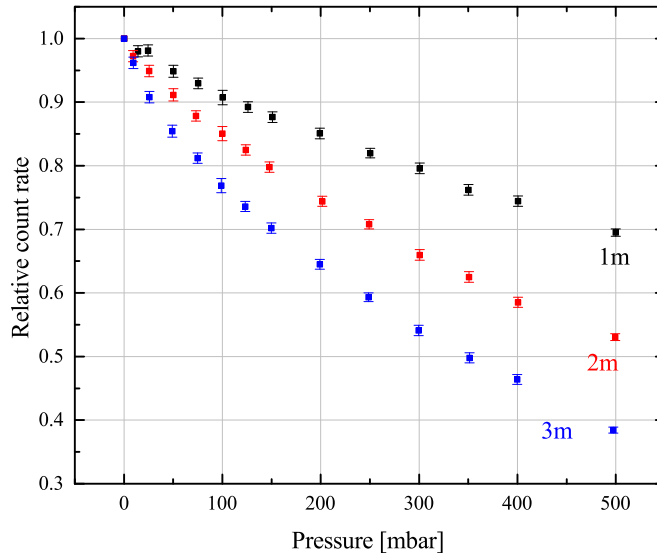


Figure 6.3.: Relative count rates vs. helium pressure in the guide system. The error bars are statistical errors plus a reactor power correction. Since all data are normalized to their respective count rates at zero pressure, the error bars have been omitted for those  $p = 0$  values.

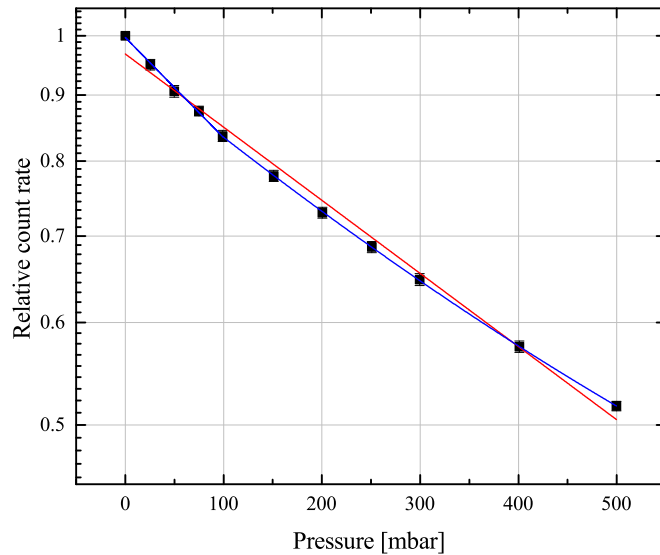


Figure 6.4.: Logarithmic plot of the helium transmission curve for 2 m guide length. The red curve shows a single exponential fit while the blue curves show two separate exponentials.

the helium. As one can see in figure 6.4 the data do not lie on a single exponential. The red curve in figure 6.4 shows a single exponential fit. It is clear, that the curve deviates for low and high pressures. The blue line shows two separate exponential fits. One fit is ending at 100 mbar while the second one starts there.

If one takes a simple binomial distribution model for the number of diffuse scattering events in the guide system, one arrives at the result, that even for the longest guide system the UCN will undergo less than 5 diffuse scattering events, considering a probability for diffuse reflection of 3%. Now, one can interpret the results in the following way: Most of the UCN are scattered in a forward direction along the guide or their direction is barely altered by a diffuse scattering event. These neutrons have a higher probability of survival even at higher helium pressures. The other part of the UCN are backscattered or scattered towards high angles with respect to the guide axis. Those neutrons will take long paths through the guides and are therefore strongly affected by the helium. These are the neutrons responsible for the stronger decrease in the first part of the helium curve.

### 6.4.2. Simulation

In order to extract more information from the experiment, a GEANT4 [Ago03] simulation was set up. It contained all the parts of the experiment which have been described in chapter 6.3. This can also be seen in figure 6.5. It is a view of the simulated setup. All aluminium windows and the spectrum shaper have been simulated. The helium volume is shown in blue, the detector is shown in light blue.

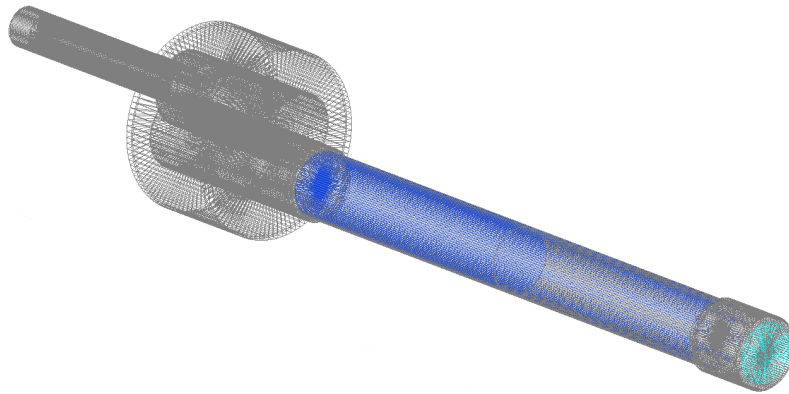


Figure 6.5.: View of the simulated setup. The geometry includes the complete setup of the experiment with the spectrum shaper and aluminium windows. The helium volume is shown in blue, the boron layer of the detector is shown in light blue.

The following formula was used to describe the interaction of the UCN with the helium atoms [Bec64]

$$\sigma_{\text{up}}(E_{\text{UCN}}) = 2\sigma_0 \sqrt{\frac{k_{\text{B}}T}{A\pi E_{\text{UCN}}}} \times \frac{4m_{\text{n}}M}{(M + m_{\text{n}})^2}. \quad (6.10)$$

In this case,  $\sigma_0$  is the thermal neutron scattering cross-section (1.34 barn),  $A = 4$  is the mass ratio of helium atoms and neutrons,  $m_{\text{n}}$  and  $M$  are the masses of the neutron and the helium atom and  $E_{\text{UCN}}$  is the energy of the UCN.

The diffuse reflection mechanism was modelled after the Lambertian reflection mechanism. Instead of scattering in a cosine distribution about the axis of the surface normal vector, the simulation scattered the neutrons around the axis of the specular reflection. Since at the time of the measurements part of the UCN turbine at the ILL were contaminated with Fomblin oil from previous experiments, the aluminium windows of the experiment were given the Fermi potential of the oil ( $V_{\text{Fom}} = 106$  neV) instead of pure aluminium ( $V_{\text{Al}} = 54$  neV). This severely alters the momentum spectrum of UCN which are allowed to enter the helium volume. Especially the angular distribution of the neutrons is changed, as the higher Fermi potential leads to UCN being more forward peaked, so that the relative transmission is increased.

The spectrum of the incoming UCN velocities was set to a gaussian profile with a mean velocity of  $10$  m/s and a spread of  $5$  m/s which roughly corresponds to the conditions at the PF2/TES beam [Zec15]. Figure 6.6 shows the results of the simulation. The simulated data are shown in black, the experimental data in red and the double exponential fits are shown as red lines through the experimental data points. For each of the data points  $3 \cdot 10^7$  particles were simulated. The diffuse reflection probability for the Replika guides in the simulation was set to 0.030. By varying the diffuse reflectivity in the simulation the error has been

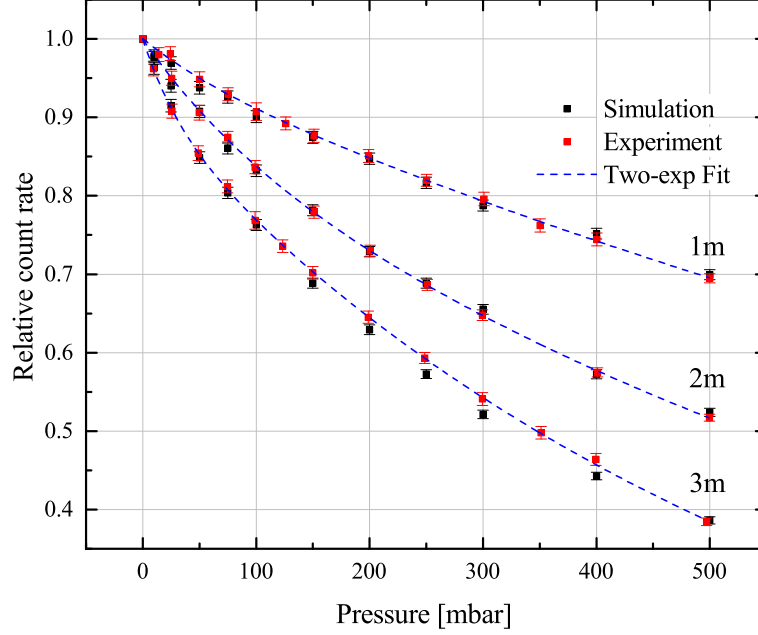


Figure 6.6.: Comparison of simulated (black) and experimental (red) data. The experimental data are fitted with a double exponential (dashed blue lines). The diffuse reflectivity in the simulation was set to  $3.0 \cdot 10^{-2}$ . Figure has been handed in for publication [Wlo15].

determined to be 0.005. In order to measure the quality of the simulated data a quality number was defined in the following way

$$\epsilon^2 = \frac{(y_{\text{dat}} - y_{\text{sim}})^2}{\sigma_{\text{dat}}^2 + \sigma_{\text{sim}}^2}. \quad (6.11)$$

This definition is analogous to the usual definition of a  $\chi^2$  number. With this definition a value of  $\frac{\epsilon^2}{\text{DOF}} = \frac{28}{31}$  is obtained, which shows a good agreement between simulation and experiment.

## 6.5. Conclusions

The simulated data reconstruct the experimental data points quite well. This shows that the modified Lambert model accurately describes the diffuse scattering process in UCN guides. NiV alloys have been tested before [Atc10]. The diffuse reflectivity of NiV has been determined to be 1.0%. One has to keep in mind that they used the standard Lambert model which yields lower values for the same transmission.

The measurement presented here was the first time that one set of parameters could be used to describe guides of different lengths. The simulations show that

Table 6.1.: Calculated values for the mean path lengths of UCN through the helium volume.

Guide length	$L_1$ [m/m]	$L_2$ [m/m]	$\bar{L}$ [m/m]	$A$
1 m	$1.47 \pm 0.04$	$35.60 \pm 13.49$	$2.66 \pm 0.53$	$0.965 \pm 0.007$
2 m	$1.22 \pm 0.03$	$11.46 \pm 1.29$	$2.33 \pm 0.17$	$0.892 \pm 0.010$
3 m	$1.28 \pm 0.01$	$23.43 \pm 2.65$	$3.30 \pm 0.26$	$0.909 \pm 0.004$

UCN arriving at the detector have a median energy of  $\bar{E} = 185$  neV ( $\bar{v} = 5.95$  m/s). Assuming that one can describe the helium transmission with two exponentials of the form of eq. 6.9 and that for both exponentials only the mean path length  $\bar{L}$  is different, one can calculate these mean path lengths. The results of this calculation are summarized in table 6.1.

The values  $L_1$  show the shorter component of the helium curve, which represents the UCN, which can sustain higher helium pressures. One can see that the UCN momentum spectrum changes within the first meter, thus the path length is still longer than for the other two lengths. The mean path length for zero diffuse reflection probability extracted from simulations is 1.27 m per meter guide length. This does correspond to the  $L_1$  values.

The values for  $L_2$ , representing the UCN strongly affected by the helium, are an order of magnitude higher than the  $L_1$  values. The values for  $L_2$  show a much greater spread, indicating that statistics might not be enough to draw solid conclusions about the exact value. The last column shows a mean path length  $\bar{L}$  calculated using

$$AL_1 + (1 - A)L_2 \quad (6.12)$$

where  $A$  is the pre-factor from the two exponential fit. From the simulations one can also get a median path length  $\bar{L}_{\text{sim}} = 2.22$  m/m. Both values for simulation and experiment fall within the same region. The values do not agree perfectly, which again might be due to limited statistics for the  $L_2$  values, since the effect is only visible in the first 4-5 data points until 150 mbar and the exponential fit has to use at least two variables.

The values for  $A$  range from 0.89 to 0.97. One would expect a decrease of  $A$  for longer guide length, since the probability for a diffuse scattering event increases with the guide length. While this is certainly the case for the 1 m and 3 m measurement, it does not prove valid for the 2 m measurement. This is very likely due to an imperfect connection of the different guide pieces and thus a slight misalignment of the guide. This then adds to the diffuse scattering.



# Chapter 7.

## Analysis of Pure Helium-4

---

### 7.1. Motivation

Helium is the main cooling medium used in the new ultra-cold neutron source at the FRM II. Not only will it cool the deuterium and hydrogen in the converter vessel, but also the surrounding double-walled aluminium tube. While  $^4\text{He}$  does not absorb neutrons [Sea92], any commercially available helium will contain  $^3\text{He}$  which has a high thermal absorption cross section of 5333 barn [Sea92]. Because of its high absorption cross section the amount of tritium produced through neutron capture is still significant despite the low natural abundance of  $^3\text{He}$  of  $1.4 \cdot 10^{-6}$ . Commercially available helium still has  $^3\text{He}$  contents ranging from  $(1.6 - 3.0) \cdot 10^{-7}$ . A detailed calculation of the tritium production in the helium system of the UCN source has been done in [Fre11].

The tritium is produced through the following reaction:



It will subsequently decay through



with a half-life of  $t_{1/2} = (4500 \pm 8) \text{ d}$  [Luc00]. This means that tritium production and decay are coupled together since no other processes produce tritium or helium-3. A decrease of helium-3 is linked to an increase in the tritium content and vice versa. The tritium activity in the converter cooling cycle can be calculated using [Fre11]

$$A = N_{\text{He},0} \frac{\alpha \lambda}{\alpha + \lambda} \left( 1 - e^{-(\alpha + \lambda)t} \right). \quad (7.3)$$

$\lambda = 1.78 \cdot 10^{-9} \text{ s}^{-1}$  [Luc00] is the decay constant of tritium and  $\alpha$  is the production rate coefficient which links the number of produced tritium atoms per second to the number of helium-3 atoms in the sample. The value for  $\alpha$  varies between  $2.5 \cdot 10^{-9} \text{ s}^{-1}$  and  $4.5 \cdot 10^{-8} \text{ s}^{-1}$  [Fre11] for the different cooling subsystems.

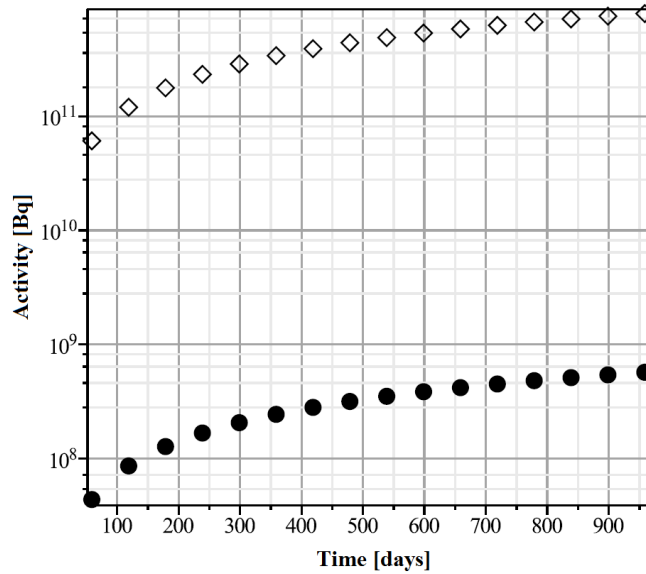


Figure 7.1.: Total tritium activity over time in the cooling systems of the UCN source for two different  ${}^3\text{He}$  concentrations. Empty squares represent the natural helium composition. Black circles represent a  ${}^3\text{He}$  content of less than  $10^{-9}$ . Each mark represents the end of one reactor cycle.

Fig. 7.1 shows a comparison of the tritium activities after a certain amount of time for two different concentrations of  ${}^3\text{He}$ . The empty squares depict the natural helium composition while the filled circles represent a  ${}^3\text{He}$  concentration of less than  $10^{-9}$ . The activity decreases almost linearly with the  ${}^3\text{He}$  concentration, so it is about 3 orders of magnitude smaller for the purer  ${}^4\text{He}$ . The activities for the pure helium are in the order of magnitude of the activities of the irradiated hydrogen in the UCN source [Fre11]. This is 1 – 2 orders smaller than the activity of the irradiated deuterium [Fre11]. In return, the design of the cooling facilities is greatly facilitated, since there is no need to contain activity, which is never produced.

This chapter will focus on an experimental campaign to measure the  ${}^3\text{He}$  content in a standard sample obtained from a gas bottle and compare it to a pure helium sample bought from Lancaster University [Hen87].

## 7.2. Experiment

In order to measure the  ${}^3\text{He}$  concentration, the helium sample is first irradiated in the FRM II research reactor. The tritium can then be detected in a single wire gas detector [Gre11, Wlo11].

The helium samples were prepared in glass cuvettes with an inner volume of

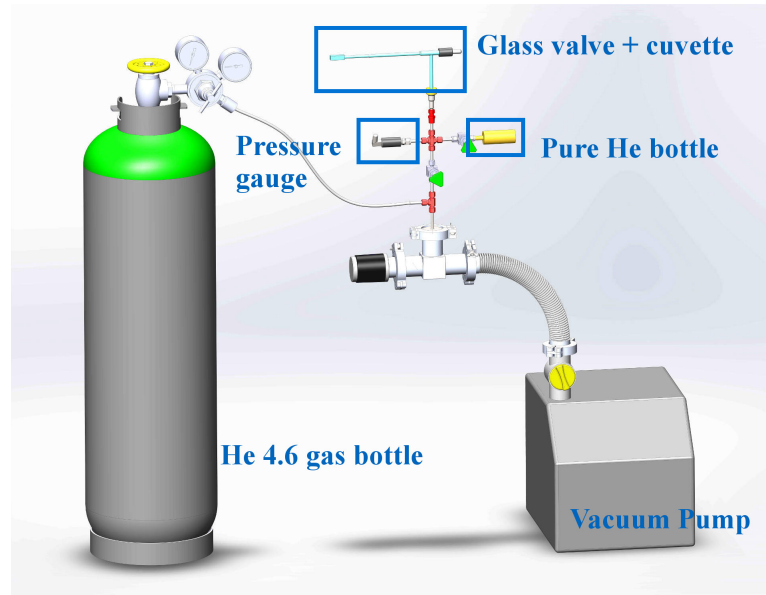


Figure 7.2.: Scheme of the helium filling device used to fill the glass cuvettes with pure helium. The system was first evacuated. Afterwards the system could be filled with helium from a gas bottle or purified  $^4\text{He}$ .

$3.5\text{ cm}^3$ . This made it possible to irradiate the helium without producing long lived irradiation products in the container. It was also possible to bring the helium in contact with the measurement gas in the detector by simply destroying the cuvette.

The glass cuvettes were standard fluorescence measurement cuvettes from Hellma GmbH & Co. KG. The filling device is shown in fig. 7.2. They were first evacuated down to  $\sim 10^{-5}$  mbar. After that they were filled with either a natural composition helium gas from a pressurized gas bottle (Helium 4.6) or purified helium from Lancaster University [Hen87]. The pressure of the helium inside the cuvette was monitored. A total of 4 samples were prepared this way, 2 of which with the pure helium. The pressures within the cuvettes was 650 mbar and 500 mbar respectively. Before the actual irradiation the samples had to be melted off the glass valves, which were attached previously. This was done in such a way, that no air could enter the sample volume during the melting. This was aided by the low pressure inside the cuvettes. The possible contaminants of the helium gas bottle (nitrogen, oxygen, water, carbo-hydrates) are unproblematic. Neither of these materials can produce unstable isotopes in a single neutron capture. Any double neutron captures can be neglected, since the probability for such an event is very low.

The samples were irradiated at the KBA 2-1 facility at the FRM II. The thermal neutron flux density at this position is  $\phi = 1.1 \cdot 10^{14} \text{ cm}^{-2}\text{s}^{-1}$ . The irradiation time was  $t = 2$  h. Since  $\sigma\phi \gg \lambda$ , the resulting tritium activity can be calculated

by using a first order approximation

$$A_T = n\sigma\phi\lambda t. \quad (7.4)$$

Here,  $n$  is the  $^3\text{He}$  atom density,  $\sigma = 5333$  barn [Sea92] is the neutron absorption cross-section of  $^3\text{He}$ . For a natural composition helium sample this results in  $A_T = 880$  Bq and  $A_T = 660$  Bq for the two different pressures. For the commercially available gas, one would expect  $75 \text{ Bq} < A_T < 180 \text{ Bq}$ . These activities can be well measured with the tritium detector setup developed in [Gre11, Wlo11] where activities as low as 10 Bq were measured.

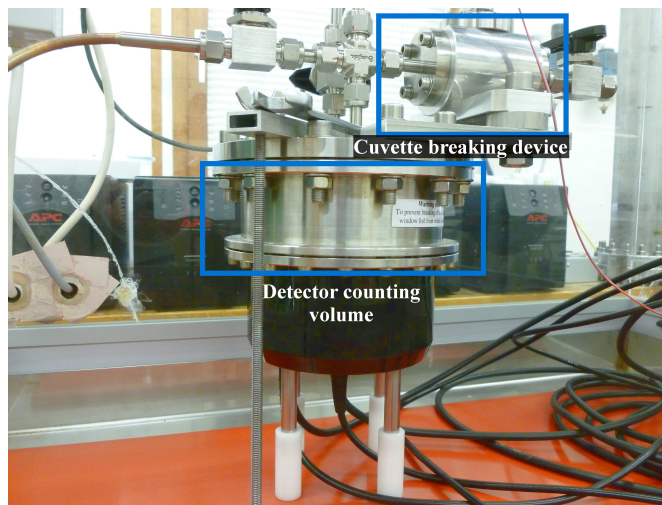


Figure 7.3.: The detector used for the tritium detection. It is filled with the measurement gas from the left side. The cylindrical shaped device to the top right destroys the glass cuvette mechanically. Thus the measurement gas comes into contact with the irradiated helium. After the measurement, the gas is flushed into a digestorium.

Figure 7.3 shows the detector. It was a cylindrical shaped chamber with an inner volume of  $540 \text{ cm}^3$ . The inner volume was filled with a mixture of 50:50 He to  $\text{CO}_2$ . The total pressure in the detector was 400 mbar. Thus, the irradiated helium within the cuvettes will not change the pressure in the detector drastically. The detector was operated at a voltage of 2600 V, where previous studies [Gre11, Wlo11] could prove a detection efficiency of more than 50 %.

Figure 7.4 shows a schematic layout of the detector setup. The detector was placed in a glove box, which was depressurized by 1.5 mbar to ensure that no contaminants can leave the detector setup. Three gases were used in the experiment. Helium and  $\text{CO}_2$  were used as counting gases and nitrogen was used to flush the detector after each measurement for cleaning purposes. The pipes, leading to the breaking armature for the cuvettes, were filled with sintered filters, so

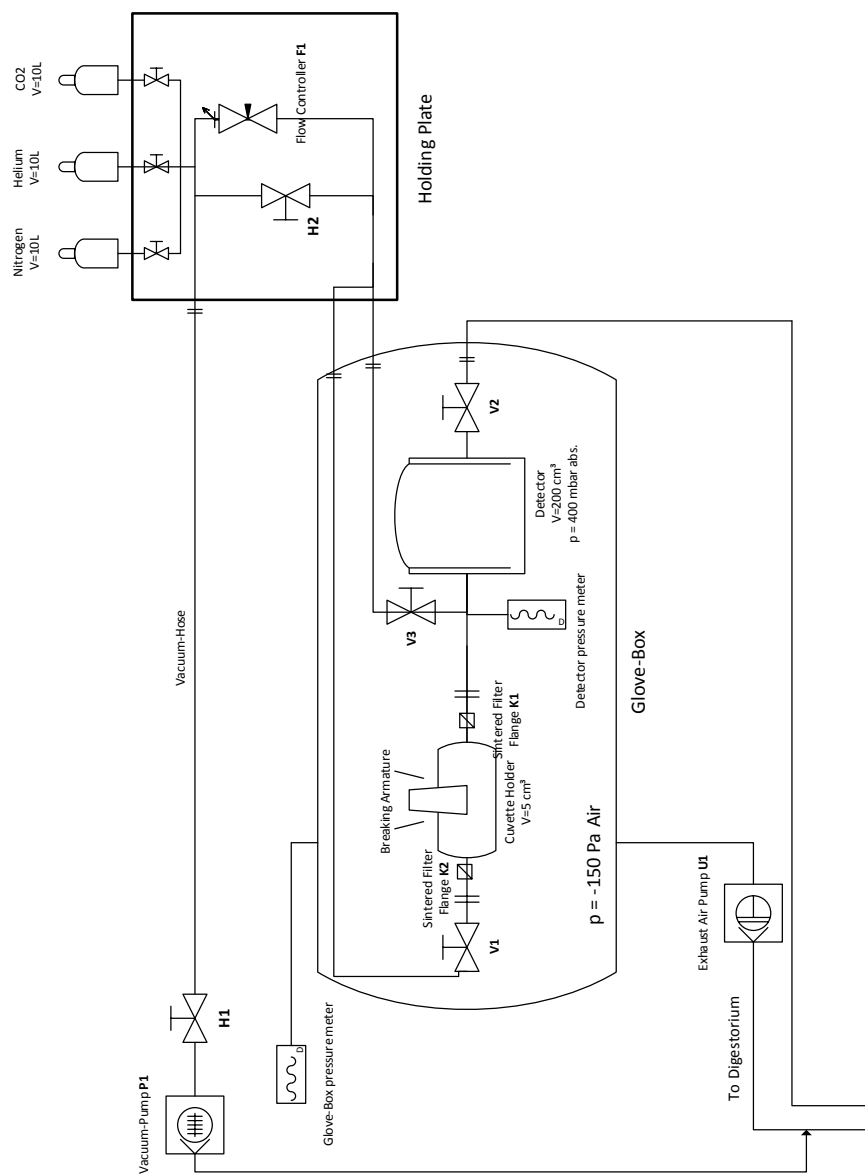


Figure 7.4.: Schematic layout of the detector setup. The detector was placed in an underpressurized glove box to ensure that no contamination can leak into the surroundings. The detector was filled with a 50:50 mixture of He and CO<sub>2</sub>. Nitrogen was used to clean the detector after a measurement.

that no broken glass could get into the detector. The pressure inside the detector was constantly monitored by a membrane pressure meter. All exhaust gases were led into the digestorium of the the radioprotection laboratory of the Physics Department of the Technical University of Munich (TUM).

After the detector was evacuated to pressures of  $< 10^{-3}$  mbar, the cuvette was destroyed, so that the irradiated gas could fill the detector volume. No increase in detector pressure could be detected at this stage. Next, the detector was filled with the measurement gas. Helium and CO<sub>2</sub> were filled in separately, one after another. The detector could then be ramped up to the nominal voltage of 2600 V and a spectrum could be taken. Every measurement was accompanied by a background measurement, where the procedures mentioned above were done without breaking the glass cuvette. After each measurement the detector gas was flushed into the digestorium with nitrogen with a flow rate of 100 sccm.

The primary signal of the detector was put into an Ortec Spectroscopy Amplifier Model 440A with a Coarse Gain of 4 and a fine gain of 1.8. The shaping time was set to 1  $\mu$ s. The shaped signal was then analysed by a Pocket MCA8000a by Amptek Inc., which then transmitted the pulse-height spectrum to a PC.

## 7.3. Results

### 7.3.1. Count rates

Unfortunately, after cleaning of the cuvettes, no assignment as to which cuvette held which gas was possible, since the labels were cleaned off. This meant, that the experiment was an actual double blind study to find the cuvettes holding the non-purified helium.

The first cuvette was measured with a defective detector, where no real Geiger signal could be observed. It is unclear, whether the cuvette was filled with standard helium or purified helium. The other three samples were measured with a working detector producing a clear Geiger signal. A typical spectrum is shown in fig. 7.5. The amplifier gain was set in such a way that the Geiger Peak appeared in the center of the spectrum. Events with a higher energy than the Geiger Peak belong to pile-up events. Particles, which do not have enough energy to trigger a Geiger event are seen with their correct energy, which is less than the full Geiger cascade and therefore appear on the left side of the spectrum.

For the actual analysis two windows of interest were defined. Since the events seen in the spectrum do not contain noise, the first window is simply the total spectrum itself. The second window was set around the Geiger Peak. The window began 200 channels below the peak maximum and ended 100 channels after the maximum. This accounted for the asymmetry of the peak.

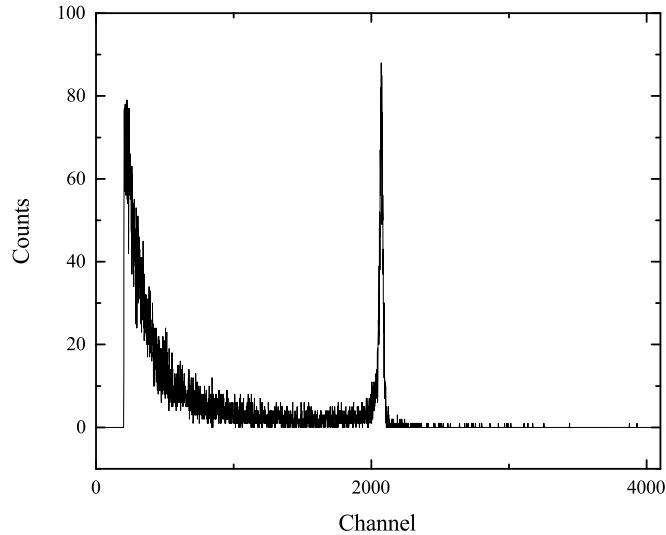


Figure 7.5.: Typical spectrum of the tritium detector at  $U = 2600$  V. The MCA threshold was set to 205. The peak around channel 2100 is the Geiger peak. Events with higher energy come from pile-up events. Beta particles with lower energy do not necessarily produce a Geiger event and are seen with fewer events producing the spectrum on the left half of the plot.

The results for the different cuvettes are summarized in table 7.1. The given uncertainties are  $3\sigma$  statistical uncertainties and a 4% systematic uncertainty, which was estimated by repeatedly measuring the background rate. This second uncertainty describes differences due to slight changes in the gas mixture, each time the detector is filled.

For two of the cuvettes a significant increase of the count rate was found. As it has already been seen in [Wlo11], after the detector measured tritium and is flushed with nitrogen, part of the activity still remains in the detector leading to an unwanted background. This background has to be measured prior to every measurement. This has not been done for cuvette no. 3, hence the measured rate for cuvette no. 2 was used as background with a 10% systematic uncertainty. By flushing the detector with nitrogen for several hours and evacuating the detector for several hours, the background can be brought back to its original values. Due to the limited time available in the laboratory of the radioprotection group of the Physics Department of the TUM, this has been done with shorter flushing times.

Table 7.1.: Measured count rates for the different cuvettes with statistical uncertainties.

Cuvette no.	Peak rate	Total rate	BG peak rate	BG total rate
1	–	–	–	–
2	$4.26 \pm 0.29$	$26.14 \pm 1.34$	$3.50 \pm 0.33$	$20.47 \pm 1.27$
3	$11.56 \pm 0.76$	$77.06 \pm 3.84$	$4.26 \pm 0.71$	$26.14 \pm 3.96$
4	$13.61 \pm 0.86$	$91.18 \pm 4.47$	$6.53 \pm 0.52$	$43.52 \pm 2.40$

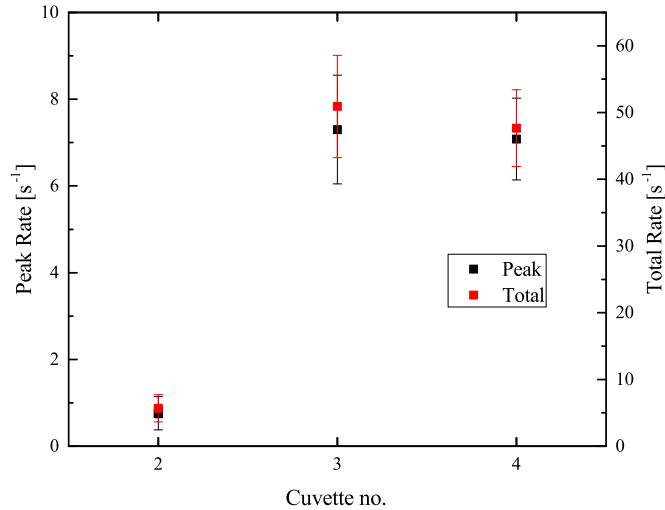


Figure 7.6.: Background subtracted count rates for the three measured cuvettes. The rate in the Geiger peak is shown on the left  $y$  axis, while the total rate in the spectrum is on the right axis. Two of the cuvettes clearly show an increase in activity. Within the uncertainty the increase is the same for the Geiger peak and the total spectrum. The increased rate in cuvette no. 2 can be attributed to detector drift.

### 7.3.2. Helium-3 content

Subtracting the background rates from the measured rates with the destroyed cuvettes yields the values for the activity of the irradiated helium. This is shown in fig. 7.6. Two of the three measured cuvettes show a clear indication of tritium content. In both cases the count rate is increased, i.e. by  $\approx 7 s^{-1}$  in the peak rate or  $\approx 50 s^{-1}$  in the total rate. In [Wlo11] it could be shown, that up to  $(72 \pm 2) \%$  of the tritium could be detected at a voltage of 2600 V. With this, an actual activity of  $(66 \pm 2 \pm 15) s^{-1}$  can be calculated. The systematic uncertainty of  $15 s^{-1}$  is estimated due to differences in the actual gas mixture used in this experiment and in [Wlo11]. The different gas mixtures lead to different gas amplifications, which cannot be estimated. Nevertheless, this value leads to a ratio  ${}^3\text{He}/{}^4\text{He} = (1.4 \pm 0.3) \cdot 10^{-7}$ , which is well in the range of commercially available gases. The increased uncertainty of cuvette no. 3 comes from the uncertainty of the background measurement, because the background was taken from the actual measurement of cuvette no. 2, as was explained before. An independent measurement of the actual helium-3 content of the bottled gas still needs to be done.

As can be seen in fig. 7.6, there is a small increase in the count rate for cuvette no. 2 of  $(0.76 \pm 0.05) s^{-1}$ . This is very likely not due to an actual tritium content in the irradiated helium, but rather due to a drift in the detector amplification. Figure 7.7 shows the spectrum for cuvette no. 2 together with the accompanying background spectrum. The actual cuvette measurement has been shifted by 28



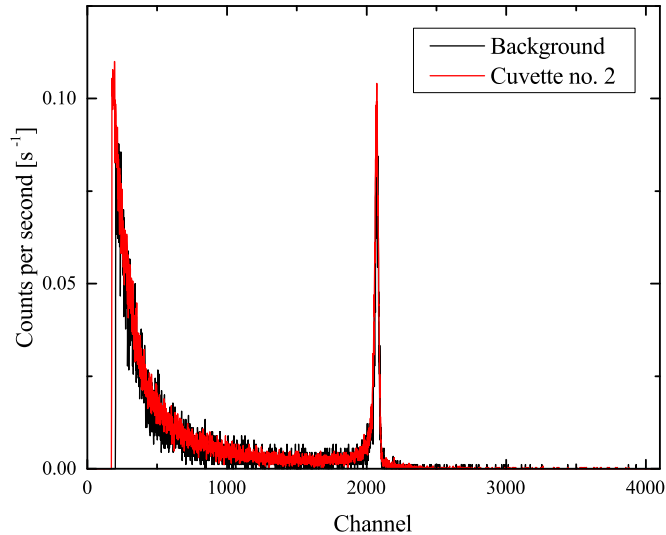


Figure 7.7.: Comparison of the background measurement and the actual measurement of cuvette no. 2. The cuvette measurement spectrum has been moved by 28 channels, so that the Geiger peaks coincide. It becomes clear, that the shape of the two spectra is the same. There are no excess counts in the general spectrum. The Geiger peak is enhanced by 17%, due to detector drift, which leads to an an increased gas amplification, where the threshold for a Geiger event is lowered.

channels, so that the Geiger peaks coincide. The shape of the two spectra is almost identical. The shift in the position of the peak and the 17% increase in peak count rate can both be attributed to a drift in the detector amplification.

### 7.3.3. Background rates

After the different cuvettes were measured, it was noticed that the background rate was elevated, even after flushing the detector with nitrogen for several hours. Fig. 7.8 shows the count rates for 90 consecutive measurements with a measurement time of 1 h. The gas shows an ageing effect. The total count rate drops by almost 20% during the 90 h. The slope of the peak rate and the total rate is different, which indicates that the gas amplification also changes with time. The effect, that the count rate and the peak/total rate ratio are linked, has already been investigated in [Wlo11]. By emptying and refilling the detector with the counting gas, the background count rate can be restored to its original values.

From fig. 7.8 it can also be observed, that for the first few hours the count rate remains rather stable. By averaging the first 10 h, a uncertainty of  $0.1 \text{ s}^{-1}$  for the peak rate and  $0.4 \text{ s}^{-1}$  for the total rate can be extracted. By not changing the gas between the background measurement and the actual tritium measurement, i.e. breaking the cuvette only when the counting gas is already inside, one could

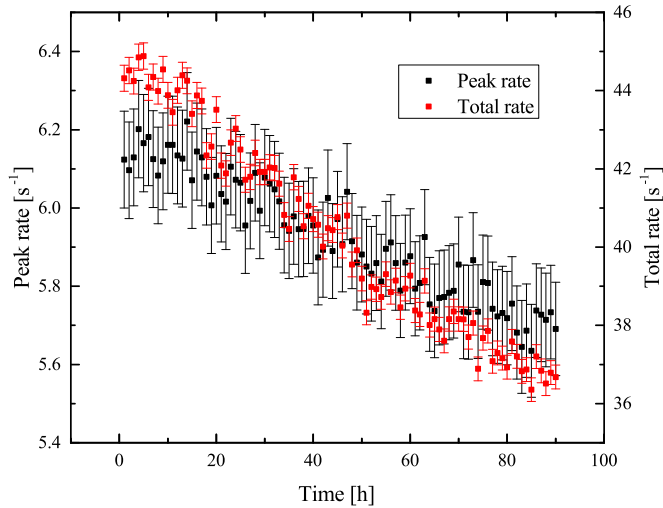


Figure 7.8.: The background count rate in the detector after measuring the cuvettes. Each data point was measured for 1 hour. The counting gas shows an ageing effect, where the count rate continuously drops. After refilling the detector with new gas, the count rate is restored. A slight difference in the slope of the peak rate and the total rate can be observed.

significantly reduce the total uncertainty. A bypass would have to be installed, so that the irradiated gas does not have to pass through the sintered filters, so that it reaches the counting volume quicker.

### 7.3.4. Helium purity and limit of the method

With the values determined above, it is now possible to calculate limits for the helium-3 content of the purified helium samples. This, of course, assumes that cuvette no. 2 contained the purified helium while the other two cuvettes contained normal helium from a gas bottle. By simply calculating the ratio of the count rate for cuvette no. 2 and the other cuvettes and then calculating the weighted mean, one can come up with  $^3\text{He}$  suppression of

$$\gamma_{^3\text{He}} = 0.111 \pm 0.031. \quad (7.5)$$

This means, that the helium-3 content in the purified sample was a factor of 9 smaller than in the bottle helium samples. Using the  $^3\text{He}/^4\text{He}$  ratio estimated above, one can now calculate a ratio of  $^3\text{He}/^4\text{He} = (1.6 \pm 0.8) \cdot 10^{-8}$ .

For cuvette no. 2 it is also possible to calculate the count rate differently by using the corrected spectrum from fig. 7.7. With this, the total rate in the detector is

reduced to  $(2.78 \pm 0.28) \text{ s}^{-1}$ . This also reduces the  $^3\text{He}$  suppression to a value of  $0.057 \pm 0.009$ .

In [Wlo11] the tritium detector was tested up to activities of 3 kBq. Using that value together with the lowest experimental uncertainty for the total rate of  $0.28 \text{ s}^{-1}$  a limit for the detectable suppression can be calculated.

$$\gamma_{\text{lim}} \approx 10^{-4} \tag{7.6}$$

Assuming that industrial grade helium has a helium-3 content of  $3 \cdot 10^{-7}$ , the upper limit for a purified helium sample is  $^3\text{He}/^4\text{He} < 3 \cdot 10^{-11}$ . This is several orders of magnitude better, than what is needed for the UCN source at the FRM II. In order to irradiate a sample with industrial grade helium to activities of 3 kBq an irradiation duration of  $\sim 2$  days is needed at the KBA-1.1 facility of the FRM II.

It becomes clear, that the experiment needs to be repeated with longer irradiation times and a more careful execution. It is of special importance to determine the background rate accurately. The background rate should be determined over the course of several hours. The detector should be enhanced in such a way, that the cuvette can be destroyed, when the counting gas is already inside. A bypass for the sintered filters is then needed, so that the irradiated gas can mix easily with the counting gas. After each measured cuvette, the detector should be flushed with nitrogen for several hours and pumped to a vacuum of  $< 10^{-4}$  mbar to ensure a minimum of residual background from previous measurements.

Nevertheless, it could be shown that the detector tested here, is capable to determine small fractions of tritium and thus helium-3, with ratios of  $^3\text{He}/^4\text{He} < 10^{-9}$ , which is needed for the operation of the UCN source at the FRM II.



# Chapter 8.

## Conclusion

---

Ultra-cold neutrons are excellent probes for fundamental physics due to their unique properties. The determination of an electric dipole moment or the neutron lifetime are fundamental tests for the standard model. Currently all experiments are limited due to statistics, which is why new strong sources for UCN are necessary.

Over the last decade several new sources went into operation, like the Los Alamos UCN source [Sau13], the PSI UCN source [Lau11] or the SUN source at the ILL [Zim15]. All these sources are based on the “superthermal” production process [Gol75]. However, only the SUN source could so far surpass the ILL turbine regarding its achieved UCN density. Newer and stronger sources are already under construction [Mar08].

The new source for ultra-cold neutrons at the Forschungs-Neutronenquelle Heinz Maier-Leinbitz (FRM II) will be among the strongest sources with an estimated UCN density of  $\sim 5 \cdot 10^3 \text{ cm}^{-3}$  [Fre13]. The source will use deuterium as its converter material. Deuterium, as any other superthermal converter material, hardly moderates the neutrons through elastic collision processes. Solid-state excitations, e.g. phonons, take almost all of the energy from the neutrons in a single scattering process. Once the UCN are produced, there are a number of loss mechanisms already within the converter. Absorption and upscattering losses have to be minimized in order to effectively extract the neutrons towards the experiments. For the deuterium a temperature of 5 K is needed to bring the upscattering rate of phonons to the same level as the absorption rate.

Deuterium, like all the homonuclear, diatomic molecules, comes in two quantum-states. Since the higher-energetic “para” state lies 7 meV above the ground “ortho” state, one needs to make sure, that the para content of the deuterium is minimal, so that upscattering on the para molecules is minimized. Previous studies have shown [Liu00] that a para fraction of less than 2 % is needed to reduce the losses on para deuterium to an acceptable level.

Once the neutrons leave the deuterium, they have to be guided to the experiments.

In the FRM II UCN source the neutrons first have to travel a distance of  $\sim 8$  m before they reach the exit of the source in the experimental hall. This distance has to be passed with minimal losses. Standard ultra-cold neutron guides, made by coating a reflective surface onto a glass tube, cannot be used in a high radiation environment like the beam tube SR6 of the FRM II. The UCN source will rather rely on newly developed “Replika”-type guides, where a Nickel-Vanadium alloy is sputtered onto a flat glass surface. The sputtered material is then loosened from the glass and rolled to a guide. These new guides can easily withstand the radiation doses occurring near the reactor fuel element.

The following results were obtained during the course of this work.

- A experimental area to irradiate cryo-crystals down to 7 K with protons with energies up to 23 MeV has been built at the Maier-Leibnitz-Laboratory (MLL). The ortho/para ratio could be monitored with a Raman spectrometer. The optics, which bring the laser light to the crystal and the Raman light to the spectrometer have also been developed during this work.
- Two experiments have been conducted to determine the radiation-assisted ortho conversion parameters of solid deuterium. One experiment was conducted at 7.8K, the other one at 10.3K. A strong dependence of the conversion parameter  $\beta$  on the temperature of the crystal has been found. At 7.8K a value of  $\beta = (8.5 \pm 4.0) \cdot 10^{-25} \text{ cm}^3\text{s}^{-1}$  was determined and at 10.3K  $\beta = (1.2 \pm 0.6) \cdot 10^{-23} \text{ cm}^3\text{s}^{-1}$ .
- A theoretical model has been employed to analyse the data. It has been found that the diffusion parameter  $t_0$  has to be decreased by 2 orders of magnitude, compared to estimates by Collins et al. [Col91], in order to explain the experimental results. With this, it was possible to calculate the  $t \rightarrow \infty$  ortho fraction during irradiation at the FRM II. Further experiments are needed at different temperatures in order to confirm the model.
- The diffuse reflectivity of Replika guides has been measured at the PF2/TES beam line of the ILL. Together with a GEANT4 simulation, it was possible to create a consistent description of the UCN propagation through the guide. The model uses an altered lambertian reflection mechanism, which proved to describe the data very well. A diffuse reflection probability of  $d = (3.0 \pm 0.5) \cdot 10^{-2}$  was determined. This is the first time that an experiment is able to describe the diffuse reflectivity of different guide lengths of the same type with a single set of parameters.
- A method for the determination of the  $^3\text{He}$  content in a helium sample was tested. The helium was first irradiated at the FRM II reactor, so that part of the helium-3 converts to tritium via neutron absorption. Glass cuvettes were used to contain the helium during irradiation. Afterwards the cuvettes were inserted in a single wire chamber, where the cuvettes were destroyed and the tritium activity was measured. Two different helium samples were

measured, a standard sample from a gas bottle, and a purified helium sample from Lancaster University [Hen87]. The working principle of the method could be proven. A reduction of the  $^3\text{He}$  by a factor of 9 could be shown directly. It was also estimated, that by redoing the experiment with longer irradiation times and longer measurement times for the tritium,  $^3\text{He}$  content of less than  $10^{-10}$  can be measured.

The experimental results were compared with literature and other models. For the production and extraction of the UCN out of the deuterium converter, it could be shown, that no anomalous losses, due to a para deuterium enhancement during irradiation, are to be expected. Up to a temperature of 10 K the ortho content will stay well above 0.99. For the guide system, which is needed for the transport to the SR6 beam tube exit, a Replika type guide has been developed, which can transport  $(0.99 \pm 0.006) \text{ m}^{-1}$  of the UCN. This is mainly because of the low surface roughness of the material, which lowers the probability for diffuse reflection on the surface of the guide. Together, this means that the UCN source will have the output strength that has already been calculated in [Fre08], which will surpass all previously built sources by at least one order of magnitude.

Two major experiments are planned for the UCN source at the FRM II: The determination of the lifetime and the electric dipole moment of the free neutron. While the lifetime experiment will still take several years before the final operation can start, the EDM experiment is becoming ready for production runs. The equipment is currently being tested at the Institut Laue-Langevin (ILL) in Grenoble. The outer magnetic shielding and a magnetically shielded room are already in place in the neutron guide hall east of the FRM II. The UCN source will also have two additional experimental areas, one in the experimental hall, and another one in the guide hall east. Those areas are foreseen for short term experiments and experimental time will be distributed in a proposal round system.

Currently all components of the new UCN source are being tested at the Maier-Leibnitz Laboratory (MLL) in Munich. For the next year the complete setup of the source will be tested non-nuclearly. All operational parameters will be known before the actual operation in the FRM II. After the successful tests, the equipment will be brought to the FRM II and installed there. The start of the source is planned for 2018 and regular user operation can start in 2019.





# Appendix A.

## Raman spectroscopy

---

### A.1. The Raman effect

The Raman effect was first discovered by C.V. Raman and K.S. Krishnan in 1928 [Ram28]. Since then it has become one of the most powerful tools to investigate the structure of solids as well as the molecular structure of liquids and gases. Typically high power laser light sources are used for Raman spectroscopy. The photons interact either with a molecule itself or with the solid state lattice. In either case energy and momentum conservation is fulfilled.

$$\begin{aligned}\hbar\omega_{\text{ex}} &= \hbar\omega_{\text{ph},f} - \hbar\omega_{\text{ph},i} \\ \hbar Q_{\text{ex}} &= \frac{2\pi\hbar}{\lambda_{\text{ph},f}} - \frac{2\pi\hbar}{\lambda_{\text{ph},i}}\end{aligned}\tag{A.1}$$

Here,  $\omega_{\text{ex}}$  and  $\hbar Q_{\text{ex}}$  are the frequency and lattice vector of an excitation.  $\omega_{\text{ph},i/f}$  are the initial and final frequencies of the light and  $\lambda_{\text{ph},i/f}$  are the corresponding wavelength.

Molecules can be excited to (virtual) energy states by the incoming laser light. Subsequently the molecule will de-excite to either its previous energy state, which is called Rayleigh scattering, or a different energy level, which is called Raman scattering. For the latter type, two outcomes are possible. The de-excited state can have more energy than the initial state, so that the re-emitted light has less energy (Stokes Raman scattering) or the final state can be a lower energetic state (Anti-Stokes Raman scattering). When scattering on a lattice the excitation can be any excitation fulfilling eq. A.1, i.e. phonons, magnons, etc. A single molecule can have its vibrational or rotational state changed by the incoming light.

The frequency change of the Raman scattered light is independent of the frequency of the incoming light. The so-called Raman spectrum shows the intensity of the scattered light as a function of the frequency change  $\Delta\nu$ . The measurement

of the energy levels can give information on the population of the different energy levels or the energy levels themselves. In order to avoid confusion, when determining the different energy levels, single-mode lasers are most commonly used for Raman spectroscopy. The intensity of the Rayleigh scattered light is many orders of magnitude bigger, than for the Raman light. In order to detect very small Raman shifts ( $< 100 \text{ cm}^{-1}$ ) it is often helpful to use a Raman spectrometer with a subtractive mode, which can block the unwanted Rayleigh light, while letting the Raman light pass.

## A.2. Molecular energy levels in hydrogen

The energy levels of a diatomic molecule with vibrational and rotational degrees of freedom can be expressed as

$$E_{\text{tot}}(v, J) = E_{\text{vib}}(v) + E_{\text{rot}}(v, J), \quad (\text{A.2})$$

where  $v$  is the vibrational quantum number and  $J$  is the rotational quantum number.  $E_{\text{vib}}$  can be expressed as [Sou86]

$$E_{\text{vib}}(v) = \hbar \left[ v_e \left( v + \frac{1}{2} \right) + x_e \left( v + \frac{1}{2} \right)^2 + y_e \left( v + \frac{1}{2} \right)^3 \right], \quad (\text{A.3})$$

where  $v_e$ ,  $x_e$  and  $y_e$  are vibrational spectroscopic constants [Sou86]. Often, the vibrational energy is defined as the difference between  $E_{\text{vib}}$  and the zero-point energy  $E_{\text{vib}}(0)$ .

The rotational energy can be written as [Sou86]

$$E_{\text{rot}}(v, J) = B_v J(J+1) + D_v J^2(J+1)^2 \quad (\text{A.4})$$

$B_v$  and  $D_v$  are the rotational and centrifugal distortion constants. They both depend on  $v$  and are given by

$$B_v = B_e - \alpha_e \left( v + \frac{1}{2} \right) \quad (\text{A.5})$$

$$D_v = D_e + \beta_e \left( v + \frac{1}{2} \right), \quad (\text{A.6})$$

where  $B_e$ ,  $D_e$ ,  $\alpha_e$  and  $\beta_e$  are empirical constants. Details about the different coefficients and empirical values can be found in [Lon01, Sou86, VK60, VK83].

### A.3. Occupation of the different levels

As is the case for any system with different energy levels, the population of the hydrogen energy levels follows a Boltzmann distribution. The different levels have to be weighted though, with nuclear spin degeneracy  $g_J$ , which is 3 for odd values and 6 for even values of  $J$ .

$$P(v, J) = \frac{g_J (2J + 1) e^{-E_{\text{tot}}(v, J)/T}}{Z} \quad (\text{A.7})$$

Here,  $Z$  is the partition function, which can be written as

$$Z = \sum_{v=0}^{\infty} \sum_{J=0}^{\infty} g_J (2J + 1) e^{-E_{\text{tot}}(v, J)/T}. \quad (\text{A.8})$$



# Appendix B.

## Data analysis

---

### B.1. Raman intensities

The intensities of each Raman line in deuterium or hydrogen can be written in the following way

$$I(J \rightarrow J + 2) \propto \frac{B_{J,J+2} c_{o/p} (\omega - \omega_{0 \rightarrow 2})^2 P(0, J)}{Z_J / Z}. \quad (\text{B.1})$$

Here,  $c_{o/p}$  is the ortho or para content depending on whether  $J$  is even or odd,  $\omega$  is the incoming light frequency,  $\omega_{0 \rightarrow 2}$  is the frequency shift due to the excitation and  $Z_J$  is the fractional partition function, which only runs over the even or odd terms, depending on whether  $J$  is even or odd. The value  $B_{j,j+2}$  is the so-called Placzek-Teller coefficient [Pla33], which describes the different coupling strength of the photons to the different rotational quantum numbers and can be calculated with [Pla33, Mis04]

$$B_{j,j+2} = \frac{3(j+1)(j+2)}{2(2j+1)(2j+3)}. \quad (\text{B.2})$$

In the Raman experiments in this work, only intensity ratios of the  $J = 0 \rightarrow 2$  and  $J = 1 \rightarrow 3$  Raman lines are used

$$R = \kappa^{-1} \frac{I(0 \rightarrow 2)}{I(1 \rightarrow 3)}. \quad (\text{B.3})$$

The ratio  $R$  is then used to calculate the ortho/para ratio  $c_o$ . The correction factor  $\kappa$  includes the differences in the actual Raman cross-sections of the lines. However,

those differences are small, since the wavelength differences are  $< 10$  nm [Lon01]. The factor  $\kappa$  also combines all differences in the transport efficiency through the optical system for the lines. It has to be fixed by measuring the Raman intensities of hydrogen or deuterium with a known ortho/para ratio.

## B.2. The Voigt function

The Voigt function is often used in spectroscopy and diffraction. It is the convolution of a Gauss function and a Lorentz function.

$$V(x) = G(x) \circ L(x) \quad (\text{B.4})$$

Due to this property, it combines the broadening mechanisms of both functions. In atmospheric spectroscopy the Voigt function is used, because it describes the pressure broadening and doppler broadening accurately. In the case of the Raman spectroscopy on solid deuterium used in this work, it describes the broadening due to the light travelling through the crystal, the broadening of the optical system, and the broadening within the spectrometer, which is comprised mostly of the slit entrance function.

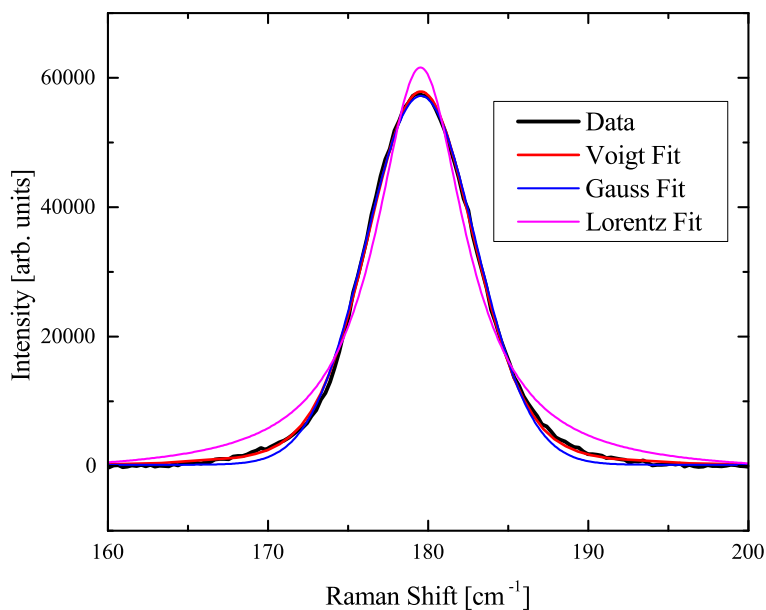


Figure B.1.: Comparison of different fitting functions. The Voigt function describes the data best. While the Gauss fit does describe the peak itself well, it fails to reproduce the edges. On the other hand, the Lorentz curve is not suited to describe the data.

Figure B.1 shows a comparison of the three different fitting functions, Gauss, Lorentz and Voigt, when fitting a typical Raman peak. While the Lorentz function is not suitable to describe the experimental data, the Gauss fit already fits well to the most part of the peak. However, it does not describe well the edges of the peak, which are broadened compared to the single Gauss curve. The Voigt function accurately describes all parts of the data. As can be seen in the figure, the peaks fit curve is mostly comprised of a gaussian portion, and a small (10 – 15 %) portion of the Lorentz curve adds to the broadened edges. Origin Pro 9.1 was used to fit the data. The fit function is

$$y_0 + A \frac{2 \ln 2}{\pi^{3/2}} \frac{w_L}{w_G^2} \int_{-\infty}^{\infty} \frac{e^{-t^2}}{\left(\sqrt{\ln 2} \frac{w_L}{w_G}\right)^2 + \left(\sqrt{4 \ln 2} \frac{x-x_c}{w_G} - t\right)^2} dt. \quad (\text{B.5})$$

The values  $w_L$  and  $w_G$  describe the full widths at half maximum of the Lorentz and Gauss function,  $y_0$  is the baseline value,  $A$  is the area under the curve and  $x_c$  is the center value of the curve. The total FWHM is calculated by Origin Pro using

$$\text{FWHM} = 0.5346 w_L + \sqrt{0.2166 w_L^2 + w_G^2}. \quad (\text{B.6})$$

### B.3. Determination of the correction factors

In order to determine the correction factor  $\kappa$ , which is used to correct for the different light transmissions efficiencies for the Raman lines, a sample with a known ortho-concentration has to be measured first. In this work, for every configuration of the optics system, a deuterium crystal was frozen using gas from a bottle. It was assumed, that at the time of liquefaction, the deuterium had a natural ortho content  $c_o = 2/3$ . A series of 5 to 10 measurements on the solid at the same temperature as the later irradiation measurement temperature was done. The value  $c_o$  was assumed to change slightly according to [Sou86] with a characteristic time  $\tau = 1900$  h. The correction factor  $\kappa$  could then be calculated.

$$\kappa = f \frac{(1 - c_o) S(0 \rightarrow 2)}{c_o S(1 \rightarrow 2)} \quad (\text{B.7})$$

Here,  $S(i \rightarrow f)$  describe the intensity of the measured Raman lines. The pre-factor  $f$  is almost independent of temperature for hydrogen or deuterium below 20 K.

For deuterium  $f = 1.699$ , while for hydrogen  $f = 1.731$ . For the ortho/para ratio, one can then write

$$c_o = \kappa^{-1} \frac{S(0 \rightarrow 2)}{S(1 \rightarrow 2)} \left( f + \kappa^{-1} \frac{S(0 \rightarrow 2)}{S(1 \rightarrow 2)} \right)^{-1} = \frac{R}{f + R}. \quad (\text{B.8})$$



# Bibliography

---

- [Abe10] H. Abele, T. Jenke, H. Leeb and J. Schmiedmayer. *Physical Review D*, **81** (2010)
- [Abe11] H. Abele, G. Cronenberg, P. Geltenbort, T. Jenke, T. Lins and H. Saul. *Physics Procedia*, **17**, 4 (2011)
- [Ago03] S. Agostinelli et al. *Nucl. Instr. Meth. A*, **506**, 250 (2003)
- [AH98] N. Arkani-Hamed, S. Dimopoulos and G. Dvali. *Phys. Lett. B*, **429**, 263 (1998)
- [Alt10] I. Altarev et al. *Nucl. Phys. A*, **844**, 47c (2010)
- [Ang09] A. Anghel et al. *Nucl. Instr. Meth. A*, **611**, 272 (2009)
- [Atc03] F. Atchison et al. *Phys. Rev. B*, **68** (2003)
- [Atc09] F. Atchison et al. *Nucl. Instr. Meth. A*, **608**, 144 (2009)
- [Atc10] F. Atchison et al. *Eur. Phys. J. A*, **44**, 23 (2010)
- [Bae08] S. Baeßler et al. *Eur. Phys. J. A*, **38**, 17 (2008)
- [Bak06] C. A. Baker et al. *Phys. Rev. Lett.*, **97** (2006)
- [Bec64] K. Beckurts and K. Wirtz. *Neutron Physics* (Springer Verlag, 1964)
- [Ber05] M. Berger, J. Coursey, M. Zucker and J. Chang. ESTAR, PSTAR, and ASTAR: Computer Programs for Calculating Stopping-Power and Range Tables for Electrons, Protons, and Helium Ions (version 1.2.3). [Online] Available: <http://physics.nist.gov/Star> [2015, 12 02]. National Institute of Standards and Technology, Gaithersburg, MD. (2005)
- [Bha62] S. Bhatnagar, E. Allin and H. Welsh. *Can. J. Phys.*, **40**, 9 (1962)
- [Bon09] D. Bondoux et al. *Nucl. Instr. Meth. A*, **606**, 637 (2009)
- [Bro83] R. L. Brooks, M. A. Selen, J. L. Hunt, J. R. MacDonald, J. D. Poll and J. C. Waddington. *Phys. Rev. Lett.*, **51**, 1077 (1983)
- [Bro85] R. L. Brooks, S. Bose, J. L. Hunt, J. R. MacDonald and J. D. Poll. *Phys. Rev. B*, **32**, 2478 (1985)

- [Bry07] T. Bryś. *Extraction of ultracold neutrons from a Solid Deuterium Source*. Dissertation. ETH Zürich (2007)
- [Cah90] D. G. Cahill. *Rev. Sci. Instrum.*, **61**, 802 (1990)
- [Car87] J. M. Carpenter. *Nature*, **330**, 358 (1987)
- [Col91] G. W. Collins, E. M. Fearon, E. R. Mapoles, R. T. Tsugawa, P. C. Souers and P. A. Fedders. *Phys. Rev. B*, **44**, 6598 (1991)
- [Dau12] M. Daum et al. *Nucl. Instr. Meth. A*, **675**, 103 (2012)
- [Dia85] V. Diatschenko, C. W. Chu, D. H. Liebenberg, D. A. Young, M. Ross and R. L. Mills. *Phys. Rev. B*, **32**, 381 (1985)
- [Dic65] S. A. Dickson and H. Meyer. *Phys. Rev.*, **138**, A1293 (1965)
- [Dub08] D. Dubbers, H. Abele, S. Baefler, B. Märkisch, M. Schumann, T. Soldner and O. Zimmer. *Nucl. Instr. Meth. A*, **596**, 238 (2008)
- [Ebn72] C. Ebner and C. Sung. *Phys. Rev. A*, **5**, 2625 (1972)
- [Fer36] E. Fermi. *Ricerca Scientifica*, **7**, 13 (1936)
- [For94] J. Forrest, R. L. Brooks and J. L. Hunt. *Phys. Rev. B*, **50**, 9573 (1994)
- [For97] J. Forrest and R. L. Brooks. *Phys. Rev. B*, **55**, 906 (1997)
- [Fre07] A. Frei et al. *Eur. Phys. J. A*, **34**, 119 (2007)
- [Fre08] A. Frei. *Produktion von ultrakalten Neutronen mit einem festen Deuteriumkonverter*. Dissertation. Physics Department E18, Technical University of Munich (2008)
- [Fre09] A. Frei, E. Gutmiedl, C. Morkel, A. Müller, S. Paul, M. Urban, H. Schober, S. Rols, T. Unruh and M. Hölzel. *Phys. Rev. B*, **80** (2009)
- [Fre10] A. Frei, K. Schreckenbach, B. Franke, F. J. Hartmann, T. Huber, R. Picker, S. Paul and P. Geltenbort. *Nucl. Instr. Meth. A*, **612**, 349 (2010)
- [Fre11] A. Frei. Berechnung der erwarteten Tritium-Aktivität bei der geplanten UCN-Quelle im SR6 am FRM II. Tech. rep. Forschungs-Neutronenquelle Heinz Maier-Leibnitz (FRM II), OPA00375, Techn. Univ. München (2011)
- [Fre13] A. Frei. UCN density calculations for the new UCN source at the FRM II. Internal Report, Forschungs-Neutronenquelle Heinz Maier-Leibnitz (FRM II), Technical University of Munich (2013)
- [Fre14] A. Frei. UCN Quelle (im Aufbau). <http://www.mlz-garching.de/instrumente/teilchenphysik/ucn.html> (2014)
- [Gil34] N. Gilbert and W. Hanson. *J. Am. Chem. Soc.*, **56**, 1687 (1934)

## Bibliography

- [Gol75] R. Golub and J. Pendlebury. Phys. Lett. A, **53**, 133 (1975)
- [Gol91] R. Golub, D. Richardson and S. Lamoreaux. *Ultra-Cold Neutrons* (Adam Hilger, Bristol, Philadelphia and New York, 1991)
- [Gra12] R. Q. Gram, A. She, R. S. Craxton and D. R. Harding. J. Appl. Phys., **112**, 033504 (2012)
- [Gre11] T. Greese. *Characterization of a Tritium Detector*. Bachelor thesis, Physics Department E18, Technical University of Munich (2011)
- [Gro71] I. Groshev, V. Dvoretzky, A. Demidov, Y. Panin, V. Lushchikov, Y. Pokotilovsky, A. Strelkov and F. Shapiro. Phys. Lett., **34B**, 293 (1971)
- [Hei15] K. Heinemann. *Charakterisierung von festem Deuterium mittels Raman Spektroskopie*. Bachelor Thesis, Physics Department E18, Technical University of Munich (2015)
- [Hen87] P. Hendry and P. McClintock. Cryogenics, **27**, 131 (1987)
- [Hog51] H. Hoge and R. Arnold. Journal of Research of the National Bureau of Standards, **47**, 63 (1951)
- [Hol02] D. Hollenbeck and C. Cantrell. J. Opt. Soc. Am. B, **19**, 2886 (2002)
- [Hub11] T. Huber. *Transport and Storage of Ultra-Cold Neutrons in Replika-Guides*. Diploma Thesis, Physics Department E18, Technische Universität München (2011)
- [Ign96] V. Ignatovich. Physics - Uspekhi, **39**, 283 (1996)
- [Isk86] A. Iskovskikh, A. Y. Katunin, I. Lukashevich, V. V. Sklyarevskii, V. V. Suraev, V. V. Filippov, N. I. Filippov and V. A. Shevtsov. Sov. Phys. JETP, **64**, 1085 (1986)
- [Jac57] J. D. Jackson, S. B. Treiman and H. W. Wyld. Phys. Rev., **106**, 517 (1957)
- [Jen80] J. Jensen, W. Tuttle, R. Stewart, H. Brechna and A. Prodel. *Brookhaven National Laboratory Selected Cryogenic Data Notebook* (Brookhaven National Laboratory Associated Universities, Inc., 1980)
- [Jen86] D. Jennings, A. Weber and J. Brault. Applied Optics, **25**, 284 (1986)
- [Job94] Jobin Yvon / Horiba GmbH. T64000 Manual. Tech. rep. (1994)
- [Kes99] E. Kessler, M. Dewey, R. Deslattes, A. Henins, H. Börner, M. Jentschel, C. Doll and H. Lehmann. Phys. Lett. A, **255** (1999)
- [Kle14] M. Klein. CASCADE. <http://www.physi.uni-heidelberg.de/Forschung/ANP/Cascade/> (2014)
- [Kor07] E. Korobkina, B. W. Wehring, A. I. Hawari, A. R. Young, P. R. Huffman, R. Golub, Y. Xu and G. Palmquist. Nucl. Instr. Meth. A, **579**, 530 (2007)

- [Kru78] I. Krupskii, S. Kovalenko and N. Krainyukova. *Sov. J. Low Temp. Phys.*, **4**, 564 (1978)
- [Lau11] B. Lauss. *Journal of Physics: Conference Series*, **312**, 052005 (2011)
- [Liu00] C. Y. Liu, A. Young and S. Lamoreaux. *Phys. Rev. B*, **62** (2000)
- [Liu08] C.-Y. Liu and A. Young. Ultra-cold Neutron Production in Antiferromagnetic Oxygen Solid. arXiv:nucl-th/0406004v1 (2008)
- [Lon01] D. A. Long. *The Raman Effect* (John Wiley & Sons, Bradford, 2001)
- [Luc00] L. Lucas and M. Unterweger. *J. Res. Natl. Inst. Stand. Technol.*, **105**, 541 (2000)
- [Mam89] W. Mampe, P. Ageron, C. Bates, J. Pendlebury and A. Steyerl. *Phys. Rev. Lett.*, **63**, 593 (1989)
- [Mar08] J. Martin et al. TRIUMF Ultracold Neutron Source. Tech. rep., TRIUMF Vancouver, BC (2008)
- [Mat09] S. Materne, R. Picker, I. Altarev, H. Angerer, B. Franke, E. Gutmiedl, F. J. Hartmann, A. R. Müller, S. Paul and R. Stoepler. *Nucl. Instr. Meth. A*, **611**, 176 (2009)
- [Men13] M. P. Mendenhall et al. *Phys. Rev. C*, **87** (2013)
- [Mil75] Y. Milenko and R. Sibileva. *Soviet J. Low Temp. Phys.*, **1**, 382 (1975)
- [Mis04] K. Mishima. *Irradiation Effect on Ortho Deuterium for UCN Source*. Dissertation. Research Center for Nuclear Physics (RCNP), Osaka University (2004)
- [Mor15] C. Morkel. Personal Communication (2015)
- [Mot56] K. Motizuki. *J. Phys. Soc. Jpn.*, **12**, 163 (1956)
- [Mä09] B. Märkisch, H. Abele, D. Dubbers, F. Friedl, A. Kaplan, H. Mest, M. Schumann, T. Soldner and D. Wilkin. *Nucl. Instr. Meth. A*, **611**, 216 (2009)
- [Nes02] V. V. Nesvizhevsky et al. *Nature*, **415**, 297 (2002)
- [Nev80] L. Nevot and P. Groce. *Rev. Phys. Appl.*, **15**, 761 (1980)
- [Nie71] M. Nielsen and H. Møller. *Phys. Rev. B*, **3**, 4383 (1971)
- [Oli14] K. A. Olive et al. *Chin. Phys. C*, **38**, 090001 (2014)
- [Par67] J. H. Parker, D. W. Feldman and M. Ashkin. *Phys. Rev.*, **155**, 712 (1967)
- [Pfi14] N. Pfifferling. *Simulation der thermischen und mechanischen Belastung eines Doppelrohrs der UCN-Quelle am FRM II*. Bachelor thesis, Physics Department E18, Technical University of Munich (2014)

## Bibliography

- [Pic05] R. Picker, I. Altarev, J. Bröcker, E. Gutschiedl, J. Hartmann, A. Müller, S. Paul, W. Schott, U. Trinks and O. Zimmer. *J. Res. Natl. Inst. Stand. Technol.*, **110**, 357 (2005)
- [Pla33] G. Placzek and E. Teller. *Zeitschrift f. Physik*, **81**, 209 (1933)
- [Plo07] C. Plonka, P. Geltenbort, T. Soldner and H. Häse. *Nucl. Instr. Meth. A*, **578**, 450 (2007)
- [Pyn92] R. Pynn. *Phys. Rev. B*, **45**, 602 (1992)
- [Ram28] C. Raman. *Indian J. Phys.*, **2**, 387 (1928)
- [Rie13] D. Ries. Status of the source for ultra-cold neutrons at the Paul Scherrer Institute. Tech. rep., Paul Scherrer Institute (2013)
- [Ros76] G. Rosen. *J. Chem. Phys.*, **65**, 1735 (1976)
- [Rö09] A. Röhrmoser. Ultrakalte n-Quelle (UCN) im Strahlrohr SR-6 des FRM II. Forschungs-Neutronenquelle Heinz Maier-Leibnitz (FRM II), OPA00331, Techn. Univ. München (2009)
- [Sak67] A. Sakharov. *JETP Lett.*, **5**, 24 (1967)
- [Sat88] J. Sater, J. Gaines, E. Fearon, P. Souers, F. McMurphy and E. Mapoles. *Phys. Rev. B*, **37**, 1482 (1988)
- [Sau13] A. Saunders et al. *Rev Sci Instrum*, **84**, 013304 (2013)
- [Sch14] F. Schmid. *Messung der Wärmeleitfähigkeit von Deuterium mittels der  $3\omega$  Methode*. Bachelor Thesis, Physics Department E18, Technical University of Munich (2014)
- [Sea92] V. F. Sears. *Neutron News*, **3**, 26 (1992)
- [Sem16] I. Semrock. LPD02-532RU Measured Spectrum. Typical measured spectrum of Semrock LPD02-532RU Optical Filter, Downloaded on 31st May 2016 (2016)
- [Ser10] A. Serebrov, A. Fomin and V. Varlamov. arXiv:1001.3210v1 [nucl-ex] (2010)
- [She94] V. Shevtsov, A. Frolov, I. Lukashevich, E. Ylinen, P. Malmi and M. Punkkinen. *J. Low Temp. Phys.*, **95**, 815 (1994)
- [Sil80] I. Silvera. *Rev. Mod. Phys.*, **52**, 393 (1980)
- [Sin88] S. K. Sinha, E. B. Sirota, S. Garoff and H. B. Stanley. *Phys. Rev. B*, **38**, 2297 (1988)
- [Sou86] P. C. Souers. *Hydrogen Properties for Fusion Energy* (University of California Press, Berkeley and Los Angeles, California, 1986)
- [Ste72] A. Steyerl. *Z. Physik*, **254**, 169 (1972)

- [Ste86] A. Steyerl et al. Phys. Lett. A, **116**, 347 (1986)
- [Ste91] A. Steyerl, S. Malik and L. Iyengar. Physica B, **173**, 47 (1991)
- [Ste10] A. Steyerl, S. Malik, A. Desai and C. Kaufman. arXiv:0911.4115v2 [cond-mat.other] (2010)
- [Sto89] R. Stolen, J. Gordon, W. Tomlinson and H. Haus. J. Opt. Soc. Am. B, **6**, 1159 (1989)
- [Tur65] V. Turchin. *Slow Neutrons* (Israel Program for Scientific Translations Ltd., 1965)
- [VK60] J. Van Kranendonk. Can. J. Phys., **38**, 240 (1960)
- [VK83] J. Van Kranendonk. *Solid Hydrogen* (Plenum Press, New York, 1983)
- [Whi63] G. White. Radiation Research, **18**, 265 (1963)
- [Wlo11] S. Wlokka. *Die neue UCN-Quelle am FRM II – Produktion ultrakalter Neutronen mit Kryo-Konvertern und Betrachtung ausgewählter Sicherheitsaspekte*. Diploma Thesis, Physics Department E18, Technical University of Munich (2011)
- [Wlo15] S. Wlokka, P. Fierlinger, A. Frei, P. Geltenbort, T. Huber, S. Paul, K. Schreckenbach and R. Stoepler. Neutron Delivery Systems 2015 Proceedings: Investigation of Guides for Ultracold Neutrons. Submitted for publication (2015)
- [Yu86] Z.-C. Yu, S. Malik and R. Golub. Z. Physik, **62**, 137 (1986)
- [Zec15] T. Zechlau. Private Communication (2015)
- [Zie10] J. F. Ziegler, M. D. Ziegler and J. P. Biersack. Nucl. Instrum. Methods B, **268**, 1818 (2010)
- [Zim15] O. Zimmer and R. Golub. Ultracold neutron accumulation in a superfluid-helium converter with magnetic multipole reflector. arxiv:physics.ins-det/1303.1944v2 (2015)

# Danksagung

Im Verlauf dieser Dissertation konnte ich auf die Unterstützung viele verschiedener Leute zählen. Besonders erwähnen möchte ich hier die folgenden Personen.

- Univ.-Prof. Dr. Peter Fierlinger, der als Doktorvater diese Dissertation betreut hat.
- Dr. Andreas Frei, der mir als direkter Betreuer stets mit Rat und Tat zur Seite stand.
- Univ.-Prof. Dr. Winfried Petry und Herrn Dr. Jürgen Neuhaus, die diese Dissertation möglich gemacht haben.
- Herrn Dr. Christian Bocquet, Herrn Dipl.-Ing. Fernando Cristiano und Herrn Dipl.-Ing. Johann Schilcher für die vielen fruchtbaren und unterhaltenden Gespräche über Physik und Nicht-Physik.
- Herrn Thomas Deuschle und Herrn Stefan Wenisch, für die vielen kleinen und großen Bauteile und Einsätze, die zum Gelingen der Arbeit beigetragen haben.
- Herrn Dr. Christoph Morkel, der mir half das ein oder andere wissenschaftliche Detail zu klären.
- Den Master-, Bachelor und Werkstudenten, die ich während meiner Promotion betreuen durfte.
- Allen Mitarbeitern des Maier-Leibnitz Laboratoriums, vor allem den Operateuren sowie Herrn Dr. Ludwig Beck und Herrn Dipl.-Ing. Peter Hartung.
- Dr. Peter Geltenbort und Herrn Thomas Brenner, für die großartige Unterstützung während meiner Messkampagnen am ILL.